DOCTOR OF PHILOSOPHY

Heating of solid matter via laser generated electrons

Garland, Rory

Award date:
2018

Awarding institution:
Queen's University Belfast

Queens University Belfast

School of Mathematics & Physics

Heating of solid matter via laser generated electrons

Author: Rory J. Garland

Supervisor: Alex P. L. Robinson & Marco Borghesi

A thesis submitted in fulfilment of the requirements for the degree of Doctor of Philosophy

June 2019

Declaration of Authorship

I, Rory J. Garland, declare that this thesis titled, 'Heating of Solid Targets via Laser Generated Fast Electrons' and the work presented in it are my own. I confirm that:

- This work was done wholly or mainly while in candidature for a research degree at this University.
- Where any part of this thesis has previously been submitted for a degree or any other qualification at this University or any other institution, this has been clearly stated.
- Where I have consulted the published work of others, this is always clearly attributed.
- Where I have quoted from the work of others, the source is always given. With the exception of such quotations, this thesis is entirely my own work.
- I have acknowledged all main sources of help.
- Where the thesis is based on work done by myself jointly with others, I have made clear exactly what was done by others and what I have contributed myself.

Signed: _____

Date: _____

I do.

Natasha Paris Anita Garland, 11th August 2018

Abstract

This thesis reports on numerical studies of the heating of solid targets via laser generated fast electron beams, which allows for better understanding and optimisation of the generation of hot dense matter in a laboratory setting. The work is split into 3 main investigations which are summarised below.

In the first investigation, simple analytical scalings of target temperatures with laser-target parameters, I_L, λ_L, n_i, produced by the Spitzer resistivity and a prescriptive low temperature for Ohmic heating were compared using a 3D Hybrid-PIC code. Results showed that the scalings from the Spitzer resistivity underestimate the overall dependencies and the numerical results are found to be better fit by the prescriptive low temperature resistivity model. Thus, not only is the Spitzer resistivity insufficient to characterise the full evolution of a target but it is also shown that the low temperature regime of the target plays a pivotal role in the evolution of the target.

In the second investigation, assumptions made in the previous investigation, constant ionisation and specific heat capacity, were explored via a 0D heating model. Results showed that the assumption had little impact on the scalings from the 0D model. It was noted, however, that fixing the ionisation and specific heat capacity resulted in higher overall temperatures. This was expanded upon by varying these two independently while also considering a more complete resistivity model which accounted for electron statistics and collisions. It was found that fixing the specific heat capacity produces higher temperatures compared to fixing the ionisation state. These results show that the scaling relations derived in the previous Chapter will be incorrect due to the ideal gas capacity having no temperature dependence. Furthermore, these results indicate how important the selection of the specific heat capacity is for a correct characterisation of the target.

In the third investigation, the generation of uniform heating for potential use in heating experiments was considered from various designs of the inverse conical taper using a 3D Hybrid-PIC code. Results showed that a 2-material design with a "square" geometry of an Al cone, which has a truncated inverse pyramid-like shape in this geometry, and Cu wire were found to produce regions of uniform heating. This occurred due to inhomogeneous transport in the fast electron beam,

which is not present in a 1-material design, e.g. Al, where a monotonically decreasing current density is found. While the exact reasons were not fully elcuidated, various investigations were carried out to consider the optimum periods of uniform heating. First, the Z value of the wire was then varied to see its role in the uniform heating. It was found that both Z values smaller and larger than Cu resulted in less uniform heating. Work then considered varying the I_L & λ_L with these producing contrasting results. Due to the strong dependence of the current density on λ_L, the variation results in dramatically different transport patterns. Increasing λ_L, decreasing current density, results in uniform heating occurring in a different position. Decreasing λ_L, increasing current density, results in larger interior magnetic fields, producing a completely different transport pattern. On the other hand, varying I_L produces similar transport patterns. Increasing I_L, results in a smoother inhomogeneous transport pattern and thus an absence of uniform heating while decreasing I_L enhances the inhomogeneous transport and results in periods of uniform heating. Further work considered whether the uniform heating was limited to certain values of the fast electron conversion efficiency, β. Results showed that the uniform heating was independent of β but the position of the uniform heating was varied due to the variation in current density. Finally, a cylindrical geometry of the same area was considered to investigate the production of this uniform heating. Results showed that uniform heating was also produced in this geometry but that the transport patterns differed greatly. This arised due to the larger radius of the cylindrical geometry, leading to a weaker field generation meaning that the fast electron beam went under a more stable transport compared to the "square" approach.

Acknowledgements

The undertaking of a PhD is never done in a vacuum, with there being a variety of people whom have contributed and helped throughout the duration of this work. Below presents but a snippet of the help I have had from a variety of people during this work.

First, I would like to extend my eternal gratitude to my external supervisor Dr Alex P. L. Robinson, who guided me through this research. The support, guidance and replying to some rather hefty emails have not only been constant but also invaluable throughout this work.

Secondly, to my other supervisor Professor Marco Borghesi, who I found to be one of the most calming influences throughout this work. No issue was too larger or worrisome and whatever the situation, there was always a solution.

There a various people in the PhD cohort from both this institution, QUB, and other institutions who deserve to be thanked. First to my housemate for 2 years and friend for far longer, Nicholas Millington. From our almost daily lunches to Subway to our debates about Star Trek, to politics and everything in-between, you have made this PhD bearable for all of these years! To Kealan Naughton, I am sorry for all those hours I spent talking rubbish to you in the office! To Brendan Coleman, whom spent more time with me sitting over a coffee talking rubbish than anyone else. Thanks also to Guillermo Marrero Samarin, Richard Warwick, Ahmed Sharba, Robert Cohen & Seyed Reza Mirfayzi from QUB. To all of the other people at various institutions: Nick Butler, Robbie Wilson, Jordan Taylor, Dean Rusby and the many more I forget, thank you.

To my family who have helped me throughout this, thank you.

Last, and by no means least, to my wife, Natasha. While you may not have been with me through the entire duration of the PhD, you have taken the brunt of it. From the late nights to the early mornings, from the cancelled plans to the constant doubting, and from the constant babbling on about physics to me going "but it's my PhD", you have been through it all. If it were not for your willing me on, being exempt from chores was brilliant, I would not have finished this. I

have a debt of gratitude that one life time alone will never fully repay it. I can start by dedicating this work to you, and hoping that this is modest proof of my sheer appreciation of you.

Contents

List of Figures

List of Tables

To my wife, Natasha

Chapter 1

Introduction

1.1 Motivation

Since their first experimental demonstration almost 60 years ago (Maiman (1960)) [1], lasers have found uses in all walks of life due to the unique properties of light they produce: high directionality, monochromaticity & spatial and temporal coherence. Following the advent of the Chirped Pulse Amplification technique (CPA) in 1985 [2], short pulse lasers have been able to reach the relativistic regime: $I_L \lambda_L \geqslant 10^{18}$ Wcm^{-2} μm^2. When a linearly polarised relativistically intense laser pulse is incident upon a solid target, fast electrons (v $\sim$ c) are generated through a variety of mechanisms and can propagate through the target. This process, known as fast electron transport (FET), presents a rich variety of physical effects, and is of relevance to numerous applications ranging from laser driven fusion to laser driven ion acceleration to many more.

1.2 Fast Electron Transport (FET)

The generic picture of fast electron transport can be considered as follows. A linearly polarised, short pulse at irradiance, $\geqslant 10^{18}$ Wcm^{-2} μm^2, is incident upon a solid target and accelerates a small proportion of electrons to velocities $\sim$ c, fast electrons. The mechanisms through which energy and momentum are transferred are discussed in Chapter 2. The coupling efficiency of the laser energy to fast electron energy is typically between 0.2 - 0.5. The fast electrons will then proceed

to propagate through the target, which leads to the generation of resistive EM fields which can stop these fast electrons in distances $< \mu$m [3, 4]. To facilitate the propagation of the fast electrons, a return current is formed within the solid target which results in the neutralisation of the fast electron beam. Moreover, while these two currents neutralise each other the physical nature of the two beams is very different, with the return current being collisional in nature compared to the fast electrons collisionless nature. These contrasting physical characteristics lead to very different heating mechanisms, with the return current producing Ohmic heating, which can raise the temperature inside a solid target to keV in ps time-scales [4]. The fast electron beam can also induce heating via drag & collisional stopping of the beam [4]. Incomplete neutralisation of the fast electron beam will result in the growth of EM fields [4, 5]. The magnetic fields generated can either act to collimate or hollow the fast electron beam. Following the propagation of the fast electron beam in a target, the fast electrons will either come to a stop and heat it (if the target length is larger than the mean free path), or will generate large electric fields resulting in the acceleration of ions (if the target length $<$ mean free path). The regimes and applications which utilise these physical mechanisms are briefly explored in the sections below.

1.2.1 Laser Driven Ion Acceleration (LDIA)

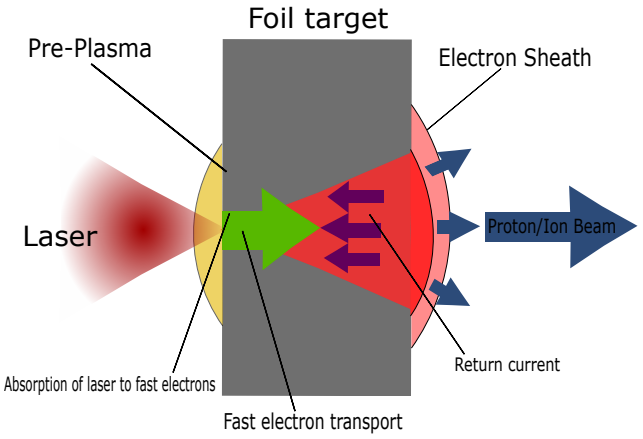

FIGURE 1.1: A schematic of Target Normal Sheath Acceleration (TNSA)

Laser Driven Ion Acceleration allows for the generation of high energy (MeV) ions in target lengths of μm. This can be achieved by a variety of regimes, including: Target Normal Sheath Acceleration (TNSA), Radiation Pressure Acceleration (RPA) & Break-Out Afterburner (BOA) [5–7]. Due to TNSA being predicated upon efficient fast electron transport [5–7], it is the only mechanism discussed. The TNSA mechanism follows on from the physical mechanisms discussed in the previous section, with MeV fast electrons propagating through a target and reaching the rear of the target where electrons escape into vacuum. The charge separation leads to the generation of an electric field of the order TV m^{-1}. This electric field is large enough to ionise the atoms on the rear of the target and then accelerate them to MeV energies normal to the target surface. Due to their favourable charge-mass ratio, it is found that protons are the most efficiently accelerated ions [5, 6, 8–10].

The proton/ion beam produced from this acceleration method is found to posses a variety of attractive features including: high energy, highly laminarity, low emittance [5, 6, 11]. These features lead to current, and proposed, applications in a variety of fields: proton oncology [5, 6, 12], fast ignition [5, 6, 13], proton imaging [5, 13], Warm Dense Matter (WDM) [5, 6, 13] and heating of targets.

With the fast electrons leading to the generation of the electric field at the rear of the target, their transport and characteristics are crucial to the overall structure of the ion beam generated [6, 8–10, 14–17]. Both Fuchs et al (2003) [9] & Roth et al (2002) [15] showed that the type of target at room temperature, conductor or insulator has a large impact on the propagation of the fast electron beam, with the insulator leading to inhomogeneities in the fast electron beam and thus leads to a modulated ion beam. McKenna et al (2011) [14] investigated the role of lattice structure in Carbon, showing that a disordered lattice will lead to more filamentation of the fast electron beam and thus produce a more modulated ion beam compared to that of a structured lattice.

The results from these works shows that the understanding of fast electron transport is paramount to the success of this form of LDIA.

1.2.2 Inertial Confinement Fusion (ICF)

Another application of laser-plasma physics is that of Inertial Confinement Fusion (ICF). This method offers the possibility of controlled fusion, and with it a potential for clean and long-lasting energy source that can meet todays high energy consumption needs.

The ICF approach uses the compression and heating of a deuterium-tritium fuel contained with capsules via drivers (such as lasers or x-rays). Central hot-spot ignition, via either direct of indirect drive, is the predominant most conventional of the methods within ICF. This approach requires for the fuel to be compressed to large densities (1000 g/cm^3) to generate a hotspot which initiates fusion "burn". Direct Drive is found to be prone to a variety of instabilities and requires an almost perfect symmetry for high energy gain [18]. With these drawbacks in mind, another regime was presented by Tabak et al (1994) [19]: Fast Ignition (FI).

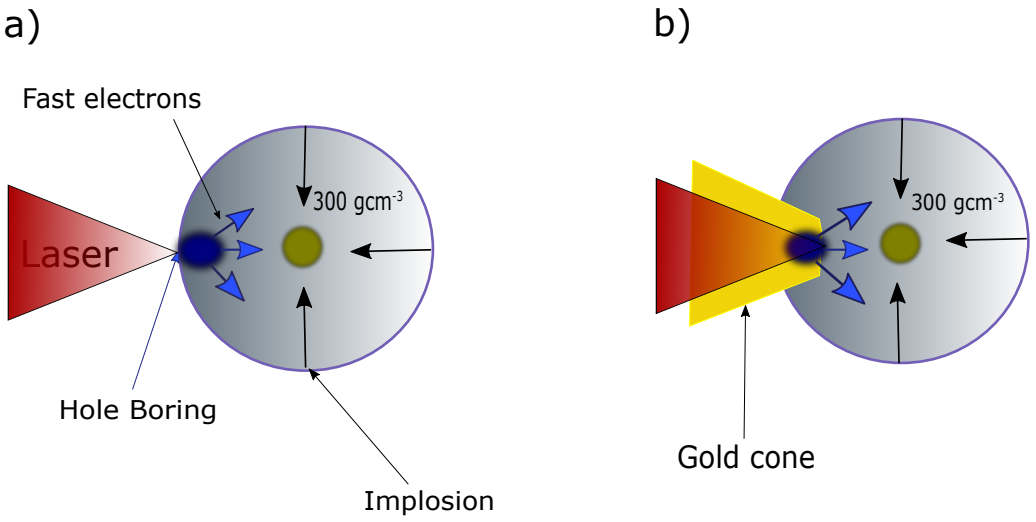

FIGURE 1.2: Illustration of the igniter pulse in a) Hole Boring & b) Gold Cone regimes of FI

FI aims to overcome a variety of issues found within the hot-spot regime by decoupling the compression and ignition stages from one another. The first stage of FI is still to compress the fuel to high densities ($300 < \rho < 1000$ g/cm^3) [4, 5]. After this compression a second intense "igniter" pulse (10 kJ, 10 ps) [20] couples its energy into fast electrons which propagate a certain distance, known as the

"stand-off" distance, through the target and heat a hot-spot to temperatures of $\sim$ 12 keV required for fusion [5, 21]. Performing ICF through this regime offers a variety of benefits compared to conventional ICF. As FI is an isochoric approach (constant density) [4, 5, 18, 22–24] compared to the isobaric (constant pressure) approach of hot-spot regime [5, 18, 22, 23], it results in the compression of the fuel being both less stringent and demanding therefore meaning that a less energetic driver can be used. As well as this, the hydrodynamic constraints on the implosion process are also reduced [4]. These features of FI allow for a very high gain ($>$ 100), while using considerably less driver energy [4, 5, 19–22, 24–29].

The original mechanism for FI is known as the hole-boring regime [19, 20]. In this regime, as shown in figure 1.2 (a), after the ablation and compression of the target, a channel is formed in the plasma by a "hole-boring" laser. Following this, fast electrons are generated at the critical density, by an ignition pulse guided through the channel, and propagate to the high density core [19]. Difficulties were discovered due to typical "stand-off" distances being $\approx$ 300 μm. This distance resulted in fast electron energy being lost to plasma instabilities or to angular deflections and raised questions of how effective hole-boring would be [18, 20]. Efforts have been made to reduce this "stand-off" distance by the use of a hollow gold cone, or similar high Z material, embedded within the target, as shown in figure 1.2 (b). In this method, the igniter pulse is focused onto this gold cone causing the fast electrons to be generated at its tip. This results in the "stand-off" distance being reduced to $\approx$ 100 μm resulting in less loses from the fast electron beam [4, 21, 22, 25, 28].

1.2.3 X-ray Generation

The propagation of this relativistic fast electron beam through a solid target will lead to the generation of x-rays due to the various interactions with the background ions and electrons, e.g. collisions, ionisation, recombination [10, 13, 30–35]. These x-rays are not only highly energetic with values ranging from keV to MeV but are also found to have a small emission area, therefore resulting in high resolution of radiographic images [10, 30], if they are employed as backlighter beams.

1.2.4 Heating experiments

At the start of a fast electron transport experiment the target of concern, as will be discussed in section 3.6, will start out at a cold temperature, e.g. described via solid state physics. This target will subsequently be heated to temperatures > 100 eV (10^6 K) where it will be in the plasma state. Before its transition to a plasma state, the target will be in a intermediate state known as Warm Dense Matter (WDM) [28, 32]. This state is characterised by being degenerate $\theta \leq 1$, equation 3.36, where the Fermi energy is larger than the thermal energy, and strong coupling between the ions, $\Gamma \geq 1$, equation 3.35. If the coupling parameter is still ≥ 1 even once the temperatures are in the plasma region, this state of matter is known as either Hot Dense Matter (HDM) [36] or hot dense plasmas [37]. Both of these states of matter, especially WDM, are found to be of critical interest in the characterisation of astrophysical objects [32, 36, 38, 39], e.g. Brown Dwarf Stars [38], and ICF [28, 32, 36, 39], e.g. the outer layers of the target [28]. Thus, fast electron experiments will allow for a characterisation of the Equation of State (EOS) or opacity of these states of matter, allowing for a more complete understanding and better benchmarking of models. For an optimal characterisation of these properties, isochoric heating in the region of interest is desirable [28, 40]. However due to a variety of reasons such as, transport instabilities, angular scattering & longitudinal dispersion, uniform heating is not easily achievable in the laboratory via Ohmic heating. Thus, techniques or designs are needed to improve both the optimisation and uniformity of heating, some of which will be discussed in this thesis.

1.3 Thesis Overview

The thesis is structured down into the following chapters:

2. This chapter discusses the theoretical concepts behind laser-matter interactions. This starts by considering the CPA technique before discussing ionisation and electron motion in an EM wave. From here, relevant plasma parameters are defined and various laser-plasma absorption mechanisms are discussed.

3. This chapter discusses the physics more relevant to this thesis. This starts at the consideration of the Thomas-Fermi Model before discussing the various resistivity models used in fast electron transport. Following this, the various physical implications of fast electron transport ranging from heating to EM field generation to instabilities are discussed. The chapter is rounded off by considering numerical and experimental methods for investigating fast electron transport.

4. Investigates the scaling relations connecting Ohmic heating to various laser and target parameters in solid targets using a 3D Hybrid-PIC code. Scalings based on a low temperature resistivity & Spitzer resistivity are compared.

5. Investigates the assumptions of constant specific heat capacity & ionisation made in the previous chapter via the construction of a 0D heating model.

6. Investigates uniform heating found within inverse conical taper targets for possible use in uniform heating experiments via a 3D Hybrid-PIC code. Both target designs and laser parameters are varied to see how different material affects heating uniformity throughout the target. Following this, different target areas are also considered.

7. Brings the work together, discussing the findings and future work.

1.4 Role Of the Author

The results presented in this thesis is entirely the author's own work, with all simulations and analysis performed by the author. The implementation of the Robinson Resistivity model, Chapter 5, was done with the help of Dr A. P. L. Robinson. The results in Chapter 4 were published in [41]:

Analysis of fast electron scaling theory for the heating of a solid target. Physics of Plasma **23**, 083116 (2016), R. J. Garland, M. Borghesi and A. P. L. Robinson.

Chapter 2

Laser-Solid Interactions

2.1 Introduction

When a sufficiently high power laser interacts with a solid target, it leads to the generation of a plasma via rapid ionisation. The laser proceeds to couple its energy to the plasma which leads to the generation of relativistic electrons which proceed to propagate through the target. In this Chapter, these various mechanisms will be discussed. It must be noted that there are variety of books, papers, lecture notes which present a very good description of laser-plasma physics. The author would like to acknowledge the extensive use of Gibbon (2004) [13] & Eliezer (2002) [42] throughout the use of this chapter.

2.2 Chirped-Pulse Amplification (CPA) Lasers

All short-pulse, high power lasers are predicated upon the technique of Chirped-Pulse Amplification (CPA) [2, 7, 13, 18, 28, 42–45] which allows for laser intensities $\geq 10^{18}$ Wcm^{-2}. The premise of this technique, based originally on a radar technique, is to stretch a laser pulse in time so that it is safe to be amplified and then re-compressing it down.

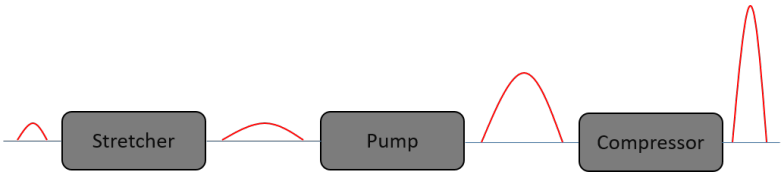

FIGURE 2.1: Simple figure showing the process of CPA in lasers. The pulse is first stretched in time, reducing its intensity and allowing for the pulse to be amplified. The pulse is then re-compressed down. Producing a short, relativistic laser pulse.

The pulse is first stretched temporally by diffraction gratings resulting in a decrease in laser intensity, therefore allowing for pulse to be amplified. Following this amplification, the pulse is then re-compressed down to a pulse length slightly longer than that of the original pulse. The disparity in the pulse lengths arises from the combination of gain narrowing and non-linear dispersion effects [43]. Figure 2.1 shows a very simple schematic of the CPA process.

The generation of this ultra-short pulse is often coupled with pre-pulses and amplified spontaneous emission (ASE) [7, 12, 15, 26, 28, 43, 45–55]. The ratio between these generated pulses and the main pulse can be described by the two following ratios. The temporal intensity contrast (TIC) describes the ratio between the peak laser intensity, I_0, and the laser intensity at time t, I_t, where $t < 0$ is before the pulse and $t>0$ is after the pulse [45]. On the other hand contrast ratio describes the ratio between I_0 and ASE [7, 12, 13, 15, 26, 28, 29, 32, 35, 36, 43, 44, 46–59].

The pre-pulse and ASE generation can be split into 4 categories: a) pre-pulses, ns time scale, leaking through the laser system due to the architecture of the laser system; b) pre-pulses, ps time-scale, which is primarily generated from non-linear mixing of post-pulses and temporally overlap with the stretched main pulse during amplification; c) deterioration of the rising slope of the main pulse, due to uncompensated higher-order spectral phase modulations d) ASE generated by fluorescence emitted in the different amplification stages of the laser [45]. Unlike terms a-c which are dependent upon the laser system, therefore allowing to be tuned and reduced, ASE depends instead on the active material in the amplifiers and cannot be suppressed completely [45], meaning that it will play a role in almost all laser systems [7, 12, 13, 15, 26, 28, 29, 32, 35, 36, 43–59]. The generation of ASE can be considered as follows. Atoms spontaneously emit photons randomly

within a solid angle of 4π steradians. Photons which are emitted outside of the central axis leave the laser chain without much amplification while photons which are emitted near the central axis are amplified in the same manner as the stimulated emitted photons. The intensity of this generated pulse is found to be 6-10 orders of magnitude smaller than the peak intensity [7, 28, 43, 44, 60], meaning that it can play a non-trivial role in laser-solid experiments. A further discussion of this can be found in section 2.5.2.

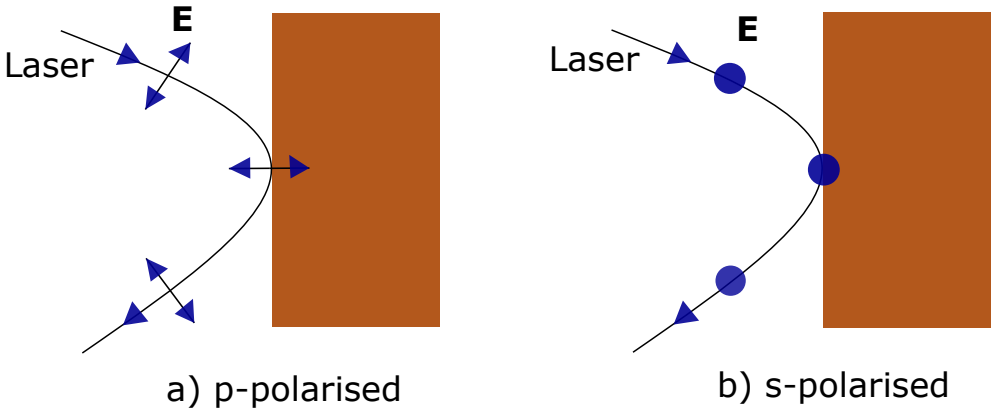

FIGURE 2.2: Figure showing linear laser polarisation. (a) p is parallel to the plane of incidences (b) s is perpendicular to plane of incidence.

During the production and use of a laser pulse, one must consider the polarisation being used. This is defined by the orientation of the electric field. If the field has a polarisation perpendicular to the plane of incidence it is referred to as s-polarised whereas, if the wave has polarisation parallel to the plane of incidence it is referred to as p-polarised. This is shown in figure 2.2.

2.3 Ionisation Mechanisms

During the interaction of a sufficiently intense laser pulse with a solid target, ionisation will occur. Rapid ionisation of the target will occur if the electric field of the laser pulse is larger than that of the electric field for the respective atom.

The yard-stick used in this scenario is by considering a hydrogen atom with a Bohr radius [13]

$$a_B = \frac{4\pi\epsilon_0\hbar}{m_e e^2} = 5.3 \times 10^{-11}\,\mathrm{m} \tag{2.1}$$

where $\hbar$ is the reduced Planck's constant, m is the mass and e is the fundamental charge. The electric field at this distance is given by

$$E_{ab} = \frac{e}{4\pi\epsilon_0 a_B^2} = 5.1 \times 10^{11}\,\mathrm{Vm}^{-1}. \tag{2.2}$$

From here it is possible to calculate the laser intensity required to equal this electric field produced, known as the atomic intensity

$$I_a = \frac{\epsilon_0 c E_{ab}^2}{2} \simeq 3.51 \times 10^{16}\,\mathrm{Wcm}^{-2}. \tag{2.3}$$

Hence, any laser intensity $> 3.51 \times 10^{16}$ Wcm^{-2} will result in the ionisation of the matter it is incident upon. The ionisation processes considered in a laser-solid interaction are: multi-photon ionisation, tunnelling ionisation and barrier-suppression, which are all represented in figure 2.3 (a-c).

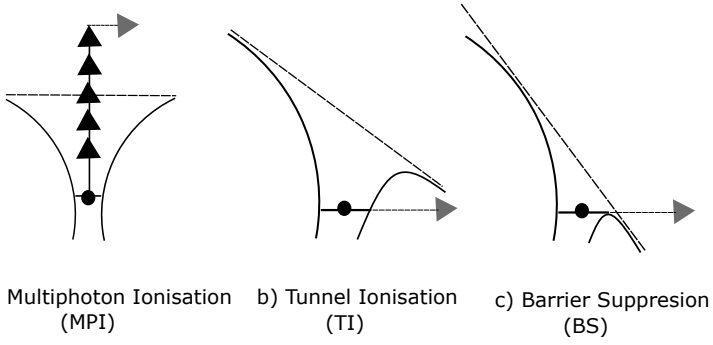

FIGURE 2.3: Mechanisms for the ionisation of an atom via laser-solid interactions (a) multi-photon ionisation, (b) tunnel ionisation, (c) Barrier Suppression

To show which mechanism is dominant, Keldysh (1965) [61] introduced the Keldysh parameter

$$\gamma_k = \omega_L \sqrt{\frac{2E_{ion}}{I_L}} \sim \sqrt{\frac{E_{ion}}{\Phi_{pond}}}, \tag{2.4}$$

where ω_L is the frequency of the ionising field of intensity I_L, E_{ion} is the binding energy of the ion & Φ_{pond} is the ponderomotive potential of the laser field (discussed in section 2.4.1) and is written as

$$\Phi_{pond} = \frac{e^2 E_L^2}{4m\omega_L^2}. \tag{2.5}$$

where E_L is the electric field of the laser.

When the laser intensity is low, $\gamma_k > 1$ and the multi photon absorption process dominates, as seen in figure 2.3 (a) [13, 61]. In this process, the electron absorbs n photons for ionisation and s excess photons, resulting in a final kinetic energy of [13]

$$E_{final} = (n+s)\hbar\omega - E_{ion} \tag{2.6}$$

where $\hbar\omega$ is the energy of each respective photon.

When the laser intensity increases $\gamma_k < 1$, the ponderomotive potential starts to dominate. This increase in laser intensity leads to I_L being comparable to I_a which results in the Coulomb field felt by the electron being distorted by the laser field and resulting in either Quantum Tunnelling, figure 2.3 (b) or Barrier Suppression, figure 2.3 (c). In the Quantum Tunnelling approach, the strength of the laser is large enough to lower the potential well, resulting in electrons without sufficient energy to escape the barrier. Whereas in Barrier Suppression, the strength of the laser is larger enough to lower the the potential well below E_{ion}, allowing for all electrons to escape the atom and therefore resulting in rapid ionisation via the process of barrier suppression. During this ionisation mechanism, other ionisation mechanisms are suppressed. Once enough electrons have been ionised via these two processes, collisional ionisation processes start to dominate [13].

The probability of the ionisation rate for a hydrogen-like atom (Z=1, 1s electron only) via quantum tunnelling is given as [13, 61]

$$\Gamma_H = 4\omega_a \left(\frac{E_{in}}{E_h}\right)^{\frac{5}{2}} \frac{E_{ab}}{E_L(t)} \exp\left[-\frac{2}{3}\left(\frac{E_{in}}{E_h}\right)^{\frac{3}{2}} \frac{E_{ab}}{E_L}(t)\right], \tag{2.7}$$

where E_{in} & E_h are the ionisation potential of the atom and hydrogen respectively, and

$$\omega_a = \frac{4\pi\epsilon_0 m_e e^4}{\hbar^3} = 4.16 \times 10^{16}\,\mathrm{s}^{-1} \tag{2.8}$$

is the atomic frequency.

Ammosov, Delone, and Krainov (1986)[62] presented the "ADK theory" which can calculate the tunnelling probability for more complex atoms/ions.

2.4 Electron Motion in a laser field

The liberation of electrons from their atomic shells via ionisation will mean that their motion will be influenced by the laser field which ionised the target. Here Gibbon (2004) [13] is followed, with other references used noted throughout. By considering that the laser pulse is propagating in the |x| direction, the vector potential of this EM wave can be written as[13, 63]

$$\mathbf{A} = A_0 \cos\phi = A_0 \cos\left(\omega_L t - k_L x\right), \tag{2.9}$$

where the subscript 0 denotes the amplitude, ω_L the laser frequency and k_L the wave number.

This definition allows for the description of both the electric, **E**, and magnetic, **B**, fields in terms of **A**. Both of these fields are perpendicular to each other and **A**,

$$\mathbf{E} = -\frac{\partial \mathbf{A}}{\partial t} = \mathbf{E_0} \sin\left(\omega_L t - k_L x\right), \tag{2.10}$$

$$\mathbf{B} = \nabla \times \mathbf{A} = \mathbf{B_0} \sin\left(\omega_L t - k_L x\right), \tag{2.11}$$

where $\mathbf{E_0} = A_0 \omega_L \hat{\mathbf{y}}$, $\mathbf{B_0} = A_0 k_L \hat{\mathbf{z}}$ and are considered in SI.

The equation of motion for electrons in this EM wave is given by the Lorentz equation [42, 63, 64]

$$\mathbf{F} = \frac{d\mathbf{p}}{dt} = m_e \frac{d\mathbf{v}}{dt} = -e(\mathbf{E} + \frac{1}{c}\mathbf{v} \times \mathbf{B}). \tag{2.12}$$

From equation 2.12 it can be seen that there will be two forces operating on the electron: the electric field $\mathbf{E}$ & magnetic field $\mathbf{B}$. The factor of $\frac{v}{c}$ in the $\mathbf{B}$ term limits the impact of the magnetic field to the relativistic regime. A parameter used to determine if the laser pulse is relativistic is [6, 7, 18, 43, 63, 65]

$$a_0 = \frac{\gamma v_q}{c} = \frac{eA_0}{m_e c} = \frac{eE_0}{m_e c \omega_L} = \sqrt{\frac{I_L \lambda_L^2}{1.37 \times 10^{18}\ \mathrm{Wcm^{-2}}\,\mu\mathrm{m}^2}} \tag{2.13}$$

where v_q is the quiver velocity and $\gamma = 1/\sqrt{1-\beta^2} = 1/\sqrt{1 - v_q^2/c^2}$ is the relativistic Lorentz Factor.

The definition of a_0 allows for two regimes to described for the electron motion in an EM wave: $\mathrm{a}_0 < 1$ non-relativistic regime, while $\mathrm{a}_0 \geqslant 1$ is the relativistic regime.

In the non-relativistic regime, $\mathbf{B}$ can be neglected and the resulting integration of equation 2.12 gives the velocity of the electron [63],

$$\mathbf{v} = \frac{eE_0}{m_e \omega_L} \cos\left(\omega_L t - k_L x\right) \hat{\mathbf{y}} = v_q \cos\left(\omega_L t - k_L x\right) \hat{\mathbf{y}} \tag{2.14}$$

Integrating this will return the distance

$$y = \frac{eE_0}{m_e \omega_L^2} \sin\left(\omega_L t - k_L x\right) = \frac{v_q}{\omega_L} \sin\left(\omega_L t - k_L x\right). \tag{2.15}$$

Thus for the non-relativistic case, the acceleration of the electron is parallel to the electric field.

In the relativistic regime, the magnetic field is no longer negligible and will also affect the motion of the electron. As well as being accelerated parallel to the electric field, the electron is also accelerated in the laser propagation direction with the position being written as

$$y = a_0 \sin\left(\omega_L t - k_L x\right), \tag{2.16}$$

$$x = \frac{a_0^2}{4}\left[\left(\omega_L t - k_L x\right) + \frac{1}{2}\sin\left(2\left(\omega_L t - k_L x\right)\right)\right] \tag{2.17}$$

The motion of an electron in the laboratory frame is represented in figure 2.4 (a). Here it can be seen that the electron drifts in the direction of the laser propagation with this drift velocity being written as

$$v_D = \frac{a_0^2}{4 + a_0^2} c. \tag{2.18}$$

The electron will oscillate at $2\omega_L$ in the laser propagation direction, from $\mathbf{v} \times \mathbf{B}$ term, and ω_L in the transverse direction. When viewed in the reference frame, i.e. with no drift velocity, the electron orbit is the characteristic figure of 8 orbit shown in figure 2.4 (b).

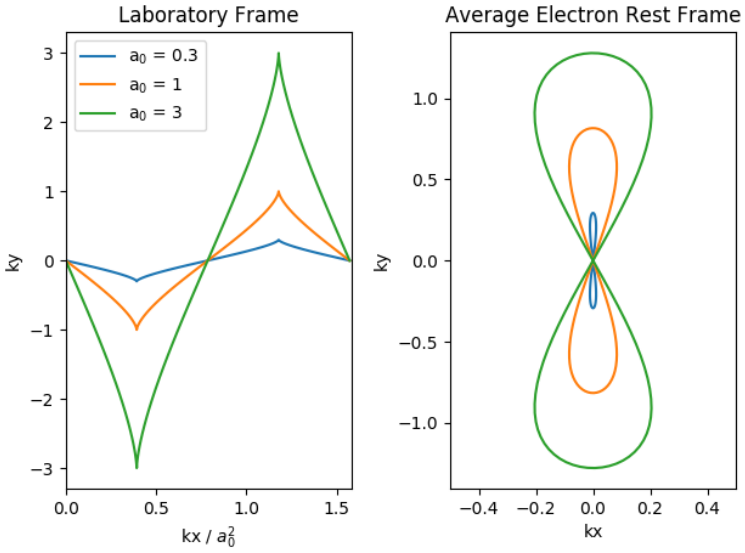

FIGURE 2.4: Electrons trajectories in an EM plane-wave with the laser propagation in the x direction with a wavelength of 1 μm. The magnetic field results in longitudinal displacement in the x direction while the electric field causes transverse displacement in y direction. a) In the laboratory frame, the electron trajectory is displaced along the direction of the laser propagation, increasing for an increasing a_0^2. b) The displacement of the two fields in the x-y direction causes the figure-8 orbit in the electron. Graphs produced from Gibbon (2004) [13].

2.4.1 Ponderomotive Force

According to the Lawson-Woodward theorem [13, 63], a plane wave cannot impart net energy on a charge. Short pulse lasers however violate this, due to not being a plane wave, and thus allow the acceleration of charges [13, 63]. When considering a laser field one of its characteristic features is a varying spatial intensity which can be split into two parts. In the first half of the laser cycle, the electrons are pushed away from regions of high laser intensity to regions of low laser intensity. During the second half of the cycle the sign changes, which will result in these electrons feeling a weaker return force meaning that the electron will not return to its original position. This force is known as the ponderomotive force and the cycled averaged form is given as [6, 13, 42, 63]:

$$f_p = -\frac{e^2}{4m_e\omega_L}\nabla \mathbf{E}^2. \tag{2.19}$$

In the relativistic regime, this force is written as

$$f_p = -mc^2\nabla\bar{\gamma} = -mc^2\nabla\sqrt{1+\frac{a_0^2}{2}}. \tag{2.20}$$

2.5 Plasma

As discussed in section 2.3, the rapid ionisation of the target results in numerous electrons being liberated from the target and, due to this, will result in a state change from a solid target to that of a plasma. This plasma, commonly referred to as the *fourth state of matter* [66], differs greatly from the other 3 states of matter. Instead of being constructed out of molecules and atoms, it instead consists of a sea of charged particles. The plasma appears to be quasi-neutral on a macroscopic scale and also exhibits behaviour [42, 66–70].

This quasi-neutrality is maintained by the plasmas ability to shield the rest of itself from foreign electrostatic fields [66, 67]. This can be shown if we consider a positive test particle, χ, being placed in a plasma, where the electron density follows a Boltzmann distribution [66–70]:

$$n_e(r) = n_0 \exp\left(\frac{e\phi}{k_B T_e}\right), \tag{2.21}$$

where $n_e(r)$ is the electron density at distance r from the test charge, n_0 is the average electron number density, e the charge on the electron, $k_B T_e$ the thermal energy in the plasma and ϕ the electric potential due to the test charge. It is assumed to occur on the time-scale of electrons therefore leaving the ions immobile [68].

The potential from χ can be described via Poisson's equation:

$$\nabla^2\phi = -\frac{\rho}{\epsilon_0} = -\frac{e}{\epsilon_0}\left(n_0 - n_0\exp\left(\frac{e\phi}{k_B T_e}\right)\right) \tag{2.22}$$

where ρ is the charge density & ϵ_0 is the permittivity of free space.

Rewriting equation 2.22 in spherical co-ordinates, we arrive at:

$$\nabla^2\phi = \frac{1}{r^2}\frac{\partial}{\partial r}\left(r^2\frac{\delta\phi}{\delta r}\right) \tag{2.23}$$

Assuming that the majority of the particles are free streaming & unaffected by ϕ, $k_B T_e >> e\phi$, allows for a first order Taylor expansion

$$\exp\left(\frac{e\phi}{k_B T_e}\right) \approx 1 + \frac{e\phi}{k_B T_e}. \tag{2.24}$$

Combining 2.21, 2.23 & 2.24, we arrive at

$$\frac{1}{r^2}\frac{\partial}{\partial r}\left(r^2\frac{\partial\phi}{\partial r}\right) = \frac{n_0 e^2\phi}{\epsilon_0 k_B T_e} \tag{2.25}$$

which can be written in the form

$$\nabla^2\phi = \frac{\phi}{\lambda_D^2}, \tag{2.26}$$

where λ_D is the Debye length which can be written as

$$\lambda_D = \left(\frac{k_B T\epsilon_0}{n_e e^2}\right)^{\frac{1}{2}}. \tag{2.27}$$

Using equation 2.23, we can write a differential equation of the form

$$\frac{\partial^2}{\partial r^2}(r\phi) = \frac{r\phi}{\lambda_D^2}, \tag{2.28}$$

re-arranging for ϕ, we arrive at

$$\phi(r) = \frac{\beta}{r}\exp\left(-\frac{r}{\lambda_D}\right) \tag{2.29}$$

At r $<<$ λ_D and taking $\beta = 4\pi\epsilon_0 r$, we arrive at the solution

$$\phi = \frac{q}{4\pi\epsilon_0 r}. \tag{2.30}$$

At distances r $\neq$ 0, the solution is

$$\frac{q}{4\pi\epsilon_0 r}\exp\left(\frac{-r}{\lambda_D}\right). \tag{2.31}$$

As equation 2.31 shows, that the electrostatic potential from χ is screened at distances > than λ_D [42, 66–70].

For this Debye shielding to occur there must be enough particles located within a "Debye sphere", with the number of particles within this sphere being written as

$$N_D = \frac{4}{3}n_e\pi\lambda_D^3, \tag{2.32}$$

For Debye shielding and collective behaviour to be valid, a plasma requires

$$N_D >> 1. \tag{2.33}$$

The ratio of PE to KE in a plasma can be written as

$$g = \frac{1}{n_e\lambda_D^3}. \tag{2.34}$$

Equation 2.34 infers that a larger amount of particles within the plasma therefore reduces the impact of collisions on the behaviour of the plasma which means that we can view this parameter, g, as a measure of the dominance of collective interactions over collisions [66].

In a steady state plasma, electrons will be located at their equilibrium position x_0. By applying an electric field to this plasma, a group of electrons will be displaced from x_0, resulting in a positive charged region at x_0 and a negative charged region at x_1. This charge disparity will give rise to a force which seeks to return these electrons to x_0. The acceleration by this field causes for the electrons to gain kinetic energy, which means that the electrons go past x_0 to point x_2. Thus the electron will oscillate about its equilibrium position at the frequency [29, 42, 66–70]

$$\omega_{pe} = \frac{(\frac{k_B T_e}{m_e})^{\frac{1}{2}}}{\lambda_D} = \sqrt{\frac{n_e e^2}{\epsilon_0 m_e}}. \tag{2.35}$$

The picture of the plasma is completed in section 3.3.1, where collisions and resistivity are discussed.

2.5.1 Laser Propagation in a Plasma

Now that the characteristics of a plasma have been defined, it is possible for us to consider the propagation of a laser, or any other EM wave, through this medium. The starting point of this consideration is Maxwell's famous equations are given as [18, 67]:

$$\nabla \cdot \mathbf{E} = \frac{\rho}{\epsilon_0} \tag{2.36}$$

$$\nabla \cdot \mathbf{B} = 0 \tag{2.37}$$

$$\nabla \times \mathbf{E} = -\frac{\partial \mathbf{B}}{\partial t} \tag{2.38}$$

$$\nabla \times \mathbf{B} = \mu_0 \left(\mathbf{J} + \frac{\partial \mathbf{E}}{\partial t} \right) \tag{2.39}$$

Using these equations in conjunction with the vector identity: $\nabla \times (\nabla \times H) = \nabla(\nabla \cdot H) - \nabla^2 H$, we can derive an equation describing the propagation of electromagnetic waves in a plasma:

$$\nabla \times (\nabla \times \mathbf{E}) = -\frac{1}{c^2}\frac{\partial^2 \mathbf{E}}{\partial t^2} - \mu_0 \frac{\partial \mathbf{J}}{\partial t} \tag{2.40}$$

By considering an electric field of the form

$$\mathbf{E} = E_0 \exp\left[i\left(\mathbf{kx} - \omega t\right)\right], \tag{2.41}$$

and writing $\mathbf{J}$ as

$$\mathbf{J} = -en_e\mathbf{v} = -\frac{n_e e^2 \mathbf{E}}{i\omega m_e} = \sigma \mathbf{E}, \tag{2.42}$$

where σ is the conductivity, we arrive at

$$-i\left[\mathbf{k}\times(\mathbf{k}\times\mathbf{E})\right] = -ik^2\mathbf{E} = -i\frac{\omega^2}{c^2}\epsilon\mathbf{E}. \tag{2.43}$$

ϵ is a dielectric constant

$$\epsilon = 1 - \frac{\sigma}{\epsilon_0\omega i} = 1 - \frac{n_e e^2}{\epsilon_0 m_e \omega^2} = 1 - \frac{\omega_p^2}{\omega^2} \tag{2.44}$$

where the definition of ω_p, equation 2.35, has been used.

Combining equations 2.43 & 2.44

$$k^2 = \frac{\omega^2}{c^2}\epsilon = \frac{\omega^2}{c^2}\left(1 - \frac{\omega_p^2}{\omega^2}\right), \tag{2.45}$$

re-arranging gives

$$\omega^2 = \omega_{pe}^2 + k^2c^2. \tag{2.46}$$

It can clearly be seen from equation 2.46 that for values where $\omega_{pe} \geq \omega$, k will either become 0 or imaginary resulting in the wave not being able to propagate in the plasma, this is therefore the cut-off limit for EM propagation in a plasma. The critical density at which the EM wave stops propagating through the plasma can be written as [6, 13, 18, 42, 63, 65]

$$n_c = \frac{\epsilon_0 m_e \omega_L^2}{\lambda_L^2 e^2} \tag{2.47}$$

This allow us to discriminate between: an under-dense plasma, $n_e < n_c$, and an over-dense plasma, $n_e > n_c$.

The evanescent part of the laser can however penetrate through this critical density. The distance to which this can propagate to in the plasma is given as

$$l_{sk} = \frac{c}{\omega_p}. \tag{2.48}$$

In the relativistic regime, $a_0 > 1$, the critical surface will be pushed deeper into the target due to the increase in the electrons mass[19, 65].

2.5.2 Pre-Plasma

The pedestal generated from a CPA laser, section 2.2, will result in the ionisation of the target surface and the formation of a "pre-plasma" in front of the target [7, 28, 49, 53, 54, 65, 71]. The rapid heating of the target results in material from the front surface of the target to blow off at roughly the sound speed [7, 13, 42, 65]

$$c_s = \sqrt{\frac{Z k_B T_e}{m_i}}. \tag{2.49}$$

Assuming an isothermal expansion, the density profile at position x from the target is[42]

$$n_e(x) = n_0 \exp\left(-\frac{x}{L_s}\right), \tag{2.50}$$

where L_s is the scale length of the pre-plasma and is given as [13, 65]

$$L_s \approx c_s \tau_L \simeq 3\sqrt{\frac{T_e}{\mathrm{keV}}}\sqrt{\frac{Z^*}{A}}\tau_{fs}\, 10^{-10}\,\mathrm{m}, \tag{2.51}$$

where τ_L is the duration of the pre-pulse.

2.6 Absorption Mechanisms

As the laser pulse propagates through this pre-plasma and eventually reaches the dense plasma regions near the original target surface, there are a variety of ways in which the energy of this pulse can be coupled to the target. With the contrasting nature of the two pulses, pre & main, there will be more than one mechanism occurring in an interaction. The dominant mechanism in this interaction is dependent upon a variety of factors, including laser intensity and density scale-length.

As well as this, it is possible to separate these mechanisms into two distinct categories: Collisional & Collisionless absorption which will both be discussed below [13, 18, 42, 63, 65].

2.6.1 Collisional

2.6.1.1 Inverse Bremsstrahlung

For lasers with $I_L\lambda_L^2 \sim 10^{12}$ - 10^{15} $\mathrm{Wcm^{-2}}\,\mu\mathrm{m}^2$, electrons absorb photons and then collide with the ions resulting in the plasma heating. This mechanism, known as Inverse bremsstrahlung (IB), can therefore be seen as a light wave being damped by the plasma which leads to the heating of said plasma [13, 65].

By taking this collisional nature of electrons and considering time scales where ion motion is neglected, the electron velocity, equation 2.12, now has an extra term for damping [42]

$$\frac{d\mathbf{v}}{dt} = -\frac{e\mathbf{E}}{m_e} - \frac{\mathbf{v}}{\tau_{ei}}, \tag{2.52}$$

where $\mathbf{B}$ is neglected due to $\mathbf{v}$ <<c and τ_{ei} is the average time between electron and ion collisions and can be written as

$$\tau_{ei} = \nu_{ei}^{-1} \propto \frac{T_e^{\frac{3}{2}}(\mathrm{eV})}{Z_i n_e} \tag{2.53}$$

By then solving equation 2.52 in combination with Maxwell's equations, equations 2.36 - 2.39, produces a dispersion relation of the from [42]

$$k^2c^2 \cong \omega_L^2\left(1 - \frac{\omega_p^2}{\omega_L^2} + \frac{\mathrm{i}\nu_{ei}\omega_p^2}{\omega_L^3}\right). \tag{2.54}$$

Due to the I_L scaling with the square of the electric field, equation 2.13, the damping is given by twice the imaginary part

$$\kappa_{IB} = \frac{\nu_{ei}}{c}\frac{\omega_p^2}{\omega_L^2}\left(1 - \frac{\omega_p^2}{\omega_L^2}\right). \tag{2.55}$$

By then using the definitions of the plasma frequency, equation 2.35, critical density, equation 2.47, and electron-ion collision frequency, equation 2.52, the damping rate can be written as

$$\kappa_{IB} \propto \frac{Z_i n_e^2}{T_e^{\frac{3}{2}}} \left(1 - \frac{n_e^2}{n_c^2}\right). \tag{2.56}$$

Equation 2.56 shows that optimum heating via IB requires high densities, high Z & low temperatures.

From equation 2.56 it can be seen that the collision time scales with $\mathrm{T}_e^{-\frac{3}{2}}$. This means that when increasing the intensity past $\mathrm{I}_L\lambda_L^2 \sim 10^{15}$ $\mathrm{Wcm}^{-2}\,\mu\mathrm{m}^2$, inverse-bremsstrahlung will play little role in the coupling of laser energy to the targets.

In conjunction with this, the increase in laser intensity will lead to larger quiver velocities for the electrons therefore reducing the collision frequency as shown by [13]

$$\nu_{eff} \simeq \nu_{ei} \frac{v_{th}^2}{(v_q^2 + v_{th}^2)}. \tag{2.57}$$

Thus, collisional effects beyond $\mathrm{I}_L\lambda_L^2 \sim 10^{15}$ $\mathrm{Wcm}^{-2}\,\mu\mathrm{m}^2$ play little role in the coupling of laser energy to the targets. Other mechanisms must therefore dominate in higher laser intensities.

2.6.2 Collisionless

2.6.2.1 Resonance Absorption

A p-polarised pulse with $\mathrm{I}_L\lambda_L^2 > 10^{15}$ $\mathrm{Wcm}^{-2}\,\mu\mathrm{m}^2$ [13, 42], will propagate through the plasma before being reflected at the density [6, 13, 18, 42, 63, 65, 72]

$$n_e(\theta) = n_c \cos^2(\theta). \tag{2.58}$$

At this point of reflection, the laser's E field component is parallel to the density gradient which tunnels through the critical density, section 2.5.1, and drives a

plasma wave in the form of density perturbations. This heating mechanism is called Resonance Absorption [13, 18, 42, 63, 65, 72] which is represented in figure 2.5

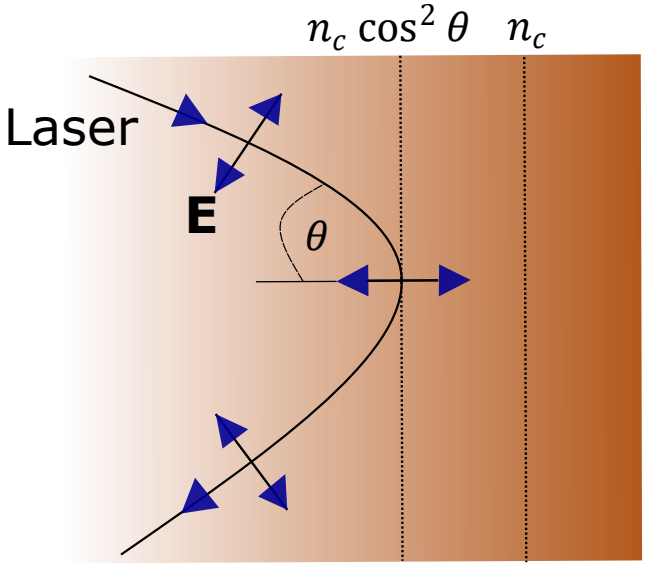

FIGURE 2.5: Figure showing resonance absorption for an electric field parallel to the density gradient, p-polarisation.

The absorbed fraction of energy is [13, 65]

$$f_{res-abs} \sim \frac{1}{2}\phi^2(\tau) \tag{2.59}$$

where τ is used to link the angle of incidence and scale length

$$\tau = \left(\frac{\omega_0 L_s}{c}\right)^{1/3} \sin\theta, \tag{2.60}$$

with ω_0 being the frequency of the excited plasma wave and

$$\phi \simeq 2.3\xi e^{\frac{-2\phi^3}{3}}. \tag{2.61}$$

Optimum heating occurs when considering large plasma scale lengths ($L_s >> \lambda_L$). Increasing the laser intensity however leads to the steepening of the density gradient which decreases the efficiency of resonance absorption leading to other absorption mechanisms dominating at higher intensities, i.e. $I_L\lambda_L^2 > 10^{17}$ $\mathrm{Wcm^{-2}}\,\mu\mathrm{m}^2$ [13].

2.6.2.2 Vacuum Heating(Brunel Mechanism)

For cases where $L_s << \lambda_L$, vacuum heating is found to dominate over Resonance Absorption[6, 13, 42, 63, 65]. In this mechanism, the electron is pulled out of the target during the first half of the laser cycle by the laser's electric field before being accelerated back into the target during the second half of the laser cycle [13, 42, 63, 65]. With the electric field of the laser only being able to penetrate to the skin depth, equation 2.48, the electron can travel almost unhindered through the target [13]. The fractional absorption can be written as [65]

$$f_{vhabsorb} = \frac{\eta}{2\pi}\frac{v_q^3}{v_L^2 c\cos(\theta)} \tag{2.62}$$

where η is an efficiency factor which shows how much oscillatory motion is lost in heating the plasma.

2.6.2.3 j × B Heating

$\mathbf{j} \times \mathbf{B}$ heating occurs when $I_L\lambda_L^2 > 10^{18}$ $\mathrm{Wcm^{-2}}\,\mu\mathrm{m}^2$, $a_0 > 1$. This mechanism is very similar to that of Vacuum Heating, with the electron being pulled out of the target and then accelerated back into the target. The difference however is that due to $a_0 > 1$, the $\mathbf{v} \times \mathbf{B}$ of the Lorentz Force, equation 2.12, is instead the driving force of the electrons along the laser's k direction while these electrons oscillate at $2\omega_L$, as discussed in section 2.4.1 [6, 13, 63, 65]. For a linearly polarised laser pulse, the longitudinal force can be written as [13]

$$f_x = -\frac{m}{4}\frac{\partial v_q^2(x)}{\partial x}\left(1 - \cos(2\omega t)\right), \tag{2.63}$$

where the first part of the rhs is the ponderomotive force, as described in section 2.4.1, and the second half describes oscillatory motion of the electrons along the

target normal. Thus, bunches of electrons are pushed away from regions of high intensity while being accelerated at a frequency of $2\omega_L$.

This heating mechanism is viable for all laser polarisations apart from circular [6, 13, 63, 65] and performs best at low angular incidences and relatively long scale lengths[13].

2.7 Fast Electron Characteristics

In the previous section, a variety of mechanisms were discussed regarding how laser energy is coupled to bunches of electrons, otherwise known as fast/hot electrons. In the following section the amount of energy coupled from the laser to the energy, the characteristic temperature of the fast electron beam and the distributions expected will be discussed.

2.7.1 Fast Electron Temperatures and Distributions

The collisionless absorption mechanisms discussed in section 2.6.2 will couple a fraction of the laser energy, discussed in section 2.7.2, into a population of electrons. Due to the intensity of the laser considered, this will therefore lead to the electrons having far higher temperatures compared to the background electrons. The temperature, or mean energy, of these electrons has had several different scaling laws suggested [4, 73–75]. Beg et al (1997) [73] showed that for $\mathrm{I}_L < 10^{19}$ Wcm^{-2}, the temperature scaled as $\mathrm{T} \sim (I\lambda_L^2)^{0.33}$. For $\mathrm{I}_L\lambda_L \geqslant 10^{18}$ $\mathrm{Wcm}^{-2}\,\mu\mathrm{m}^2$ a commonly used scaling description is the ponderomotive scaling, associated to $\mathbf{j}\times\mathbf{B}$ heating, presented by Wilks et al (1992) [74] which is derived from equation 2.20 and is given as:

$$T_p(\mathrm{MeV}) \sim 0.511\left(\sqrt{1+\frac{I_{18}\lambda_L^2}{1.38\times10^{18}\,\mathrm{Wcm}^{-2}\,\mu\mathrm{m}^2}}-1\right), \tag{2.64}$$

where I_{18} is intensity in units of $\times10^{18}$ Wcm^{-2}.

Sherlock et al (2009) [75] suggested that T_p needed to be multiplied by a factor of 0.6 due to the fast electron beam being de-accelerated once they leave the absorption region.

Due to the large contrast in temperatures between the background electrons and electrons accelerated by the laser, it will subsequently mean that the fast electrons will not be represented by a Maxwellian distribution. Instead, a relativistic Maxwellian, otherwise known as the Maxwellian-Jüttner distribution, is used [76–79] and is of the form

$$f(\gamma) = \frac{\gamma^2 \beta}{\theta K_2(1/\theta)} \exp\left(-\frac{\gamma}{\theta}\right). \tag{2.65}$$

Where $\gamma = 1 \,/\, \sqrt{1 - v^2/c^2}$, $\beta = \frac{v}{c}$, $\theta = \frac{KT}{mc^2}$ and K_2 is a modified Bessel function of the 2^{nd} order.

While this may not completely represent the distribution of the fast electrons, it allows for the simplification of the problem so that fast electron transport can be studied in greater detail.

2.7.2 Fast Electron Conversion Efficiency

It is useful to determine the amount of laser energy coupled to fast electrons, denoted as β or $\eta_{L\to e}$. This parameter is found to be extraordinary complicated with almost all laser & target parameters impacting the final values [56]. Due to the complexities of directly probing a target, a variety of secondary mechanisms are used to characterize indirectly the fast electron beam propagation through the target. These include: K_α emission [21, 26–29, 32–34, 37, 38, 49, 50, 53, 54, 56, 59, 60, 71, 80–90], escaping fast electrons [21, 58, 82], Bremsstrahlung [21, 26, 82, 91] & fast ions [14, 21, 55, 82, 92] to name but a few. As well as this, lasers do not just couple their energy to fast electrons but also to hole punching ions too [56, 76, 93, 94], making the analysis into fast electron coupling even more complex. A review paper on the topic by Davies (2009) [56] presents an assortment of experimental and numerical values for both total absorption and fast electron absorption, a few of these will be presented here as well as more recent approaches by a variety of authors.

Ping et al (2008) [80] presents measurements of total absorption for short pulse lasers for $I_L\lambda_L^2$ between 10^{17} - 10^{20} $Wcm^{-2}\,\mu m^{-2}$. These p-polarised pulses were focused onto Si plates of 400 μm and Al foils varying in thickness 1.5 - 100 μm, with the varying thickness having no impact on the recorded results. Experimental results were found to match the numerical results, with the total absorption ranging between 10% for 10^{17} Wcm^{-2}, 80 - 90% for 10^{20} Wcm^{-2}. Davies (2009) [56] fitted an analytical fit for the relativistic laser intensities, $\geqslant 10^{18}$ Wcm^{-2}, suggesting that $\beta \propto (I\lambda^2)^{0.2}$.

There has also been a variety of work investigating fast electron conversion efficiency [21, 26, 56, 87, 88, 95]. Key et al (1998) [26, 56] presents experimental results from the Nova Laser Facility for $I_L\lambda_L^2$ between of 10^{19} - 10^{20} $Wcm^{-2}\,\mu m^{-2}$. Analysis of the results via a 3D Monte Carlo code & a 1D hydrodynamic code show that β increases with $I\lambda^2$, from 1% at low $I\lambda^2$ to 50% at high $I\lambda^2$ [56]. The Monte Carlo simulations assume non-realistic properties of the fast electrons: 1) no self-generated fields & 2) isotropic fast electron source. In conjunction with this, refluxing is also neglected in the simulations.

Myatt et al (2007) [87] & Nilson (2008) [88] both investigated very thin foils which included very strong refluxing. Both of these works found that for $I_L\lambda_L^2$ between 10^{17} - 10^{20} $Wcm^{-2}\,\mu m^{-2}$, β is 20% $\pm$ 10%. Chen et al (2009) [21] noted that both of these works neglected the energy transfer to fast ions, leading to the conversion efficiencies reported being the lower bounds of the value. Chen et al (2009) then went on to investigate the conversion into fast ions by using large non-refluxing targets, finding conversion efficiencies for fast electrons between 20-40%.

As it can be noted from the results from total absorption, Ping et al (2008) [80], and fast electron absorption, [21, 26, 56, 87, 88, 95], there is a noticeable difference between these two values due to the laser also coupling to ions or other electrons [56, 76, 93]. Work done by Levy et al (2013, 2014) [76, 93] has looked to elucidate the various coupling mechanisms in laser-solid interactions via a fully relativistic 1D analytical model of laser absorption via a kinematic approach. In this model, presented in Levy et al (2013) [76], particles directly excited by the laser are split into the two kinematic modes of ponderomotive absorption: hole punching, ions & electrons, and fast electrons. The evolution of these particles is described via the

Boltzmann-Vlasov equation, where collision coupling is considered to be insignificant and a "saddle-point" approximation of the Maxwellian-Jüttner distribution is used to describe the hole-punching particles and a Maxwellian-Jüttner distribution for the hole boring fast electrons. The model is solved by considering parameters of distribution function that satisfy the conservation of energy and momentum between the laser photons and the various particle species.

This approach allowed for the authors to present theoretical maxima and minima values for β [93] which, in terms of laser & target parameters, is

$$\frac{\sqrt{I_L\lambda_L^2}}{\sqrt{I_L\lambda_L^2}+1.5\sqrt{n_e}} \leq \beta \leq 1-\frac{1.2\times10^{18}}{I_L\lambda_L^2}. \tag{2.66}$$

Equation 2.66 prohibits high absorption values at low intensity and low absorption values at high intensity.

Work has also considered the optimisation of β in terms of laser-target parameters. For example, a variety of work has considered the effect of a pre-plasma scale length, as discussed in section 2.5.2, [49, 53, 54, 71]. Gray et al (2014) [53] investigated the optimum pre-plasma scale length by keeping the main 0.8 ps pulse at $I_L\lambda_L^2$ $\sim$1.2$\times$10^{20} Wcm^{-2} μm^{-2} while the second 5 ns pulse was varied between $I_L\lambda_L^2 = 0$ & 2$\times$10^{15} - 2$\times$10^{16} Wcm^{-2} μm^{-2} allowing for varying lengths of pre-plasma. Results showed that certain values of density gradient were conducive towards soft self-focusing of the laser pulse and increased coupling of laser energy to fast electrons, while stronger density gradients leads to strong self-focusing and filamentation of the laser. Increasing the density gradient again, past the filamentation stage, resulted in another density gradient conducive towards self-focusing of the beam.

The various work discussed above shows how complex defining β is. However, it is common for most work to assume β is between 0.2-0.5, with 0.3 being a commonly used value [4, 7, 14, 21, 56, 64, 77, 78, 96–106]. The reason for the window of 0.2 - 0.5 is that this is found to fit the window of experimental results, as discussed above, or presents an optimistic estimate for fast ignition [4].

2.8 Summary

This Chapter provides an introduction to a variety of topics in laser-solid interactions. First, the technique to generate ultra-relativistic pulses for short pulse lasers, CPA, is discussed. Following this, the Chapter focuses on the various physical phenomenon which occurs when a high power laser interacts with an over-dense target. Ionisation and electron motion in a laser are first discussed. This leads on to the introduction of the plasma, how a laser propagates through said plasma and the pre-plasma which is a by-product of a CPA system. After this, the various energy coupling mechanisms between the laser pulse and target are consider, ranging from inverse bremsstrahlung to $\mathbf{j}\times\mathbf{B}$ heating. Attention then focuses upon the conversion efficiency of these coupling methods and the various approaches to measure this.

Chapter 3

Fast Electron Transport Through A Medium

3.1 Introduction

In the previous Chapter, the various physical mechanisms involved in a high power laser, $a_0 > 1$, interaction with a solid target were discussed, with the final part detailing the production and characteristics of fast electrons. In this Chapter, the various physical phenomena occurring during the propagation of these fast electrons through a medium are discussed. Once more it must be noted that there are a variety of books, papers, lecture notes which present a very good description of the physics below. The author would like to acknowledge extensive use of the books: Gibbon (2004) [13], Eliezer (2002) [42], Atzeni (2004) [18], Salzmann (1998) [107] and papers: Robinson et al (2014) [4] throughout the duration of this Chapter.

3.2 Thomas Fermi (TF) Model

The heating of a target to high enough temperatures will lead to the liberation of electrons from atoms and thus ionisation of the target. If a full characterisation of the target is wanted at these temperatures then the effective ionisation state, Z^*, and Equation of State (EOS) of the target is required. To represent Z^*, the Thomas Fermi ionisation model is often used [18, 102, 107–111]. This ionisation

model is itself derived from the Thomas-Fermi (TF) Model which describes the EOS.

Originally presented separately [112] by Fermi (1927) [113] & Thomas (1927) [114], the TF model uses a statistical approach to describe the potential of high Z-neutral atoms [107]. The electrons are treated as a non-interacting quasi-classical Fermi gas in a self consistent Coulomb potential generated by all particles [18]. The original TF model made a variety of assumptions, including taking both electrons and nuclei at 0 K [107, 115]. However since then the TF model has undergone a variety of modifications and improvements [18, 107, 110, 112, 115–118]. Feynman et al (1949) [115] presented the modern grounding to the model, by using the TF model to produce equation of states (EOS) for high pressures and at various temperatures. More (1985) [118] presented analytical formulas, Appendix A, which allow for the approximation of Z^* without the need to solve the TF model [18, 107, 110]. The TF has also be used in conjunction with other models, with More et al (1988) [110] presenting a Quotidian Equation Of State (QEOS) which uses electron properties from the TF model, while taking ion motion from other models. One reason for such wide applications is that the TF model can be scaled to any Z, meaning that it has a wide applicability in various fields [18].

In what follows, the derivation of the TF model is presented following closely Atzeni (2004) [18] while also considering the description presented in Salzmann (1998) [107]. Any other references used will be noted throughout the derivation. A similar derivation to Atzeni (2004) [18] is also found in More et al (1988) [110].

The modern TF model starts by considering that the compound in question is represented via an average ion [18, 42]. Here, each ion is described by the average ionic charge and mass number of the compound, i.e. if a AuCH target was being considered it would be represented by the TF model as $\mathrm{Z}_{ionavg} = \mathrm{avg}(\mathrm{Z}_{Au} + \mathrm{Z}_C + \mathrm{Z}_H)$ and $\mathrm{A}_{ionavg} = \mathrm{avg}(\mathrm{A}_{Au} + \mathrm{A}_C + \mathrm{A}_H)$. This ionic sphere is then placed in the center of indistinguishable spherical cells, which cannot be penetrated by other ions. The radius is given as

$$R_{sc} = \left(\frac{3}{4\pi n_{ion}}\right)^{\frac{1}{3}} \tag{3.1}$$

where n_{ion}, the total ion density, is given by $n_{ion} = \frac{\rho}{A_{avg} m_p}$.

Inside each of these cells are Z (bound+free) electrons thereby making the cell neutral and thus no interaction takes place among the spherical cells. The energy of a single electron will now also include potential energy -eV(r), $\mathrm{E} = \frac{p^2}{2m} - \mathrm{eV}(r)$. This potential energy can be derived from Poisson's equation

$$-\nabla^2 V = \frac{e}{\epsilon_0}\left(\delta(\overrightarrow{r}) - n(r)\right). \tag{3.2}$$

Equation 3.2 shows that the potential energy arises from the ion core interaction with the electrons surrounding it. By considering a Fermi gas, the electron density in this spherical shell can be written as

$$n(r) = \frac{2}{\lambda_{th}^2} I_{1/2}\left(\frac{\mu + eV(r)}{k_B T}\right), \tag{3.3}$$

where λ_{th} is the DeBroglie wavelength, μ the chemical potential and $\mathrm{I}_{1/2}$ the Fermi-Dirac integral to the $\frac{1}{2}$ order. An nth order Fermi integral can be written as

$$I_n = \int_0^\infty \frac{z^n dz}{1 + exp\left(z - \frac{\mu}{k_b T}\right)}. \tag{3.4}$$

The boundary conditions for the potential can be written as

$$\frac{dV}{dr} = 0 \text{ at } r = R_{sc} \tag{3.5}$$

and

$$V(r) \propto \frac{Ze}{r} \text{ for } r \to 0. \tag{3.6}$$

The TF model requires that equations 3.2 & 3.3 are satisfied simultaneously so that self-consistency is maintained. After the calculation of these two equations, it allows for the total kinetic energy, U_{KE}, Coulomb energy between neutrals and electrons, U_{Cen}, and Coulomb energy between electrons, U_{Cee}, to be written as

$$U_{KE} = \frac{3}{2} k_B T \frac{2}{\lambda_{th}^3} \int d^3 r I_{\frac{3}{2}} \left(\frac{\mu + eV(r)}{k_B T} \right), \tag{3.7}$$

$$U_{Cee} = \frac{e^2}{2} \int d^3 r d^3 r' \, \frac{n(r) n(r')}{|\mathbf{r} - \mathbf{r}'|} \tag{3.8}$$

$$U_{Cen} = - \int d^3 r n(r) \frac{Z e^2}{r}. \tag{3.9}$$

From here the thermodynamic properties of internal energy, free energy and entropy, in terms of per mass, can be calculated

$$E_e = \frac{U_{KE} + U_{Cee} + U_{Cen}}{A m_p}, \tag{3.10}$$

$$F_e = \frac{Z\mu - \frac{2U_{KE}}{3} - U_{Cee}}{A m_p}, \tag{3.11}$$

$$S_e = \frac{\frac{5U_{KE}}{3} - Z\mu + U_{Cen} + 2U_{Cee}}{A m_p T}, \tag{3.12}$$

and the pressure can be written as

$$p_e = n(R_{sc}) k_B T \frac{I_{\frac{3}{2}}(\mu / k_B T)}{I_{\frac{1}{2}}(\mu / k_B T)}. \tag{3.13}$$

This coincides with the Fermi gas pressure of free electrons which have a density at the spherical cell boundary of

$$n(R_{sc}) = \frac{2 I_{\frac{1}{2}}(\mu / k_B T)}{\lambda_{th}^3}. \tag{3.14}$$

The free electrons per ion sphere can be written as

$$Q = \frac{4\pi R_{sc}^3}{3} n(R_{sc}). \tag{3.15}$$

As stated previously, a major strength of the TF model is that it scales with Z. Thus by solving for hydrogen, denoted by the subscript 1, basic scaling parameters can be used for any Z

$$r = \frac{r_1}{Z^{\frac{1}{3}}}, \tag{3.16}$$

$$n(r) = Z^2 n_1(r_1), \tag{3.17}$$

$$V(r) = Z^{\frac{4}{3}} V_1(r_1). \tag{3.18}$$

The scaling for the density and temperature can be written as

$$\rho_1 = \frac{\rho}{AZ}, \; T_1 = \frac{T}{Z^{\frac{4}{3}}}, \tag{3.19}$$

Finally the scaling for free electrons, chemical potential, pressure and the various thermodynamic properties can be written as

$$\begin{aligned} Q(Z,\rho,T) &= ZQ_1(\rho_1, T_1) \\ p(Z,\rho,T) &= Z^{\frac{10}{3}} p_1(\rho_1, T_1) \\ \mu(Z,\rho,T) &= Z^{\frac{4}{3}} \mu_1(\rho_1, T_1) \\ E(Z,\rho,T) &= \frac{Z^{\frac{7}{3}}}{A} E_1(\rho_1, T_1) \\ S(Z,\rho,T) &= \frac{Z}{A} S_1(\rho_1, T_1) \\ F(Z,\rho,T) &= \frac{Z^{\frac{7}{3}}}{A} F_1(\rho_1, T_1). \end{aligned} \tag{3.20}$$

To utilise More (1985) [118] method, the number of free electrons, Q, is only required [18]:

$$Z^* = Q(Z,\rho,T). \tag{3.21}$$

It must be noted that there are a variety of issues with the TF model EOS. For example, it fails to represent real matter features at low temperature close to solid density and below. As well as this, it fails to describe zero pressure of solid matter nor does it separate between gas, fluid and solid phases. Work has been done to rectify this, with the inclusion of quantum corrections to account for the binding energy [18]. As well as this the TF model neglects a variety of aspects in the calculations, including both relativistic and quantum effects, apart from Fermi statistics, [107, 110] and the role of atomic shell effects[107].

Desjarlais (2001) [108] noted that due to the TF model neglecting the quantum shell effects on ionisation equilibrium, it leads to ionisation levels beyond the predicted values. Desjarlais suggested a blended weight of the TF and single ionisation Saha model with pressure ionisation correction. This allows for a smooth transition between the two in regions where the non-ideal Saha model, f_e, is $<< 1$.

The Saha ionisation model is often used to describe the ratio of two adjacent charge states of a dilute plasma in local thermal equilibrium (LTE) and a large λ_D. The general form is given as [18, 107]

$$n_{i+1} = n_i \frac{2}{n_e \lambda_{th}^3} \frac{g_{i+1}}{g_i} \exp\left(-\frac{I}{k_B T}\right) \tag{3.22}$$

where I is the ionisation energy of an ion with charge state i, g_i is the degeneracy of the state for i-ions and i is the charge state of the ion.

The Saha ionisation underestimates non-ideal plasmas where pressure ionisation can occur due to modifications to ionisation energies by interacting electrons and ions.

The Dejarlias corrections use a single ionisation form of the Saha ionisation equation with a pressure ionisation correction, which is given as

$$K = \frac{2g_1}{g_0} \frac{1}{n_i \lambda_{th}^3} \exp\left[-\frac{I}{k_B T}\left(1 - \left(\frac{1.5e^2}{I R_{sc}}\right)^{\frac{3}{2}}\right)\right]. \tag{3.23}$$

g_0 & g_1 denote the ground state of the neutral atom and singly ionised atom respectively and $\left(\frac{1.5e^2}{IR_{sc}}\right)^{\frac{3}{2}}$ is the semi-empirical pressure ionisation correction.

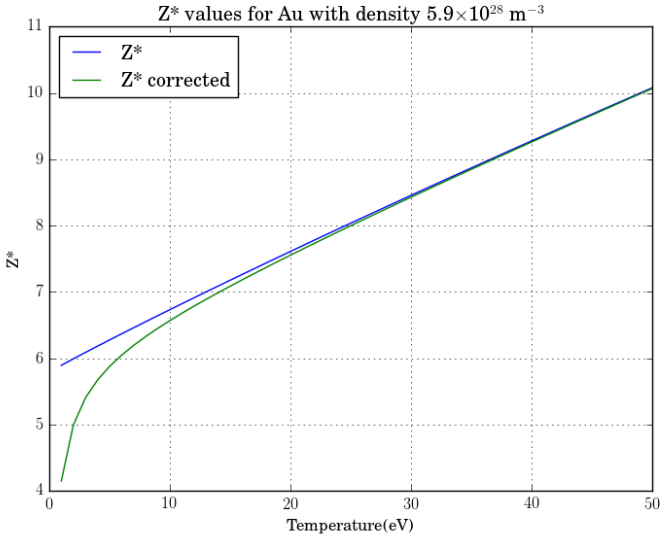

FIGURE 3.1: Plot showing Thomas Fermi Z^*, blue line, vs Desjarlais (2001) Z^* corrections, green line, for an Au target with $n_e = 5.9\times10^{28}$ m^{-3}. Z^* was calculated via More (1985) method, Appendix A.

The total contribution of the Saha ionisation in the corrections is

$$f_e = \frac{1}{2}\left(\sqrt{K^2 + 4K} - K\right). \tag{3.24}$$

The calculation of Z^* with these two models is therefore written as

$$Z^*_{corr} = f_e^{\frac{2}{Z^2_{TF}}} Z_{TF} + \left(1 - f_e^{\frac{2}{Z^2_{TF}}} Z_{TF}\right) f_e. \tag{3.25}$$

A plot showing Z^* and Z^*_{corr} for an Au target, n_i=5.9×10^{28} m^{-3}, for temperatures between 1-50 eV can be found in figure 3.1.

3.3 Resistivity of a Medium

The resistivity, η, determines how strongly a material will inhibit the propagation of an electric current. Physically, this inhibition can be seen as the conversion of the kinetic energy to thermal energy. This resistivity will depend on a variety of properties including, but not limited to: ionic structure, ionisation state and

temperature [13, 14]. In the context of fast electron transport, it can be seen that evolution of the resistivity will be crucial to governing the characteristics of the fast electron beam. In the following section, two resistivity regimes encountered in this transport, namely plasma & WDM, will be discussed.

3.3.1 Plasma

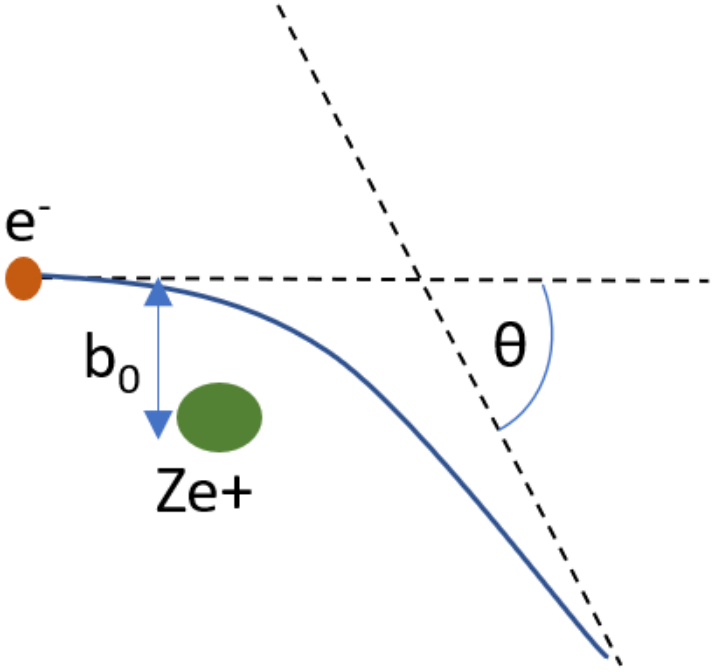

FIGURE 3.2: Coulomb collision between an electron and ion [67].

Once a target is heated to large enough temperatures, the target will start to enter the plasma state, as introduced in section 2.5. Electrons are no longer bound to atoms and therefore solid state resistivity is no longer applicable. Instead, it is assumed that resistivity will primarily arise from Coulomb collisions between the particles [42, 67, 68, 70]. A simple diagram of a Coulomb collision is found in figure 3.2.

The force from a Coulomb collision between an electron and ion can be written as [42, 67, 68, 70]

$$F_{ei} = -\frac{Ze^2}{4\pi\epsilon_0 r^2}, \tag{3.26}$$

where r is the distance between the two particles.

Electrons will feel this this force for a time t, which is written as

$$t \approx \frac{b}{v_e}, \tag{3.27}$$

where b is the impact parameter and can be defined as

$$b = \frac{Ze^2}{4\pi\epsilon_0 m_e v_e^2} \frac{1}{\tan\left(\frac{\theta}{2}\right)}, \tag{3.28}$$

where θ is the scattering angle.

To describe the collisions in a plasma, b is often taken at its two limits: b_{max} & b_0. b_{max} is taken to be the Debye length, equation 2.27, and represents small angle collisions, while b_0 is is the impact parameter for large angle collisions with $\theta = 90°$. In the large angle collision limit, the change in electron momentum can be written as

$$\Delta p = \frac{Ze^2}{4\pi\epsilon_0 m_e v_e}. \tag{3.29}$$

The Coulomb cross section can then be defined as

$$\sigma = \pi b_0^2 = \frac{Z^2 e^4}{16\pi\epsilon_0^2 m_e^2 v_e^4}. \tag{3.30}$$

By then using the electron-ion collision frequency, $\nu_{ei} = n_e \sigma v_e$, the resistivity can be written as

$$\eta = \frac{m_e}{n_e e^2}\nu_{ei} = \frac{Ze^2}{16\pi\epsilon_0^2 m_e v_e^3}. \tag{3.31}$$

To also account for small angle collisions the Coulomb logarithm is introduced,

$$\ln\Lambda = \ln\left(\frac{b_{max}}{b_0}\right) = \ln\left(\frac{\lambda_D}{b_0}\right). \tag{3.32}$$

This represents the ratio between the maximum and minimum impact parameters with typical values ranging between 5 - 15.

The definition of the Coulomb logarithm allows for the Spitzer resistivity to be defined as

$$\eta = \frac{m_e}{n_e e^2}\nu_{ei}\ln\Lambda = \frac{Ze^2}{16\pi\epsilon_0^2 m_e v_e^3}\ln\Lambda. \tag{3.33}$$

By assuming a Maxwellian velocity, equation 3.33 can be denoted in the following reduced form[42, 68, 77, 78, 100, 101, 119]

$$\eta = 10^{-4}\frac{Z\ln\Lambda}{T^{\frac{3}{2}}}. \tag{3.34}$$

3.3.2 Resistivity of Warm Dense Matter (WDM)

The heating of a solid target will not result in creating a plasma state immediately but the target will instead enter an intermediate state between a cold target and hot plasma, commonly referred to as Warm Dense Matter (WDM) [4, 14, 28, 38, 120–125]. This regime, which exists between temperatures of 0.1 - 100 eV and densities of 0.1 - 10 solid density, is characterised by strong coupling $\Gamma \gtrsim 1$ and degenerate matter $\theta \lesssim 1$ where [120, 125]

$$\Gamma = \frac{\left(Z^*\right)^2 e^2}{4\pi\epsilon_0 R_{sc} k_B T} \tag{3.35}$$

and

$$\theta = \frac{T}{T_F}. \tag{3.36}$$

T_F is the Fermi temperature and is given as

$$T_F = \frac{E_F}{k_B} = \frac{1}{k_B}\left(\frac{\hbar^2}{2m}\left[3\pi^2 n_e\right]^{\frac{2}{3}}\right), \tag{3.37}$$

where E_F is the Fermi energy.

Due to having to account for both of this effects, the modelling of the various physical properties in WDM is found to be extremely complex. A variety of resistivity models have been suggested [4, 38, 124–127] with no model being fully settled upon. In what follows, two resistivity models: Lee-More [127] and Robinson [124] are presented.

As with many resistivity models, the Lee-More & Robinson descriptions both start from the relaxation time approximation (RTA) [66, 124, 127] for the Boltzmann Transport Equation which can be written as [66, 124, 127]

$$\frac{\partial f_s}{\delta t} + \mathbf{v_s} \cdot \frac{\partial f_s}{\partial \mathbf{r}} - \frac{\mathbf{F_s}}{m_s} \cdot \frac{\partial f_s}{\partial \mathbf{v}} = -\frac{f - f_0}{\tau_c}, \tag{3.38}$$

where the subscript s denotes the species of the particle, F_s is the Lorentz force for the particle, equation 2.12, f the distribution of said species, f_0 the distribution in equilibrium and τ_c the electron relaxation time. Thus equation 3.38 shows that the distribution function, f, will relax towards its equilibrium state, f_0, in characteristic time τ_c [66].

Both models also consider the system in steady state, $\frac{\partial}{\partial t} = 0$, and by also neglecting $\mathbf{B}$, allows for equation 3.38 to be written as

$$\mathbf{v_s} \cdot \frac{\partial f_s}{\partial \mathbf{r}} - \frac{e}{m_s}\mathbf{E} \cdot \frac{\partial f_s}{\partial \mathbf{v}} = -\frac{f - f_0}{\tau_c}. \tag{3.39}$$

As well as this, both models are predicated upon the Thomas-Fermi ionisation model, section 3.2, and the Fermi-Dirac distribution which is used to describe the degeneracy of electrons.

3.3.2.1 Lee-More Model

The Lee-More model [127] is a semi-analytical model which produces various transport coefficients for a variety of states of matter, ranging from plasma to solid, liquids & neutral gases, at various temperatures and densities, which leads to it being widely used [4, 38, 97, 102, 103, 108, 111, 121, 124, 127–131].

The electron relaxation time τ_c, equation 3.38, is written as

$$\frac{1}{\tau_c} = \frac{1}{\tau_{ei}} + \frac{1}{\tau_{en}}, \tag{3.40}$$

where

$$\frac{1}{\tau_{ei}} = \frac{1}{n_i v \sigma_{ei}}, \tag{3.41}$$

and

$$\frac{1}{\tau_{en}} = \frac{1}{n_n v \sigma_{en}}, \tag{3.42}$$

are the collision rates for electron ion and electron neutral respectively. n_i is the ion density, n_n the neutral density and σ is the electron-ion and electron-neutral momentum transfer cross section respectively.

Partial wave calculations, which solve Schröndinger equation for Thomas-Fermi potentials, are used to calculate cut-off parameters for the momentum transfer cross section which is

$$\sigma_{tr} = \frac{4\pi \left(Z^*\right)^2 e^4 \ln\Lambda}{m^2 v^4}. \tag{3.43}$$

The Coulomb logarithm, ln Λ, takes a different form from equation 3.32 with the Lee-More approach being written as [4]

$$\ln\Lambda = \max\left[2, \frac{1}{2}\ln\left(1 + \frac{b_{max}^2}{b_{min}^2}\right)\right]. \tag{3.44}$$

The b_{max} parameter is written as[4]

$$b_{max} = \sqrt{\lambda_D^2 + R_{sc}^2}, \tag{3.45}$$

where λ_D is the Debye length which includes a degenerate correction factor and R_{sc}, defined in equation 3.1, is the inter-atomic distance. λ_D is rewritten to include degenerate effects

$$\frac{1}{\lambda_D^2} = \frac{n_e e^2}{\epsilon_0 k_B \sqrt{T_e^2 + T_F^2}} + \frac{n_i \left(Z^*\right)^2 e^2}{\epsilon_0 k_B T_i}. \tag{3.46}$$

The R_{sc} factor is included to account for high density plasmas where λ_D breaks down due to strong ion-ion correlation effects. The inter-atomic distance applies to highly disordered materials and, as such, it is often common for this to be multiplied by a value ranging between 2-8 when considering different structured materials[4, 38, 97, 102, 103, 111, 128].

The b_{min} parameter is written as [4]

$$b_{min} = \sqrt{b_{Cmin}^2 + b_{Qmin}^2}, \tag{3.47}$$

where b_{Cmin} is the distance of closest approach and b_{Qmin} is the de Broglie wavelength.

This allows the resistivity, with no **B** effects, to be written as

$$\eta = \frac{m_e}{n_e e^2 \tau} \left[A^\alpha \left(\frac{\mu}{k_b T} \right) \right]^{-1}, \tag{3.48}$$

$A^\alpha \left(\frac{\mu}{k_b T}\right)$ accounts for electron degeneracy and can be written as

$$A^\alpha \left(\frac{\mu}{k_b T} \right) = \frac{4}{3} \frac{I_2}{1 + \exp\left(-\frac{\mu}{k_b T}\right) \left(I_{\frac{1}{2}}\right)^2}. \tag{3.49}$$

where I_n is the Fermi integral, equation 3.4.

In the fully degenerate limit, $\left(\frac{\mu}{k_B T} \to \infty\right)$, $A^\alpha = 1$ while in the non-degenerate limit, $\left(\frac{\mu}{k_B T} \to -\infty\right)$, $A^\alpha = \frac{32}{3\pi}$ which produces the Spitzer resistivity.

Due to the Lee-More model considering non-plasma states, the τ_c variable in equation 3.40 will be incorrect in these states due to the strong ion correlation, which in turn will mean that the mean free path (mfp) of the electrons will be incorrect. To account for this the Lee-More model uses a melt temperature, T_m, which is defined as

$$T_m \text{ (eV)} = 0.32 \left[\frac{\epsilon}{1+\epsilon}\right]^4 \epsilon^{2b-\frac{2}{3}}, \tag{3.50}$$

where $b = 0.6Z^{\frac{1}{9}}$ and $\epsilon = 9.0Z^{0.3}\frac{\rho}{A}$.

For temperatures lower than this, the mean free path of the electrons is

$$\Lambda = 50R_{sc}\left(\frac{T_m}{T}\right) \tag{3.51}$$

while for temperatures above this

$$\Lambda = 50R_{sc}\left(\frac{T_m}{T}\right)\left(\frac{1}{\gamma}\right) \tag{3.52}$$

where γ is chosen for each material to account for the increase in resistivity at melting. At temperatures beyond the T_m there are values in which $\Lambda < R_{sc}$, due to this the relaxation time is assumed to be $\tau = \frac{R_{sc}}{\bar{v}}$.

Lee-More also considers an arbitrary magnetic field. From equation 2.12 it can be seen for any particle parallel to the magnetic field that the resistivity will reduce to the case with no **B**. For particles which are not parallel to this field, the resistivity can be written as

$$\eta_\perp = \frac{m_e}{n_e e^2 \tau}\left[A_\perp^\alpha\left(\frac{\mu}{k_b T}, \omega_e, \tau\right)\right]^{-1} \tag{3.53}$$

where the degeneracy parameter now accounts for the electron relaxation time, τ and electron gyro-frequency, ω_e.

Desjarlais (2001) [108] presented a variety of corrections to the Lee-More model with the Z^* corrections from this work already presented in section 3.2. Other

corrections include the inclusion of electron-electron scattering. Desjarlais also reformulates the electron-neutral collision cross section by using a fit to a momentum transfer cross section presented by Redmer (1999) & Kuhlbrodt et al (2000) [125, 129] who calculated this by using the screened polarisation potential in the Born approximation. The cross section can be written as

$$\sigma_{en} = \frac{\pi^3 \left(\frac{\alpha_D}{2r_0 a_B}\right)^2}{A^2 + 3Bkr_0 + 7.5C\left(kr_0\right)^2 - 3.4D\left(kr_0\right)^3 + 10.6668E\left(kr_0\right)^4} \tag{3.54}$$

where k is the wavenumber of the electron, α_D is the dipole polariazbility and $r_0 = \sqrt[4]{\alpha_D a_B \left(2Z^{\frac{1}{3}}\right)^{-1}}$ is the cut-off radius. The five lettered parameters are given as

$$A = 1 + 2\kappa r_0 + \frac{7}{\pi^2}\left(\kappa r_0\right)^2 + \frac{\pi}{7}\left(\kappa r_0\right)^3, \tag{3.55}$$

$$B = \exp(-18\kappa r_0) \tag{3.56}$$

$$C = \frac{1 + 22\kappa r_0 - 11.3\left(\kappa r_0\right)^2 + 33\left(\kappa r_0\right)^4}{1 + 6\kappa r_0 + 4.7\left(\kappa r_0\right)^2 + 2\left(\kappa r_0\right)^4}, \tag{3.57}$$

$$D = \frac{1 + 28\kappa r_0 + 13.8\left(\kappa r_0\right)^2 + 3.2\left(\kappa r_0\right)^3}{1 + 8\kappa r_0 + 10\left(\kappa r_0\right)^2 + \left(\kappa r_0\right)^3}, \tag{3.58}$$

$$E = 1 + 0.1\kappa r_0 + 0.3665\left(\kappa r_0\right)^2, \tag{3.59}$$

where κ is the screening wavenumber.

While the Lee-More model produces a variety of useful results, it is not without its own pitfalls. Robinson et al (2015) [124] noted that electron-impact ionisation, which is neglected in Lee-More, plays a role in the overall resistivity. The Lee-More model also neglects the ionic structure which will hamper the resistivity model at lower temperatures [14].

3.3.2.2 Robinson Resistivity

Another approach to WDM resistivity is the Robinson Resistivity. Presented in Robinson et al (2015) [124] this model investigates non-crystalline carbon, though it is applicable with relative cross sections for any material, primarily between 5-30 eV with inclusion of electron-impact ionisation and electron-impact excitation processes. The model is predicated upon the following assumptions

1. Jellium Approximation: free electrons are represented as a uniform electron gas of arbitrary degeneracy.
2. Randium Approximation: ions are assumed to be highly disordered.

As well as these two assumptions, the Lindhard theory is used to calculate the electrostatic screening length. In this approach to screening the applied electric field, E_{app}, to a material can be written as [132]

$$E_{app} = \frac{E_{tot}}{\epsilon\left(\mathbf{q},\omega\right)}, \tag{3.60}$$

where E_{tot} is total applied field to the material, $\mathbf{q}$ is the wavevector of the perturbation, ω is the frequency of the perturbation and $\epsilon\left(\mathbf{q},\omega\right)$ is the dielectric function which can be written as [132]

$$\epsilon\left(\mathbf{q},\omega\right) \equiv 1 + \frac{e^2}{\epsilon_0 \mathbf{q^2}} \sum_{\mathbf{k}} \frac{f^0(\mathbf{k}) - f^0(\mathbf{k}+\mathbf{q})}{E(\mathbf{k}+\mathbf{q}) - E(\mathbf{k}) - \hbar(\omega - i\alpha)} \tag{3.61}$$

where $\mathrm{f}^0(\mathbf{k})$ is the probability of particle state k being occupied, E(k) is the energy of the particle state k and α is a slowly growing time constant.

In the static limit, $\omega \to 0$, equation 3.61 becomes

$$\epsilon\left(\mathbf{q},\omega\right) = 1 + \frac{\kappa_s^2}{\mathbf{q^2}}, \tag{3.62}$$

where κ_s is the screening wavenumber and can be written as

$$\kappa_s = \frac{1}{l_s} = \sqrt{\frac{e^2}{\epsilon_0}\frac{\partial n}{\partial \mu}}, \tag{3.63}$$

where l_s is the screening length and $\frac{\partial n}{\partial \mu}$ is the change in electron density with respect to the chemical potential.

l_s is dependent on the state of the system, with a degenerate system using the Thomas-Fermi screening length and non-degenerate systems using the Debye length. A plot of the Lindhard theory can be found in Chapter 5, figure 5.6.

The Robinson model starts by considering an electric field **E** acting on a system whose momentum space is described via spherical-polar coordinates. The perturbation to the electrons distribution can therefore be written as [124]

$$f = f_0(\mathbf{p}) + f_1(\mathbf{p})\ \cos\theta, \tag{3.64}$$

where θ is polar angle, p the magnitude of the momentum, f_0 is the isotropic part of the distribution and f_1 the anisotropic part.

By considering the electric field to be uniform, neglecting $\frac{\partial}{\partial \mathbf{r}}$ term in 3.39, and $\mathbf{E}\frac{\partial f_1}{\partial \mathbf{p}}$, the anisotropic part of the distribution function can be written as [66, 124]

$$f_1 = \tau(\mathbf{p}) e \mathbf{E} \frac{\partial f_0}{\delta \mathbf{p}} \tag{3.65}$$

where $\tau(\mathbf{p})$ is the collision time for electron and its inverse, $\nu(\mathbf{p})$ is the frequency of collisions.

From transport theory, the current density can be written as [66]

$$\mathbf{J} = -e \int \mathbf{v} f d^3\mathbf{p}. \tag{3.66}$$

Multiplying equation 3.67 by $\frac{m_e}{m_e}$ gives:

$$\mathbf{J} = -\frac{e}{m_e} \int \mathbf{p} f d^3\mathbf{p}. \tag{3.67}$$

Now integrating this over azimuthal and polar coordinates and considering equation 3.65, the current density can be written as

$$\mathbf{J} = -\frac{4\pi e^2 \mathbf{E}}{3m_e} \int_0^\infty \mathbf{p}^3 \tau(\mathbf{p}) \frac{\partial f_0}{\partial \mathbf{p}} d\mathbf{p} \tag{3.68}$$

Using the microscopic form of Ohm's law

$$\mathbf{E} = \eta \mathbf{J}, \tag{3.69}$$

the resistivity from this model can be considered as

$$\eta = \frac{3m_e}{4\pi e^2} \left[\int_0^\infty \mathbf{p}^3 \tau(\mathbf{p}) \left| \frac{\partial f_0}{\partial \mathbf{p}} \right| \mathrm{d}\mathbf{p} \right]^{-1} \tag{3.70}$$

The collision time, $\tau(\mathbf{p})$, is given by

$$\sum_j = \frac{1}{\tau_j} \tag{3.71}$$

where τ_j is the jth collision.

τ is found to consist of a variety of collisions which will be discussed below.

Electron-ion collisions

The Robinson Resistivity model uses the Quantum Lenard-Balescu (QLB) equation to describe electron-ion collisions. A dynamically screened Coulomb potential will have an e-i collision time given by

$$\frac{1}{\tau_{ei}} = \frac{Z^* e^4 n_e m_e}{4\pi \epsilon_0^2 p^3} \int_0^{\frac{2p}{\hbar}} \frac{k^3}{\left(k^2 + \kappa_s^2\right)^2} dk \tag{3.72}$$

where k=$\frac{p}{\hbar}$ is the electron wavenumber.

Analytical integration of equation 3.72 produces the electron-ion collision time

$$\frac{1}{\tau_{ei}} = \frac{Z^* e^4 n_e m_e}{4\pi \epsilon_0^2 p^3} \left[\log\left(\sqrt{1 + \frac{\phi^2}{\kappa_s^2}} \right) - \frac{1}{2} \frac{\frac{\phi^2}{\kappa_s^2}}{1 + \frac{\phi^2}{\kappa_s^2}} \right], \tag{3.73}$$

where $\phi = \frac{2p}{\hbar}$. Unlike the Coulomb logarithm employed in the Lee-More and Spitzer resistivity this Coulomb logarithm does not require for artificial cut-offs parameters.

A structure factor $S_{ii}(k)$, assumed to be 1 here, can be added into the integral of equation 3.73 to allow for the model to consider other ionic structures.

Electron-Electron collisions

To include electron-electron collisions, the electron-ion collisions are multiplied by a reduction factor which accounts for the degeneracy of the electrons

$$\gamma = \gamma_{nd} + (1 - \gamma_{nd}) \times \frac{T_F}{T_F + \frac{3}{2}T}, \tag{3.74}$$

where γ_{nd} is the reduction factor in the non-degenerate limit and is written as

$$\gamma_{nd} = \frac{3\pi}{32}\left(1 + \frac{153Z^2 + 509Z}{64Z^2 + 345Z + 288}\right). \tag{3.75}$$

Electron-neutral collisions

The electron-neutral collisions follow the Desjarlais corrections presented in the previous section, equations 3.54 - 3.59, with the scattering time in this model being written as

$$\tau_{en} = \frac{1}{n\sigma_{en}v_e} \tag{3.76}$$

where v_e is the magnitude of the velocity.

Electron-impact excitation

The authors also considered the various shell transitions of bound electrons for Carbon atoms with +1 to +3 charge. The collision time was given as

$$\tau_{eimpact} = \frac{1}{n\sigma_{eie}v_e}. \tag{3.77}$$

σ_{eie} is the electron-impact cross section and is dependent upon the material in question.

3.4 Fast Electron Transport

With the description of the materials ionisation state and response to an electric current, the physical properties of this fast electron beam can now be described. In the following sections the various physical characteristics and mechanisms of fast electron transport will be considered.

3.4.1 Return Current

In section 2.6.2, a variety of mechanisms were presented which result in the generation of fast electrons in solid targets with $\mathbf{j} \times \mathbf{B}$ heating being the pre-eminent method in relativistic lasers. The number of fast electrons generated can be considered from energy conservation [13]

$$\frac{\beta I_L}{\epsilon_f} = n_f v_f \tag{3.78}$$

where β is the laser-fast electron conversion efficiency, as defined in section 2.7.2, ϵ_f is the ponderomotive energy of the fast electrons, equation 2.64, and v_f is the velocity of the fast electrons.

Taking $\beta = 0.3$, $\mathrm{I}_L = 2{\times}10^{19}$ Wcm^{-2}, $\lambda_L = 1$ μm, $\mathrm{v} = 3{\times}10^8$ ms^{-1} results in ϵ_f to be 1.5 MeV, thus giving a fast electron density of $\sim 8{\times}10^{26}$ m^{-3}. The current density of this beam can be calculated via

$$\mathbf{j}_f = -e n_f \mathbf{v}_f, \tag{3.79}$$

resulting in $\mathbf{j}_f \sim 4{\times}10^{16}$ Am^{-2}.

The fast electron current can be estimated via

$$I_f = \frac{\beta e I_L \pi r^2}{\epsilon_f} \tag{3.80}$$

where r^2 is the radius of the laser spot. Taking this to be 5 μm and using the values from above, we see that $I_f \approx 3$ MA.

The electric field generated by this fast electron beam can be estimated via Maxwells' equation in 1D in vacuum, $\mathbf{E} \approx \frac{\mathbf{j}_f t}{\epsilon_0}$. Thus at 100 fs, the electric field is $\sim 10^{14}$ Vm^{-1} which is enough to stop the fast electron in distances $< \mu$m [3, 4].

In conjunction with this, the maximum current allowed to propagate through a target before self generated magnetic field deflects it back is given by the Alfvén limit [18, 23, 64, 106, 133]

$$I(kA) = \frac{4\pi}{e\mu_0}\mathbf{p}_e = 17\beta\gamma. \tag{3.81}$$

where $\mathbf{p}_e$ is the electron momentum.

This current is limited to the kilo-Amp regime but as stated above, values in the mega-Amp and beyond are typical for fast electrons. Thus there must be a neutralising current which allows for the propagation of this fast electron beam through a solid target. This neutralising current is often regarded as the return current, $\mathbf{j}_b$ and the current balance is of the form [3, 4, 6, 13, 28, 29, 106, 134, 135]

$$\mathbf{j}_f + \mathbf{j}_b \approx 0. \tag{3.82}$$

One question which arises from this neutralisation is if whether this relation holds locally. Bell et al (2006) [3] demonstrated that this must occur. Consider two counter propagating currents of the same magnitude, whose radii are given as r_f and $r_b = r_f + \delta r$, where δr is the difference between the two radii. The current densities are $\mathbf{j}_f = \frac{I}{\pi r_f^2}$ and $\mathbf{j}_b = \frac{I}{\pi r_b^2}$ respectively and the magnetic field is therefore

$$B = \frac{\mu_0 I}{2\pi}\begin{cases} r(r_f^{-2} - r_b^{-2}) & \text{if } r < r_f, \\ r^{-1} - r r_b^{-2} & \text{if } r_f < r < r_b, \\ 0 & \text{if } r_b < r. \end{cases} \tag{3.83}$$

In the case where $\delta r << r_f$, the maximum magnetic field strength is $\mu_0 I \left(\frac{\delta r}{r_f}\right)/\pi r_f$ and the magnetic energy per unit length is $\mu_0 I^2 \left(\frac{\delta r}{r_f}\right)^2/4\pi$. By considering $r_f = 10$

μm and I = 50 MA, the maximum magnetic field strength is therefore $2{\times}10^6 \left(\frac{\delta r}{r_f}\right)$ T while the magnetic energy per unit length is 250 $\left(\frac{\delta r}{r_f}\right)^2$ Jμm^{-1}. As the magnetic energy cannot exceed the maximum magnetic field strength, the current must neutralise locally.

Two other defining characteristics can be noted from above: 1) while $\mathbf{j}_f$ & $\mathbf{j}_b$ have similar magnitudes the physical characteristics of the beam are in stark contrast, with the fast electron current having velocities v $\approx$ c and mean free paths will usually be larger than the target in question, while the return current is much slower and therefore both far more collisional and more dense[28]. 2) The current neutralisation is not exact, which leads to the generation of resistive EM fields [4, 136]. Due to the neutralisation not being exact, the approximation

$$\nabla \times \mathbf{B} \approx \mu_0 \left(\mathbf{j}_f + \mathbf{j}_b\right), \tag{3.84}$$

is often used.

Both of these characteristics are explored in the following sections, with 1) being discussed in section 3.4.2 and 2) being discussed in section 3.4.3.

3.4.2 Fast Electron Heating

The description of heating by these two currents starts from the Bloch-Bethe formula [4, 28, 48]. This describes the average energy loss (dE) per unit length (dx) of electrons via radiative losses and small-angle collisions. For electrons with kinetic energies > 10 keV, this is written as:

$$\frac{dE}{dx} = -\frac{e^4 n_e}{8\pi\epsilon_0^2 m_e v_f^2}\left[\ln\frac{(\gamma-1)(\gamma^2-1)}{2\left(J/m_e c^2\right)^2} + \frac{1}{\gamma^2} - \frac{2\gamma-1}{\gamma^2}\ln 2 + \frac{1}{8}\frac{(\gamma-1)^2}{\gamma^2}\right] \tag{3.85}$$

where J is the mean ionisation potential

Radiative losses, such as bremsstrahlung, are neglected in target heating due to the low absorption cross section [28]. $\frac{dE}{dx}$ is dependent on the target density ρ,

with higher density target suffering higher losses.

For a volume $\pi r_f^2 dx$ and volumetric specific heat capacity C, the heating in time by fast electrons can be written as

$$C\frac{dT}{dt}\bigg|_{coll} = \left\langle \frac{\mathbf{j}_f}{e} \left| \frac{dE}{dx} \right| \right\rangle \tag{3.86}$$

where the heating does not directly depend on the radius of the beam.

While the heating via the return current is,

$$C\frac{dT}{dt}\bigg|_{Ohm} = \eta \mathbf{j}_f^2. \tag{3.87}$$

Combining equations 3.86 & 3.87 produces the total heating of a target as

$$C\frac{dT_e}{dt} = \left\langle \frac{\mathbf{j}_f}{e} \left| \frac{dE}{dx} \right| \right\rangle + \eta \mathbf{j}_f^2. \tag{3.88}$$

Due to the Ohmic heating component scaling with $\mathbf{j}_f^2$ and fast electron mfp being longer than most targets considered, Ohmic heating is often considered the dominant heating mechanism in solid targets. Due to this, it is often common to only consider the heating performed via Ohmic heating [98]. In these scenarios, equation 3.88 is often written in the form [77, 78, 100, 128, 136–139]

$$\frac{\partial T}{\partial t} = \frac{\eta \mathbf{j}_f^2}{C}. \tag{3.89}$$

Thermal conduction is usually neglected in this approach [136]. Temperatures from Ohmic heating can reach the keV range in ps time scales [4]

However it can be seen from equations 3.85 and 3.88 that Ohmic heating is independent of the background density, while drag heating is not. This means that in high density targets, $>$ 100 g/cc, Ohmic heating is found to have a negligible impact on the heating and, as such, only drag heating is considered [4, 140].

3.4.3 Resistive Field Generation

As discussed in section 3.4.1, the neutralisation of the fast electron current is not exact and therefore leads to the generation of EM fields and are found to be dominant mechanism in prohibiting the transport of the fast electrons [124].

The resistive electric field generation can be considered from the simple form of Ohms law, equation 3.69, and Ampere's law [4, 77, 100, 119, 135, 139, 141]

$$\mathbf{E} = -\eta \mathbf{j_f} + \frac{\eta}{\mu_0} \nabla \times \mathbf{B}. \tag{3.90}$$

Other terms of Ohms law have been neglected due to these being insignificant in the fast electron transport scenario [139]. The second term shows the separation of the fast electron and background currents and is often found to make an inconsequential difference [136].

Inserting this into Faraday's law produces the magnetic field generated [4, 119, 141]

$$\frac{\partial \mathbf{B}}{\partial t} = \eta \nabla \times \mathbf{j}_f + \nabla(\eta) \times \mathbf{j}_f + \frac{\eta}{\mu_0} \nabla^2 \mathbf{B} - \frac{1}{\mu_0} \nabla \eta \times (\nabla \times \mathbf{B}). \tag{3.91}$$

The last two terms represent resistive diffusion and resistive advecition of the magnetic field [4] which are often neglected due to their long time scales [3, 136, 137]. Due to this, it is often common to write equation 3.91 as [3–5, 16, 17, 27, 28, 34, 48, 77, 96, 100–106, 119, 130, 137, 139, 142–144]

$$\frac{\partial \mathbf{B}}{\partial t} = \underbrace{\eta \nabla \times \mathbf{j}_f}_{\text{(a)}} + \underbrace{\nabla(\eta) \times \mathbf{j}_f}_{\text{(b)}}. \tag{3.92}$$

The role of the terms (a) & (b) can be considered as follows. Consider a cylindrically symmetric fast electron current $\mathbf{j_f}(r)$, which for term (a), produces a magnetic field of the form

$$\mathbf{B} = A \cdot \eta \cdot \nabla \times \mathbf{j}_f. \tag{3.93}$$

Taking the cross product of $\mathbf{j}_f$ and B produces

$$\mathbf{j}_f \times \mathbf{B} = A \cdot \eta \mathbf{j}_f \frac{d\mathbf{j}_f}{dr}, \tag{3.94}$$

thus term (a) acts to move the fast electrons regions of higher current density, self-collimation [4, 106, 137, 141].

For term (b), the magnetic field generated is of the form

$$\mathbf{B} = A \cdot \nabla(\eta) \times \mathbf{j}_f. \tag{3.95}$$

Taking the cross product of $\mathbf{j}_f$ and B produces

$$\mathbf{j}_f \times \mathbf{B} = A \cdot \mathbf{j}_f \frac{d\eta}{dr}, \tag{3.96}$$

thus term (b) acts to move the fast electrons towards regions of higher resistivity, and depending on the target, can either result in resistive collimation or beam hollowing [4, 98, 102, 103, 106].

These two terms depicted in figure 3.3 for a uniform target and are discussed in more detail in the following sections.

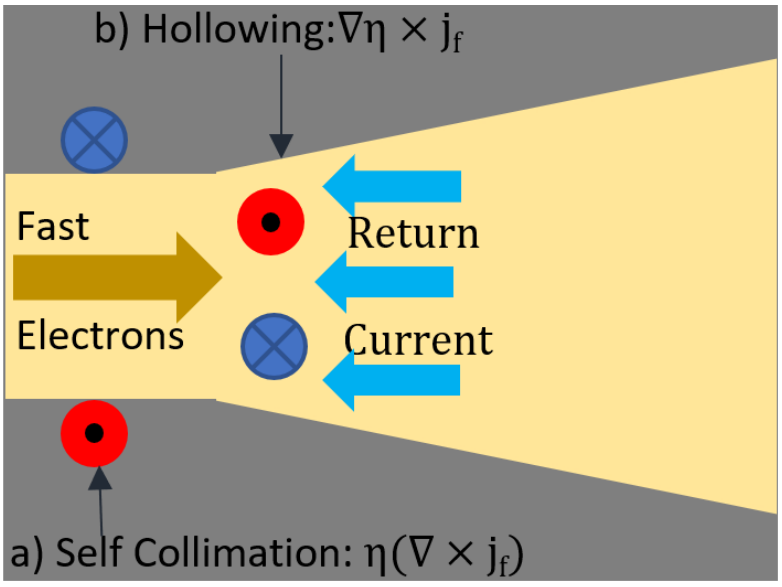

FIGURE 3.3: Cartoon showing magnetic field terms from equation 3.92 in a homogeneous target. (a) acts to reduce the fast electron beam radius therefore resulting in both a higher on axis current density and stronger heating. This results in the resistivity decreasing, leading to (b) hollowing the fast electron beam.

3.4.3.1 Self-Collimation

The magnetic field generated by term (a), $\eta\nabla\times\mathbf{j}_f$, acts to push the fast electrons towards regions of higher current density, leading to the fast electron beam self-collimating [4, 5, 106, 137, 141]. Bell & Kingham (2003) [137] presented a condition for self-collimation, $\Gamma > 1$

$$\Gamma = 0.13 n_{23}^{\frac{3}{5}} Z^{\frac{2}{5}} \ln\Lambda^{\frac{2}{5}} P_{TW}^{-\frac{1}{5}} T_{511}^{-\frac{3}{10}} (2+T_{511})^{-\frac{1}{2}} \times R_{\mu m}^{\frac{2}{5}} t_{psec}^{\frac{2}{5}} \theta_{rad}^{-2}, \tag{3.97}$$

where n_{23} is the background electron density in units of 10^{23} cm^{-3}, T_{511} is the fast electron temperature in terms of the electron rest mass, $R_{\mu m}$ is the beam radius in micrometers, t_{psec} the fast electron pulse duration in ps and θ_{rad} is the half angle in radians [4, 137].

The dependencies in equation 3.97 are weak due to the resistivity having an inverse dependence on temperature. This leads to stronger self collimation occurring in weaker fast electron beam power due to poorer heating.

3.4.3.2 Resistive Collimation

The magnetic field generated by term (b), $\nabla(\eta) \times \mathbf{j_f}$, acts to push fast electrons towards regions of higher resistivity. This therefore means that, depending upon the target, the magnetic field will either hollow out or collimate the fast electrons. In a uniform target, i.e. plastic, the fast electron beam will heat the center of the axis of propagation resulting in lower resistivity along this axis which leads to term (b) ejecting the fast electrons from this axis leading to hollowing of the beam. If, however, a target has a guiding structure where the resistivity is higher than the surrounding target and the fast electrons are beamed into this guiding structure, the magnetic field generated from this will instead confine these fast electrons inside this higher resistivity material - resistive collimation [4, 5, 98, 102, 103, 106].

Robinson et al (2007) [77] present the criteria for this guiding structure to confine fast electrons. The Larmor radius of an electron in a uniform magnetic field, with amplitude B_0, is

$$r_L = \frac{\gamma_e m_e c}{e B_0}, \tag{3.98}$$

and the resulting height of this circular segment is

$$h = r_L \left(1 - \cos\theta_{fe}\right) \tag{3.99}$$

where θ_{fe} is the half angle of the fast electrons.

Figure 3.4 shows a schematic of this height, (a), and scenarios where the fast electron is confined (b) and where it is not (c).

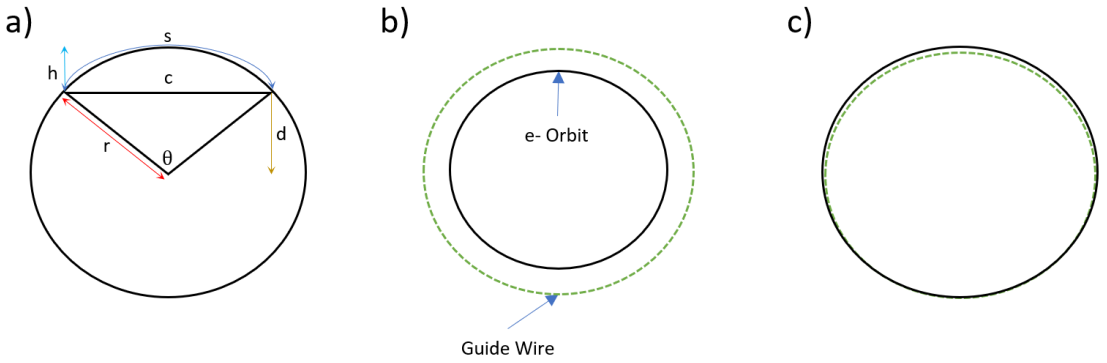

FIGURE 3.4: Figure showing the relevant diagrams for fast electron confinement in a guide wire. a) shows the construction of the circular segment, with r being the radius, h being the height of the circular segment, d the height of the triangle, θ the angle, c the chord length and s the secant length. b) shows the case where the fast electron is confined within the guide wire while c) shows the case where the fast electron is not confined

Thus for a magnetic field of extent L to confine the fast electron, the following must be true

$$B_\phi L_\phi > \frac{\gamma_e m_e c}{e} \left(1 - \cos\theta_{fe}\right). \tag{3.100}$$

Values of $B_\phi L_\phi \sim 10^{-3}\mathrm{Tm}^{-1}$ will confine the majority of fast electrons.

As well as presenting this criterion, Robinson et al (2007) explored this guiding structure by considering the cases where a) the guide wire has a larger resistivity than the substrate and b) the guide wire has a lower resistivity than the substrate. Results showed that the higher resistivity guiding structure confined the fast electrons within the target while the lower resistivity guiding structure expelled the fast electrons. The authors also noted that both magnetic field effects occur, with the resistive collimation dominating initially and then the self-collimation term takes over.

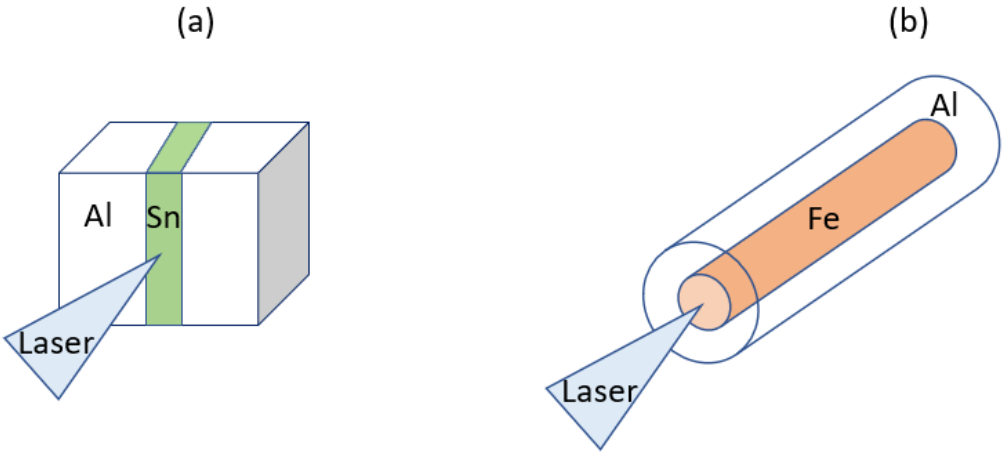

FIGURE 3.5: Diagrams showing two experimental methods in resistive collimation (a) Kar et al (2009) [105] and (b) Ramakrishma et al (2010) [101].

The effect of resistive collimation has been proved experimentally by various designs: Kar et al (2009) [105] presents an Al-Sn-Al slab, figure 3.5 (a), while Ramakrishna et al (2010) [101] presents a cylindrical Al target with an Fe guiding wire place in the center, figure 3.5 (b). These figures also show that only a perpendicular resistivity gradient is required for resistive collimation. However, designs similar to figure 3.5 (b) are found to be one of the more popular designs in the literature [4, 98, 102, 103], with the substrate usually consisting of a plastic, C_nH_n, and the guiding structure being composed of a metal.

The confinement of fast electrons in this guiding structure will lead to the rapid heating via the return current. Robinson et al (2013) [98] investigated the optimum heating conditions of this guiding structure by consider a variety of laser and target parameters. The authors noted that decreasing the laser wavelength leads to an improved wire heating by a factor of ~ 3. Improved confinement, and thus heating, is also found with lower intensity and longer pulse durations. A variety of Z values were also tried, with a higher Z wire resulting in superior heating in the Spitzer regime. However it was noted that the low temperature effects may well limit any benefits these higher Z targets offer. Improved heating is also found when the laser radius, r_{laser} & wire radius, r_{wire}, are of comparable size. The results also showed that the fast electron divergence angle, θ_{fe}, has a large impact in the heating of the target. This is of particular interest as, unlike

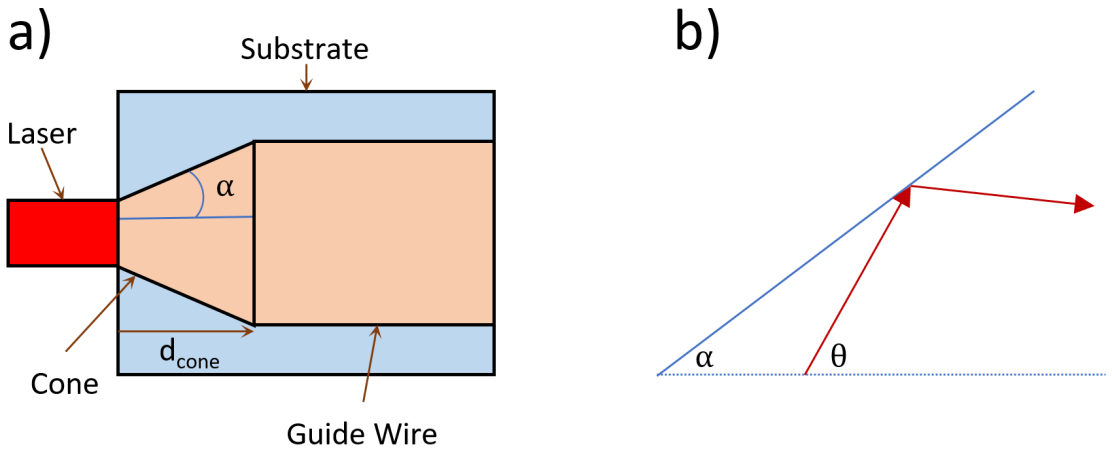

FIGURE 3.6: Figure showing the inverse conical taper scheme. a) A simple depiction of the inverse conical taper, based on Robinson et al (2015) [111], showing the half angle of the cone and its length. b) Schematic of a collision in the inverse conical taper, with the red line representing a fast electron with angle θ.

the other variables considered, this parameter is not tunable and various schemes have been presented to tackle this.

One scheme for the reduction of θ_{fe} is the "inverse conical taper" presented by Robinson et al (2015) [97, 111]. A cartoon and geometrical representation are found in figure 3.6 (a) and (b) respectively. If a fast electron is travelling at angle θ to the target axis and it strikes an oblique wall which itself is at angle α to the target axis, the change in angle can be written as

$$\tan\theta^{'} = \frac{\tan 2\alpha - \tan\theta}{1 + \tan 2\alpha \tan\theta} \tag{3.101}$$

this can therefore be rewritten as

$$\theta^{'} = 2\alpha - \theta. \tag{3.102}$$

Thus if $\theta > 2\alpha$, the fast electron propagation angle is reduced by 2α. The number of fast electrons which will undergo at least one collision can be written as

$$C_1 = \frac{\int_{\alpha}^{\frac{\pi}{2}} g\left(\theta\right) \sin\theta d\theta}{\int_{0}^{\frac{\pi}{2}} g\left(\theta\right) \sin\theta d\theta} \tag{3.103}$$

where g(θ) is the angular distribution of the fast electrons.

For the inverse conical design to be at its most effective, a low α is required. The half-angle of inverse conical taper can be written as

$$\tan(\alpha) = \frac{r_{cone}}{d_{cone}}. \tag{3.104}$$

The reduction of θ_{fe} via this method does come with some caveats. The inverse conical taper will expand in radius until a certain point which therefore means that the fast electron beam will expand radially in nature therefore resulting in $r_{wire} > r_{laser}$. Furthermore longitudinal dispersion of the fast electron beam is not completely negated leading to poor heating profiles in the targets. This is considered in more detail in Chapter 6, with various inverse conical taper designs investigated to find periods of uniform heating.

Another key factor in the heating of the guiding structure is the propagation of the fast electrons. Inhomogeneous propagation of fast electrons in the guiding structure will lead to the generation of interior magnetic fields [98, 102, 103, 130]. These magnetic fields lead to the filamentation of the fast electron beam, discussed in section 3.4.4, therefore resulting in annular transport and greater heating at the edge of the wire instead of the center [102].

Due to the laser pointing stability, there is a possibility that the laser pulse will be focused on the side of guiding structure instead of the center. This will lead to fast electrons being coupled into the substrate instead of the guiding structure. While one may consider expanding r_{wire} this will lead to poorer heating profiles, as mentioned previously, Robinson et al (2013) [98], while also increasing the likelihood of instabilities forming in the guiding structure. Alraddadi et al (2016) [102] proposed two alternatives to this step-guide: i) a co-axial guide which has an Al core surrounded by carbon and ii) a cladded target which has an Al wire surrounded by carbon which is graded down until the substrate Z. In both of these approaches r_{guide}, the non-substrate material, is larger than the r_{laser} but r_{core}, the aluminium core in the center of guide, is smaller than r_{laser}. This is done to prevent filamentation in the target. These targets were then set at $r_{guide} = 5\mu$m and compared against the conventional design, which had radii of 2.5 & 5 μm respectively while the laser was assumed to be 3.5 μm throughout. It was noted that the growth of

internal magnetic fields is only present in the larger step-target, $r_{step-target} = 5\mu m$, therefore meaning that these alternative designs look to suppress the growth of the magnetic field within the target. It was also found that $B_\phi L_\phi$ is larger for the cladded target while being smaller in the co-axial approach. The cladded target is found to produce values similar to $r_{step-target} = 2.5\ \mu m$ even though it has twice the radius. While the co-axial cable provides the lowest $B_\phi L_\phi$, it is found that the heating at depth is better than $r_{step-target} = 5\mu m$ due to the inhibition of the internal magnetic fields. Thus the grading of the guiding structure reduces the internal magnetic field thereby allowing for radius larger than r_{laser}. Alraddadi et al (2018) [103] continued this work by constructing a cladded target with an Al core, of varying width, which is graded down linearly to C and surrounded by a CH substrate. It was found that targets which had a smaller Al core, and thus more grading, produced stronger heating at depth while also stopping the growth of interior magnetic fields. This is due to more grading resulting in a larger L_ϕ. This large L_ϕ offsets the smaller B_ϕ, due to the grading, resulting in similar $B_\phi L_\phi$ for the targets.

An issue which arises from the use of the guide structure as a wire is that, instead of altering the transport properties of fast electron beam it will instead "bottle" them. This will result in fast electrons leaving with their initial divergence angle after the guiding structure. This, however, is not the case when considering the inverse conical taper, which was discussed above.

3.4.4 Instabilities

The counter-propagating nature of the two currents can lead to transport instabilities [5, 18, 29, 36, 133]. These instabilities can lead to the onset of filamentation which will in turn lead to enhanced energy loss, changes to angular divergence and non-uniform heating [4, 5, 102, 103]. In the following section, some of the instabilities which can be expected in fast electron transport will be briefly considered.

The Weibel instability is a transverse instability which occurs due to the magnetic repulsion between the counter-propagating currents. Any inhomogeneity in the fast electron density will lead to the generation of local magnetic fields which act to pinch part of the beam into a filament, thus breaking the beam up. This magnetic field acts on the electrons via the Lorentz force which leads to further

inhomogeneities in the beam and thus further growth of the Weibel instability. The growth rate of the instability can be written as [5, 133]

$$\Gamma_w = \omega_f \sqrt{\frac{n_f}{\gamma n_e}} \times \frac{v_f}{c}. \tag{3.105}$$

where ω_f is the plasma frequency of the fast electrons.

Another instability is the resistive instability [5, 131, 144]. As noted by Gremillet et al (2002) this is an extension of Weibel instability, with this occurring when the return current is collisional. The magnetic fields grow as the resistivity of plasma grows, with the typical time-scale of the magnetic field being written as [5, 131]

$$\tau_r = \frac{\mu_0 f_r^2}{\eta} \tag{3.106}$$

where f_r is the hot filament radius.

Gremillet et al (2002) [131] also noted that both the Weibel and Resistive instabilities growth is dependent upon the transverse temperature gradient. A large enough transverse temperature gradient will mean that the outward transverse forces are larger than the pinching force created by modulations in magnetic field and will suppress the instabilities.

Insulators are also found to be prone to the ionisation instability [5]. Due to insulators having no free-electrons, ionisation will need to occur so that a return current can be formed. If there are perturbations in the fast electron beam, non-uniform ionisation will occur and this can also lead to filamentation of the beam.

Experimental work done by McKenna et al (2011) [14] showed that the lattice structure of a material, carbon in this case, has a large role in the growth of instabilities. The authors considered a highly ordered lattice structure, such as diamond, and a disordered lattice structure, such as viterous carbon, and diagnosed the transport patterns via the protons accelerated via the TNSA mechanism. Viterous carbon was found to produce heavy filamentation resulting in a highly structured proton beam. Conversely, Diamond was found to suppress filamentation resulting in a more uniform proton beam which was comparable to

Aluminium. The structured nature of diamond results in metal like resistivities at 1 - 100 eV & thus the quenching of instabilities in the beam.

Blackman et al (2015) [128] investigated the link between the filamentation instability and low temperature resistivity in two disordered materials: Aluminium & Copper. Results showed that Copper experiences less filamentation compared to the Aluminium target, with the Copper target experiencing no filamentation at all when $I\lambda_L^2 < 5{\times}10^{19}$ Wcm^{-2} μm^2. This can be explained by considering the peak low temperature resistivity (PLTR) of the two targets. Copper, which has a lower PLTR, generates a larger collimating field which suppresses the filaments while in Aluminium, which has a higher PLTR, fine structures grow in the magnetic field, resulting in filamentation of the fast electron beam. The difference in the evolution of these magnetic fields can be describe due to the differences in heating. The lower PLTR in Copper means that it will experience weaker heating, equation 3.89, and thus takes longer to transition to the Spitzer resistivity. This allows for larger collimation fields to be generated. On the other hand, Aluminium will instead reach the Spitzer resistivity faster, resulting in weaker collimating fields.

3.5 Numerical Modelling of Fast Electron Transport: ZEPHYROS

Numerical modelling in physics offers a plethora of uses, ranging from the confirmation of experimental results to testing theoretical concepts. As well as this, the numerical approach allows for certain physics to be "turned off" e.g. magnetic field generation, constant resistivity, or other processes, leading to a close interrogation of a complex model.

Throughout the work presented in Chapters 4 & 6, the 3D Cartesian PIC-Hybrid code ZEPHYROS [105] developed by Dr A. P. L. Robinson, based upon work by Davies [104, 136, 141], is used. PIC-Hybrid is the approach where the fast electrons & background plasma are described via a kinetic and fluid approach respectively. This different treatment is required due to the fact that the physical nature of the two currents, section 3.4, is very different and results in dissimilar scale lengths & time scales which lends itself well to a "split" approach for the problem [4].

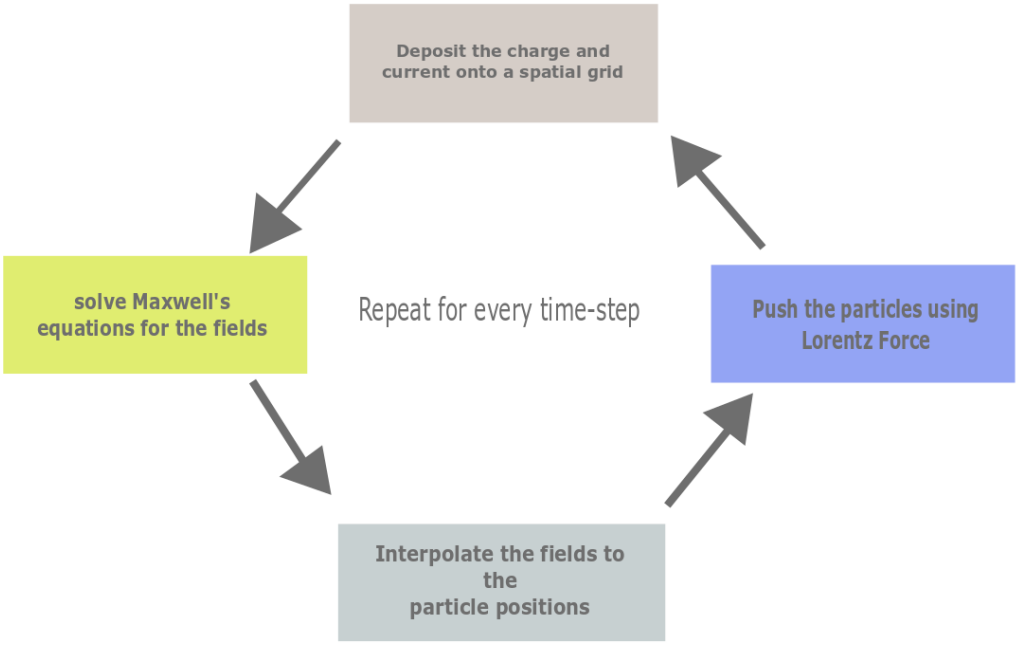

FIGURE 3.7: Illustration of the PIC algorithm. Adapted from Gibbon [13, 146].

By kinetic approach it is meant that the fast electrons are represented via the particle in cell (PIC) technique. Here particles are described via a single distribution $f = f(\mathbf{v}, \mathbf{x}, t)$ whose evolution is described by [4, 5, 13, 42, 66, 145]:

$$\frac{\partial f_s}{\partial t} + \mathbf{v_s} \cdot \frac{\partial f_s}{\partial \mathbf{r}} - \frac{\mathbf{F_s}}{m_s} \cdot \frac{\partial f_s}{\partial \mathbf{v}} = \begin{cases} 0, & \text{Collisonless(Vlasov Equation)} \\ \left(\frac{\partial f_s}{\partial t}\right)_c, & \text{Collisional(Vlasov-Fokker-Planck Equation)} \end{cases} \tag{3.107}$$

where s is the species of particle, x & $\mathbf{v}$ are the phase space position and velocity co-ordinates respectively, f is the distribution function, m the mass and $\mathbf{F}$ is the Lorentz force, equation 2.12.

Equation 3.107 represents the two methods for kinetic modelling of a plasma: when the rhs is 0, the plasma is collisionless, while when the rhs is $\left(\frac{\partial f}{\partial t}\right)_c$ the equation describes a collisional plasma. As it can be imagined, the general solution of either equations is intractable for most problems [13].

To circumvent this issue, the PIC technique is often used [4, 5, 13, 94, 146]. In this approach, computational particles are used to represent a certain number of real particles, or to consider it another way, to represent a certain part of the distribution function. The use of these computational particles follows from the Lorentz force, equation 2.12, and noting that only the charge to mass ratio varies for different particles. Thus, as long as these computational particles have the same charge-mass ratio as the constituent particles of a plasma, it can be simulated. As it can be imagined, having more computational particles will allow for a better representation of the distribution function and therefore produce more accurate results. For most simulations, values of $1{\times}10^7$ computational particles and above is commonly used and can therefore still be computationally expensive.

The core PIC technique solves for a fully ionised collisionless plasma [5, 146], the Vlasov equation, by making using of the algorithm presented in figure 3.7. Particles are first accelerated by the Lorentz equation [13]

$$\frac{d}{dt}\left(\gamma_i v_i\right) = \frac{q_i}{m_i}\left(\mathbf{E} + \frac{\mathbf{v}_i}{c} \times \mathbf{B}\right). \tag{3.108}$$

Particle positions and velocities are then mapped onto a computational grid which allows for the calculation of current densities. These current densities can then be used to calculate new EM fields which, in-turn, are used to accelerate the particles again. These steps are then repeated until the end of the simulation.

Due to the core PIC method being collisionless in nature [5, 94, 146], techniques are required to incorporate $\left(\frac{\partial f}{\partial t}\right)_c$ and thus solve the Vlasov-Fokker Planck equation. Collisions are included via a Monte-Carlo approach, which scatters particles in momentum space [5, 94]. A popular algorithm for collisions is to pair particles and perform Rutherford scattering[5, 94]. Ionisation can also be included, which uses a Monte-Carlo approach in conjunction with ionisation cross-sections[5, 94].

During the simulation, the PIC code requires to resolve λ_D and ω_{pe} at every time step. If these values are not resolved, it can lead to a variety of non-physical phenomenon including self-heating [5]. This self heating will occur until λ_D has been resolved.

The PIC technique is in stark contrast to the fluid approach which is used in

the description of the background plasma. Here, the plasma is assumed to be highly collisional & only macroscopic variables, such as fluid velocity ($\mathbf{v}$), pressure of the fluid (P) and mass density (ρ) are considered. The highly collisional nature of this plasma therefore allows for it to be approximately described via a Maxwellian distribution and it is assumed that this state is in Local Thermal Equilibrium. Fluid codes require a resistivity curve & equation of state to complete the description [5]. In ZEPHYROS, it is assumed that the background is represented via a static fluid which is heated by both the Ohmic & drag heating. Its SHC is described by a fit to the TF-corrected model originally presented in unpublished work by Bell (1980) [105, 117, 141]. The TF model, section 3.2, is also used to describe the ionisation state of the background fluid. For the resistivity curve, ZEPHYROS can either use the inbuilt Lee-More resistivity, section 3.3.2.1, an inbuilt Spitzer curve or can use a user defined resistivity curve.

To allow for the use of these two separate approaches to describe fast electron transport, the hybrid approximation, a number of assumptions are made which are presented below.

The fast electron density is assumed to be far smaller than the background density, $n_f << n_b$. This assumption, however, does not mean that the current density of the fast electron beam will be negligible. Furthermore the background plasma is assumed to be static and will instantaneously respond to the fast electron beam and will also be heated by both Ohmic heating and collisional drag, section 3.4.2. In conjunction with this, it is also assumed that the fluid description used to describe the background plasma is valid in both temporal and spatial scales of interest, even if the fast electrons are absent.

The small nature of fast electron density therefore allows for current neutrality, section 3.4.1, to hold and is represented by equation 3.84,

$$\nabla \times \mathbf{B} \approx \mu_0 \left(\mathbf{j}_f + \mathbf{j}_b \right), \tag{3.109}$$

where displacement current has been neglected.

The electric field is assumed to be described via Ohm's law. This derivation is the same as section 3.4.3, and is written as

$$\mathbf{E} = -\eta \mathbf{j}_f = \eta \mathbf{j}_b \tag{3.110}$$

which, from Faraday's law, produces a magnetic field of

$$\frac{\partial \mathbf{B}}{\partial t} = \nabla \times (\eta \mathbf{j}_f)\,. \tag{3.111}$$

The use of these fields therefore means that the standard PIC cycle is not followed. The fast electron current density, $\mathbf{j}_f$, is calculated from the interpolation of the particles on the grid. $\mathbf{j}_f$ is then used to update the fields via equations 3.110 & 3.111. These updated fields are then interpolated onto the particles and the cycle is repeated.

As well as the above assumptions, it is also noted that the generation of fast electrons is not modelled in ZEPHYROS. Instead, a prescribed distribution function is used to initialise the fast electrons. To specify between fast electrons and the fluid background, an energy cut-off of 10 keV is used, with energies larger than this being treated kinetically, while values lower are described via the fluid background. Furthermore, the laser pulse is not modelled on ZEPHYROS but is instead introduced as an energy dump of fast electrons into specified cells. This energy dump can be determined on the basis of characteristic laser parameters: pulse shape, λ_L, β, I_L etc. As an example, the user would set $\mathrm{I}_L = 5{\times}10^{19}$ Wcm^{-2} and a $\beta = 0.3$, resulting in $1.5{\times}10^{19}$ Wcm^{-2} being coupled to the cells. The number of fast electrons injected into the cells at x=0 is given as

$$N_{fast} = \frac{\beta I(r) \triangle y \triangle z \ \mathrm{d}t}{\epsilon_f} \tag{3.112}$$

where β is the fast electron conversion efficiency, section 2.7.2, dt the time step, $\triangle y \triangle z$ is the grid spacing for y & z respectively & ϵ_f is the pondermotive scaling, equation 2.64.

Due to the above assumptions, a static background which responds instantaneously to fast electrons and that $\mathbf{v}_f \sim$ c, ZEPHYROS only considers the fast electrons collisions for drag

$$dp = -\frac{D}{2mv^2}\ln\Lambda_l dt, \tag{3.113}$$

and random scattering of the fast electrons

$$d\theta = \frac{1}{p}\sqrt{\frac{ZD}{v}\ln\Lambda_s}\Gamma(t)\mathrm{dt}^{\frac{1}{2}}. \tag{3.114}$$

Here, p is the momentum, dt is the time step, $\Gamma(t)$ is time varying random number, $\mathrm{D} = \frac{n_b e^4}{2\pi\epsilon_0^2}$ and the two logarithmic terms are dependent on the target.

3.6 Fast Electron Heating Experiments

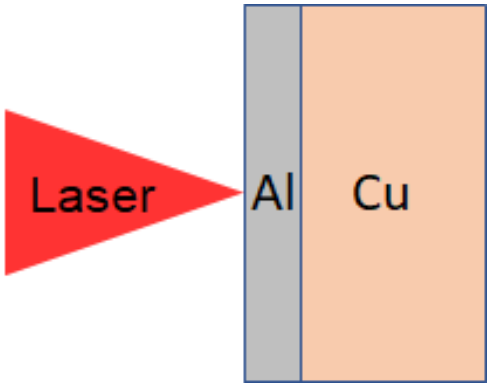

(A) Target for diagnosing pre-plasma.

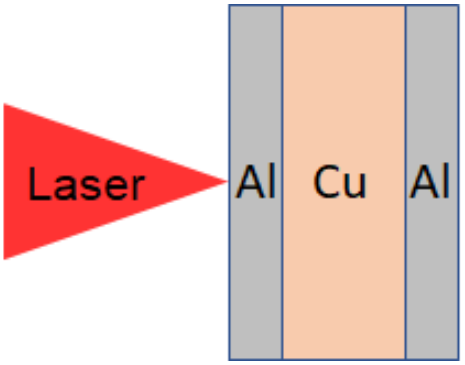

(B) Sandwich target [83].

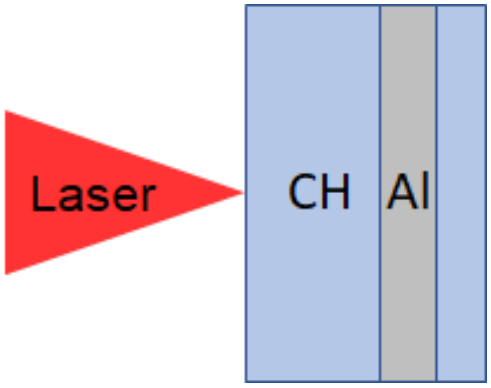

(C) Buried layer target [147].

FIGURE 3.8: Various targets used in experimental setting

Fast electron heating experiments offer considerable insight into the various transport properties of the fast electron beam, ranging from the role of instabilities to energy deposition within the target. Unlike the numerical approach, section 3.5,

an experiment will need to deal with a variety of physical effects in the laboratory setting. Due to the majority of the relevant physics occurring within the target, optimisation of its design is crucial. Some of the most typical, necessary considerations in planning a fast electron transport experiment will be discussed below.

Due to most CPA laser systems being coupled with a pre-pulse (section 2.2) there will often be a pre-plasma (section 2.5.2) which will affect the laser interaction, as well as the generation and transport of fast electrons [36, 49, 53, 54, 71, 148, 149]. For example, as it was previously discussed in section 2.7.2, Gray et al (2014) [53] showed that the pre-plasma can either result in a focusing or defocusing of the laser pulse therefore resulting in either a more energetic or less energetic fast electron beam respectively. Moreover experimental and numerical work by Scott et al (2012) [49] has shown that the pre-plasma scale length impacts the kinetic energy, current & number of fast electrons. Thus these characteristics will greatly alter the properties of the beam and a full characterisation of the pre-plasma is required to quantify the role of it.

There are a variety of methods in which this can be achieved. One is the use of pockel cells in the laser chain [44, 49] which results in controllable variations in the pre-pulse and the resulting comparisons allow for the characterisation. Another method, which is popular throughout the literature, is to use a structured target as shown in figure 3.8a (a). The different material on the front, a thin foil of a few μm, will result in a different spectra of Kα emission from the pre-plasma & target bulk allowing for a characterisation of the pre-plasma and its impact on the fast electron generation [28, 36, 60]. Another approach to counteract the pre-pulse is to frequency double the laser pulse. This results in the suppression of the pre-pulse [34, 59] and allows for comparison between the frequency doubled and fundamental frequency shots [32] allowing to elucidate the role of the pre-plasma.

The use of a structured target also extends to diagnosing the propagation of fast electrons in the target. Consider the target shown in figure 3.8a. The propagation of fast electron beam through the target will be difficult to diagnose due to there being no way to distinguish at which depth the Cu-Kα emission is generated from. Due to this, layered targets are often utilised in the literature. These layered targets can either be "sandwich" targets [83], as shown in figure 3.8b, or buried layer targets [34, 37, 50, 59, 139, 147], as shown in figure 3.8c. These targets

types vary in thickness, with this being dependent upon the experimental goals. Thus these target designs will result in the generation of different Kα spectra at different depths into the target during the propagation of the fast electron beam through the target and thus a better consideration of the transport properties of the fast electron beam, e.g. in terms of heating at depth or the onset of transport instabilities.

Other target considerations are important if certain physical effects need to be reduced. For example if the target length is smaller than the fast electrons mean free path, these fast electrons will generate a large electric field at the rear of the target, which leads to TNSA as discussed in section 1.2.1. This electric field will also deflect the less energetic electrons, redirecting them back into the target and resulting in further heating of the target. This effect, known as refluxing, will also contribute to the Kα emission from a buried layer and will complicate the inspection of the Kα for evaluating the fast electron transport. To counteract this, the thickness of the target can be increased to reduce the effect of refluxing [16, 53]. Further target alterations also look at using reduced mass targets [28, 36]. These targets allow for higher temperatures due to an equal amount of energy deposition occurring in a smaller volume [28]. Other approaches use structured targets to investigate resistive collimation, figure 3.5 [101, 105, 144], as discussed in section 3.4.3.2.

The choice of diagnostic is crucial for the correct characterisation of the fast electron beam. As it was originally discussed in section 2.7.2 there are a variety of methods used in the diagnosing of fast electron transport. In almost all experiments, Kα diagnostics are considered in imaging and/or spectroscopy arrangements. In the imager approach [28, 50, 84] Kα x-rays are collected and then focused, usually by a bent Bragg crystal, onto a spatially resolved detector, i.e. CCD camera or x-ray film. This produces 2D images which allow for the spatial characterisation of the fast electron beam transport. In the Spectroscopy approach [28, 32, 33, 35, 37, 49, 50, 57, 59, 83, 88, 90], x-rays are dispersed according to their wavelength by a crystal, and the spectrum is recorded on a suitable detector. Observation of characteristic lines in the spectrum (Kα, Kβ etc), and will assist the determination of some of the properties of the fast electron beam such as the number of electrons in the target, divergence of the beam etc. Techniques can also be used to image the optical emission from fast electrons leaving the target,

via Optical Transition Radiation (OTR) or Coherent Transition Radiation (CTR) [28, 79, 105]. Due to the transition between two different refractive indexes when the fast electrons leave the rear of the target, radiation will be emitted [28] and is imaged onto a CCD camera. This may allow for direct measurement of the fast electron distributions, energies & divergence angles.

In heating experiments, the measurement of temperature is usually considered by measurements of target heating at a given depth [26, 28, 32–37, 57, 59, 83–85, 90, 90, 150, 151] into the targets. Chen et al (2007) [36], showed that for $I_L\lambda_L \sim 10^{19}$ Wcm^{-2}, a heating layer of Ti 0.2 μm placed 1 μm after Al, was heated to $\sim$ 1300 eV while only reaching $\sim$ 500 eV for CH targets. Evans et al (2005) [35] showed that temperatures in excess of 500 eV at 10 - 20μm depth are reached for $I_L > 10^{20}$ Wcm^{-2}. Martinolli et al(2002) [83] showed that temperatures of 40 eV at distances of 40 μm for Al-Cu-Al targets with $I_L\lambda_L \sim 10^{19}$ Wcm^{-2}. Further work by Martionlli et al (2006) [84] expanded these measurements show that for comparable intensities, few tens of eV were reached at up to 100 μm in depth.

3.7 Summary

This Chapter provides an introduction to a variety of topics in fast electron transport. First, material properties were discussed which included the Thomas-Fermi model, which is used to describe the SHC of target, to the various resistivity models used: Spitzer, Lee-More & Robinson. Following this, physics relevant to fast electron were discussed, with the current balance approximation, Ohmic and drag heating, resistive magnetic field generation and instabilities all discussed. The Chapter was rounded out by considering numerical methods used in this thesis, ZEPHYROS, and the current state of fast electron heating experiments.

Chapter 4

Fast Electron scalings for Ohmic heating

4.1 Overview

In the following Chapter, simple analytical scalings for Ohmic heating coupled with numerical simulations are used to show that the use of a Spitzer-like resistivity is inadequate to describe both the full evolution of the target and also underestimates influence of laser target parameters, I_L, λ_L & n_i. It is instead shown that not only are these dependencies better described via a low temperature resistivity but also that the low temperature phase of the target evolution has a very significant role in the later stage evolution of the temperature of the target.

4.2 Fast Electron Scaling

A simple but useful tool in fast electron heating are analytical scalings. These allow for rough calculations on experimental parameters prior to investing time in detailed simulations. Moreover, these scalings allow the core physics of the problem to be reduced into a highly approximate calculation and by comparing these predicted scalings the with actual results, one can see how well the problem is understood. To derive these scalings, we first recall from section 3.4.2 that the dominant heating mechanism in a solid target is Ohmic heating which, from equation 3.87 is

$$\frac{\partial T}{\partial t} = \frac{\eta \mathbf{j}_f^2}{C}. \tag{4.1}$$

By now considering an ideal monotonic gas heat capacity for C and taking η to be the reduced form of the Spitzer resistivity, equation 3.34, equation 4.1 becomes

$$\frac{\partial T}{\partial t} = \frac{2}{3n_e e} \frac{10^{-4} Z \ln\Lambda}{T^{\frac{3}{2}}} \mathbf{j}_f^2. \tag{4.2}$$

By then considering the rigid beam model, in which current density remains fixed, integrating equation 4.2 gives

$$T(t) = \left[B t_h + T_0^{\frac{5}{2}} \right]^{\frac{2}{5}}, \tag{4.3}$$

where B = $\frac{5Z\ln\Lambda \mathbf{j}_f^2}{3n_e e}$, t_h is the heating time and T_0 is the initial temperature.

In the strong heating limit, T>>T_0, equation 4.3 becomes

$$T(t) = (B t_h)^{\frac{2}{5}} = \left(\frac{5\ln\Lambda}{3e} \right)^{\frac{2}{5}} \frac{Z^{\frac{2}{5}} \mathbf{j}_f^{\frac{4}{5}} t_h^{\frac{2}{5}}}{n_e^{\frac{2}{5}}}, \tag{4.4}$$

One can relate the current density to laser parameters via energy conservation, equation 3.78,

$$\mathbf{j}_f = \frac{e\beta I_L}{\epsilon_f}, \tag{4.5}$$

where β is the conversion efficiency and ϵ_f the mean energy of the fast electron beam, section 2.7.2.

If the fast electron temperature follows a ponderomotive scaling, equation 2.64, one has $\epsilon_f = A\sqrt{I_L \lambda_L^2}$, with A a proportionality constant. This leads to [98]:

$$T \propto \frac{\beta^{\frac{4}{5}} I_L^{\frac{2}{5}} t_h^{\frac{2}{5}}}{\lambda^{\frac{4}{5}} n_i^{\frac{2}{5}}}, \tag{4.6}$$

which shows the impact of the relevant parameters associated with Ohmic heating from the fast electron beam for a Spitzer resistivity.

However as noted in section 3.3.2, the Spitzer resistivity only accurately describes the resistivity of a plasma state. As this will not be the case when the target is in either the solid or WDM phase, these scalings will be incorrect.

Due to the complex nature of low temperature resistivity models, section 3.3.2, it is often difficult to produce simple analytical scaling predictions like the ones above. Predictions can be made by considering a resistivity which scales with temperature to an arbitrary power [136]

$$\eta = \eta_0 \left(\frac{T}{T_0} \right)^{\alpha}, \tag{4.7}$$

where η_0 is a specified value of resistivity and α is an arbitrary constant.

Substituting this into equation 4.1 produces [136]

$$T = T_0 \left(1 + (1-\alpha) \frac{\eta_0 \mathbf{j}_f^2 \tau_L}{C T_0} \right)^{1/(1-\alpha)}, \alpha < 1. \tag{4.8}$$

By then considering $\alpha = 0$, i.e. a constant resistivity, the scalings can be rewritten as

$$T \propto \frac{\beta^2 I_L \tau_L}{Z n_i \lambda_L^2}. \tag{4.9}$$

Setting $\alpha = \frac{1}{2}$, i.e. a square-root resistivity, gives instead

$$T \propto \frac{\beta^4 I_L^2 \tau_L^2}{Z^2 n_i^2 \lambda_L^4}. \tag{4.10}$$

Both of these scalings are predicated upon strong heating, T>>T_0. In the square-root resistivity case, this assumption leads to:

$$T = (A + T_0^{\frac{1}{2}})^2 = A^2 + 2AT_0^{\frac{1}{2}} + T_0. \tag{4.11}$$

where

$$A = \frac{2\eta \mathbf{j}_f^2 \tau_L}{3 n_e e}. \tag{4.12}$$

Here it can be seen that these assumptions both predict far stronger scaling dependencies than the ones predicted by the Spitzer case, equation 4.6.

As well as this, all of the scalings derived above assume that both the ionisation state and the specific heat capacity are constant. This assumption is further analysed in Chapter 5. While this assumption is heuristic in nature, it allows us to understand the potential implications of this temperature regime.

To test these simple analytical scalings presented in equations 4.6, 4.9 & 4.10, numerical simulations are performed as discussed in the next sections.

4.3 Numerical Simulations

A variety of simulations were performed using ZEPHYROS, section 3.5, which varied the parameters I_L, λ_L & n_i across 4 targets: Al, Ti, Au & CH. For each of these four targets we run benchmark simulations which use the same parameter apart from the n_i & Z value. The test simulation consists of 200 × 200 × 200 grid, with each cell being 0.1 μm in size. 4×10^7 particles were used. The laser pulse had a Gaussian profile and we set r_{spot} as 10 μm, I_L as 2×10^{19} Wcm^{-2}, β as 0.3, t_h, the laser duration, as 5.6×10^{-13} s and λ_L as 1.053 μm. The fast electron beam had an exponential energy distribution, $\exp\left(-\frac{E}{T_F}\right)$, and a divergence angle of 60° (1.047rad) was selected from an experiment on fast electron propagation [152]. x boundaries were set to be reflective. The temperature of the beam was calculated from the pondermotive scaling, equation 2.64. The Lee-More resistivity model, section 3.3.2.1, was used to describe the resistivity. From Run A, the three parameters were then varied individually as shown in table 4.1 & 4.2.

Run	I (Wcm^{-2})	λ (μm)	n_i	Fast e- Temp (MeV)
A	2×10^{19}	1.053	See table 2	1.61
B	9.25×10^{19}			3.92
C	5.55×10^{19}			2.94
D	3.33×10^{19}			2.18
E	1.2×10^{19}			1.16
F	7.2×10^{18}			0.82
G	4.32×10^{18}			0.57
H	2×10^{19}	4.875		9.02
I		2.925		5.22
J		1.755		2.95
K		0.6318		0.824
L		0.379		0.388
M		0.227		0.166
N		1.053	See table 2	1.61
O			See table 2	
P			See table 2	
Q			See table 2	
R			See table 2	
S			See table 2	

TABLE 4.1: Parameters used in each run, with Run A representing the standard run.

Run	n_i (Al)	n_i (Ti)	n_i (Au)	n_i (CH)
A	6	5.71	5.9	0.829
N	27.8	26.4	27.3	3.4
O	16.7	15.9	16.4	2.3
P	10	9.52	9.83	1.38
Q	3.6	3.43	3.54	0.497
R	2.16	2.06	2.124	0.298
S	1.296	1.2744	1.2334	0.179

TABLE 4.2: Different ion densities used for the four targets given in units of $\times10^{28}$ m^{-3}.

Before going any further, it may strike the reader as strange that the Lee-More model has been used to describe the target resistivity while the scalings for this

have not been considered above. The reason for this, which was initial discussed in the previous section, can be seen by considering the form of the Lee-More resistivity as given by equation 3.48 or 3.53. In both of these equations, there is a degeneracy parameter which does not reduce down to simple scaling laws. However it is only reasonable to use a near realistic resistivity model in these full numerical simulations.

4.4 Results

4.4.1 Initial Results

To determine these scalings the temperature was taken in the center of a target, y = z = 10 μm, at depths x = 2, 4 & 6 μm. The temperatures reached at a 2 μm depth are plotted in figure 4.1. Power dependencies on $\propto I_L^{\alpha}\ \lambda^{\epsilon}\ n_i^{\rho}$ were then fitted to these temperatures. The plotting of these coefficients can be found in figure 4.2 & and in tabular form 4.3 - 4.5.

Run	I	λ	n_i
CH	0.89455	-1.14409	-0.47616
Al	1.17037	-1.39737	-0.94616
Ti	1.31882	-1.48537	-1.14573
Au	1.71775	-1.61837	-1.61676

TABLE 4.3: Exponents from power laws for heating at depth of 2 μm

Run	I	λ	n_i
CH	0.89452	-1.14852	-0.49701
Al	1.54547	-1.74238	-1.35978
Ti	1.71326	-1.74842	-1.48347
Au	1.71396	-1.31961	-1.61393

TABLE 4.4: Exponents from power laws heating at depth of 4 μm

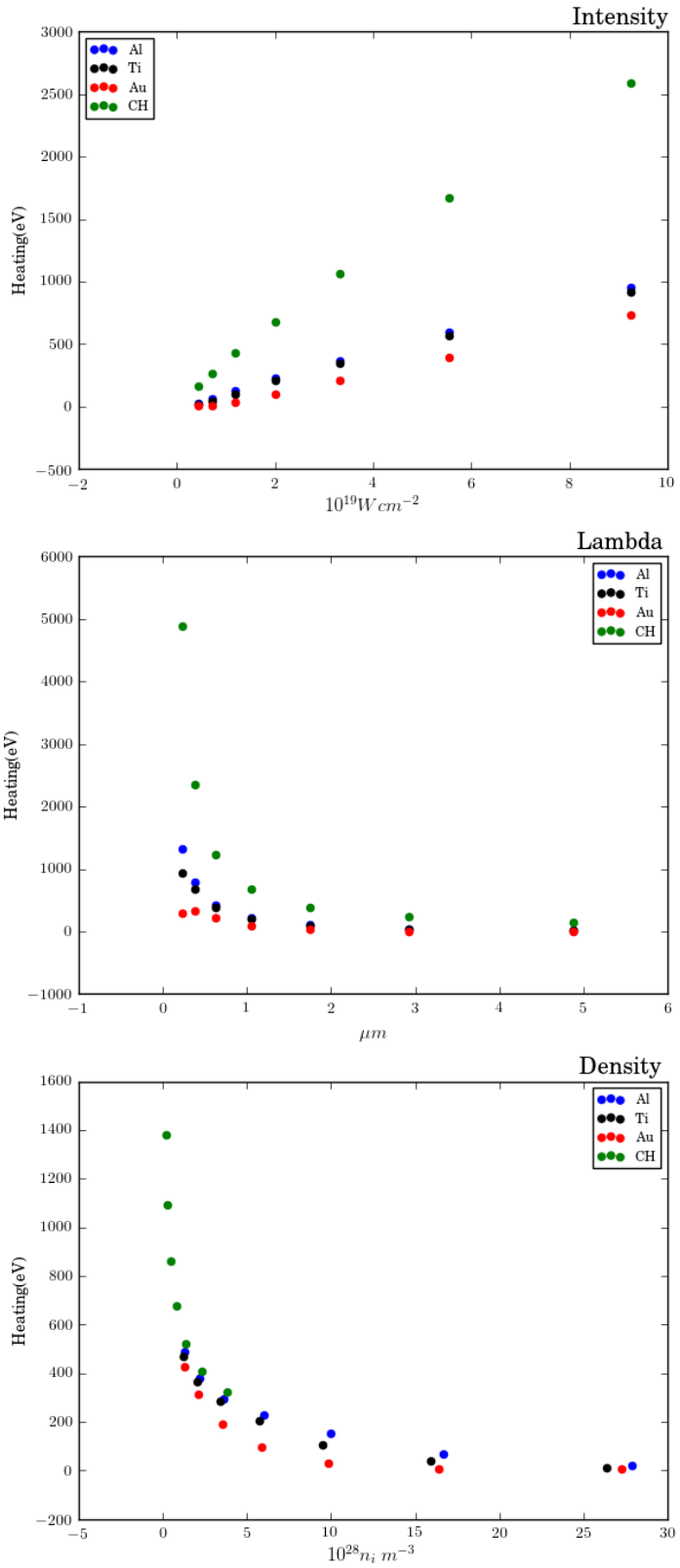

FIGURE 4.1: Maximum temperatures reached at a depth of 2 μm in the different models, plotted against the parameters I_L, λ_L & n_i.

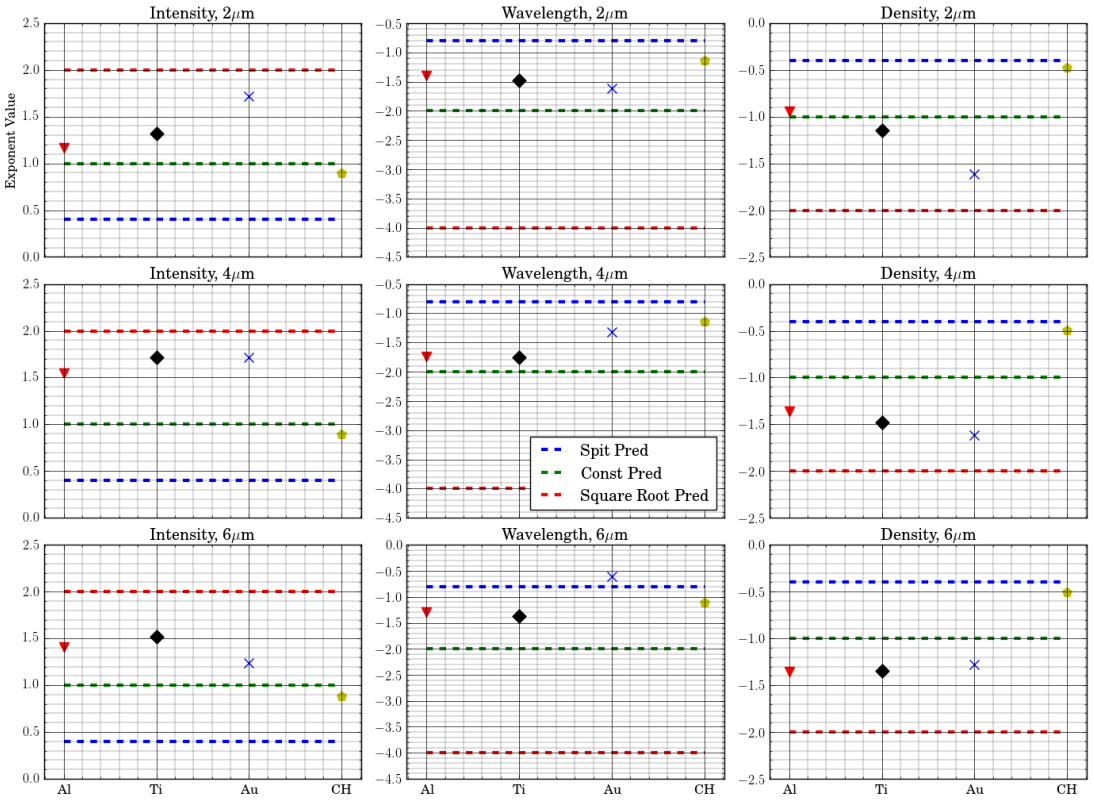

FIGURE 4.2: Figures showing the respective dependencies for I_L, λ_L & n_i in the four targets: Al, Ti, Au & CH. The blue line represents the predicted Spitzer scaling, equation 4.6, while the orange line is the constant resistivity scaling, equation 4.9, & the green line is the square root resistivity, equation 4.10.

Run	I	λ	n_i
CH	0.88295	-1.11727	-0.50418
Al	1.41015	-1.29582	-1.35218
Ti	1.52150	-1.36827	-1.34533
Au	1.23550	-0.60065	-1.28172

TABLE 4.5: Exponents from power laws heating at depth of 6 μm

As it can be seen from figures 4.1 & 4.2 and tables 4.3 - 4.5, the analytical Spitzer scalings severely underestimate the scaling of the 3 parameters. This is clearly evident in the figure 4.1 where, for CH, it can be seen that a linear fit, constant resistivity, produces a far better fit to the temperatures produced in the simulation compared to the Spitzer prediction. Another trend which appears in these exponents relates to the target Z. The behaviour for Al is better described via a constant resistivity, equation 4.9, while the dependencies for the higher Z targets, Ti & Au, are better represented via the square-root resistivity, equation 4.10. This

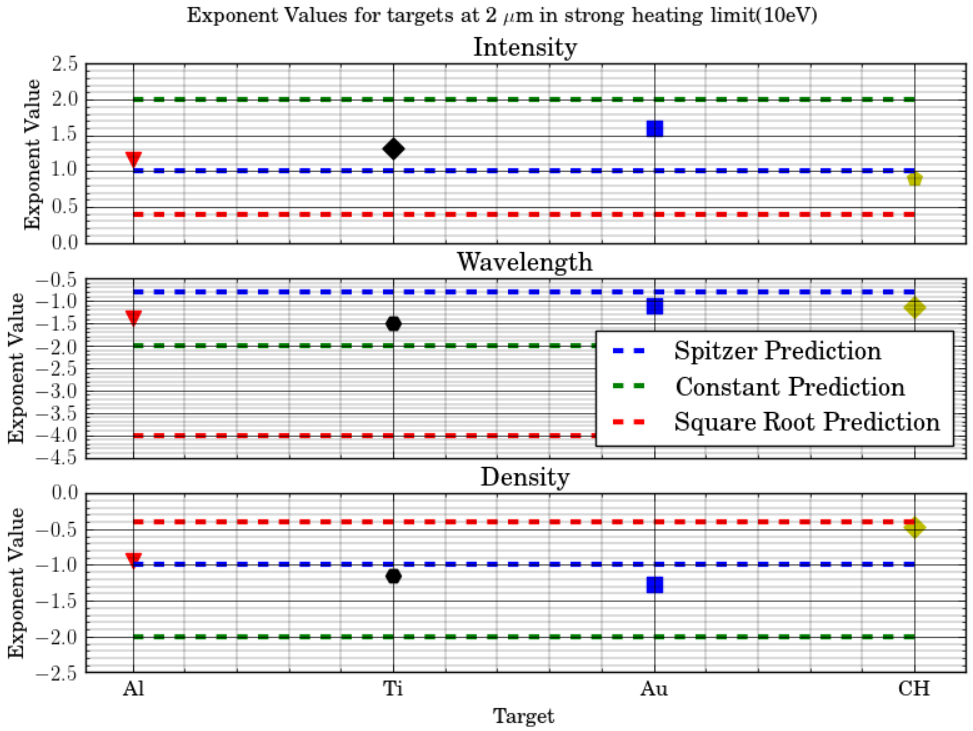

FIGURE 4.3: Figure showing dependencies for I_L, λ_L & n_i in the four targets: Al, Ti, Au & CH for T > 10 eV. The blue line represents the predicted Spitzer scaling, equation 4.6, while the orange line is the constant resistivity scaling, equation 4.9, & the green line is the square root resistivity, equation 4.10.

dependence on Z therefore means that the initial phase of the low temperature resistivity has a larger impact even for temperatures reaching T > 1 keV.

As it was stated in the derivation of the analytical scalings, a strong heating approximation has been assumed, equation 4.11. To test this assumption, the same fitting procedure was applied while removing temperatures < 10, 50 & 100 eV respectively. Table 4.6 & figures 4.3-4.5 present these results. Due to all values of CH being heated to beyond 100 eV, these exponents were left out.

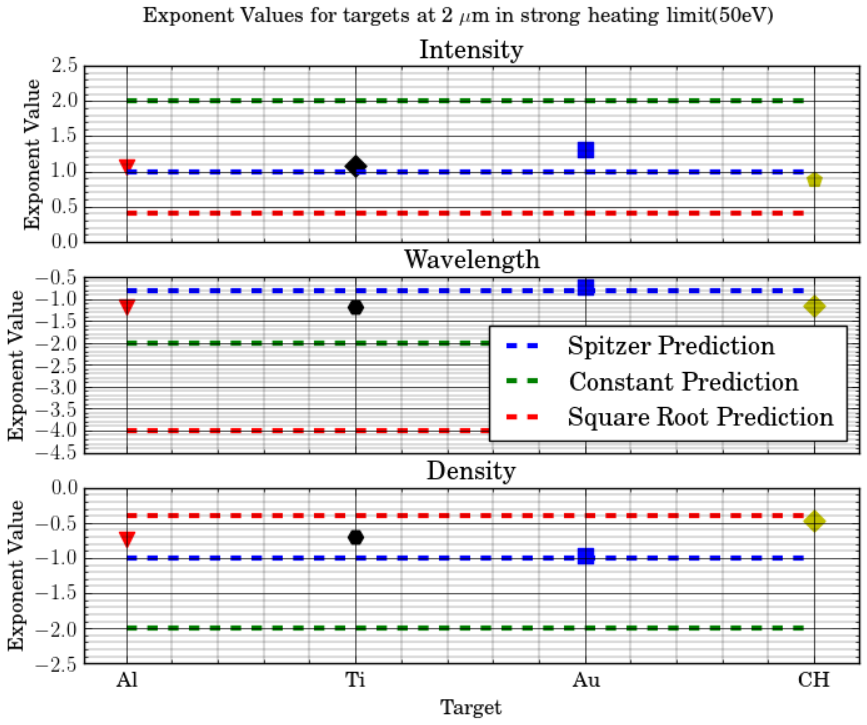

FIGURE 4.4: Figure showing dependencies for I_L, λ_L & n_i in the four targets: Al, Ti, Au & CH for T > 50 eV. The blue line represents the predicted Spitzer scaling, equation 4.6, while the orange line is the constant resistivity scaling, equation 4.9, & the green line is the square root resistivity, equation 4.10.

Run	I	λ	n_i
Al (10 eV)	1.17037	-1.3973	-0.9461
Al (50 eV)	1.06293	-1.1934	-0.7301
Al (100 eV)	0.96880	-1.1934	-0.5593
Ti (10 eV)	1.31882	-1.4853	-1.1457
Ti (50 eV)	1.07748	-1.177	-0.6947
Ti (100 eV)	0.97502	-1.0041	-0.6947
Au (10 eV)	1.60688	-1.1132	-1.2631
Au (50 eV)	1.31637	-0.7412	-0.9605
Au (100 eV)	1.24259	-0.2969	-0.7802

TABLE 4.6: Exponents from power laws for heating at 2 μm in the strong heating limit. The number in the bracket represents the lowest heating value allowed.

Table 4.6 & figures 4.3 - 4.5 show that in the limit of strong heating, the scalings of the respective targets are still best described via low temperature scalings.

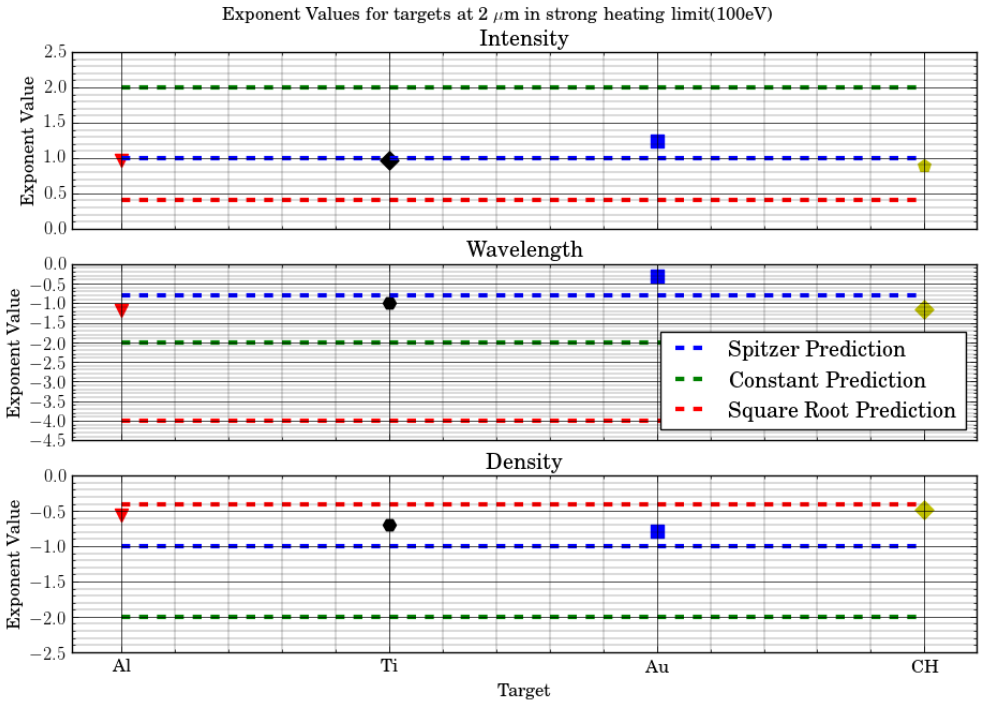

FIGURE 4.5: Figure showing dependencies for I_L, λ_L & n_i in the four targets: Al, Ti, Au & CH for T > 100 eV. The blue line represents the predicted Spitzer scaling, equation 4.6, while the orange line is the constant resistivity scaling, equation 4.9, & the green line is the square root resistivity, equation 4.10.

Furthermore it can also be noted that there is a slow drift towards the Sptizer regime in each of the targets when higher temperatures are used as the cut-off. In spite of this drift, the majority of results are still firmly represented by the low temperature scalings. This once again shows that the low temperature resistivity part of the evolution plays a major role in the overall heating of the target.

4.4.2 Role of Collisional Heating

A caveat in discussing the exponents above is that the heating of the target can also occur from the drag of fast electron beam, section 3.4.2. To consider the role of this heating, extra simulations were performed with collisional drag turned off for Al & CH targets. As well as this, an extra simulation was run which also considered no acceleration from the fast electron beam thereby resulting in a true rigid beam. The completely rigid beam was introduced to try and explain why the CH n_i exponent, value of 0.5, does not reproduce the Spitzer scaling value, 0.4.

Figures 4.6 - 4.7 & tables 4.7 - 4.9 present the calculated exponents from these simulations.

Run	I	λ	n_i
Al	1.17037	-1.3973	-0.9461
Al_{drag}	1.17371	-1.38557	-1.04787
CH	0.89455	-1.1440	-0.47617
CH_{drag}	0.89412	-1.14139	-0.47401
$CH_{drag+accl}$	0.89642	-1.14068	-0.47616

TABLE 4.7: Exponents for Al & CH with no drag & no acceleration at 2 μm. The subscript denotes the physical feature which has been turned off.

Run	I	λ	n_i
Al	1.54547	-1.74238	-1.35978
Al_{drag}	1.65364	-1.84295	-1.57542
CH	0.89452	-1.14852	-0.49701
CH_{drag}	0.90193	-1.35040	-0.47695
$CH_{drag+accl}$	0.90336	-1.14129	-0.49079

TABLE 4.8: Exponents for Al & CH with no drag & no acceleration at 4 μm. The subscript denotes the physical feature which has been turned off.

Run	I	λ	n_i
Al	1.41015	-1.29582	-1.35218
Al_{drag}	1.69495	-1.5338	-1.53862
CH	0.88295	-1.11727	-0.50418
CH_{drag}	0.89675	-1.13157	-0.47506
$CH_{drag+accl}$	0.91498	-1.13147	-0.50102

TABLE 4.9: Exponents for Al & CH with no drag & no acceleration at 6 μm. The subscript denotes the physical feature which has been turned off.

As it can be noted from figures 4.6 - 4.7 and tables 4.7 - 4.9, Ohmic heating is the dominant method in the targets. This is clearly seen in figure 4.7 where it is noted that the final temperatures in these simulations are remarkably similar.

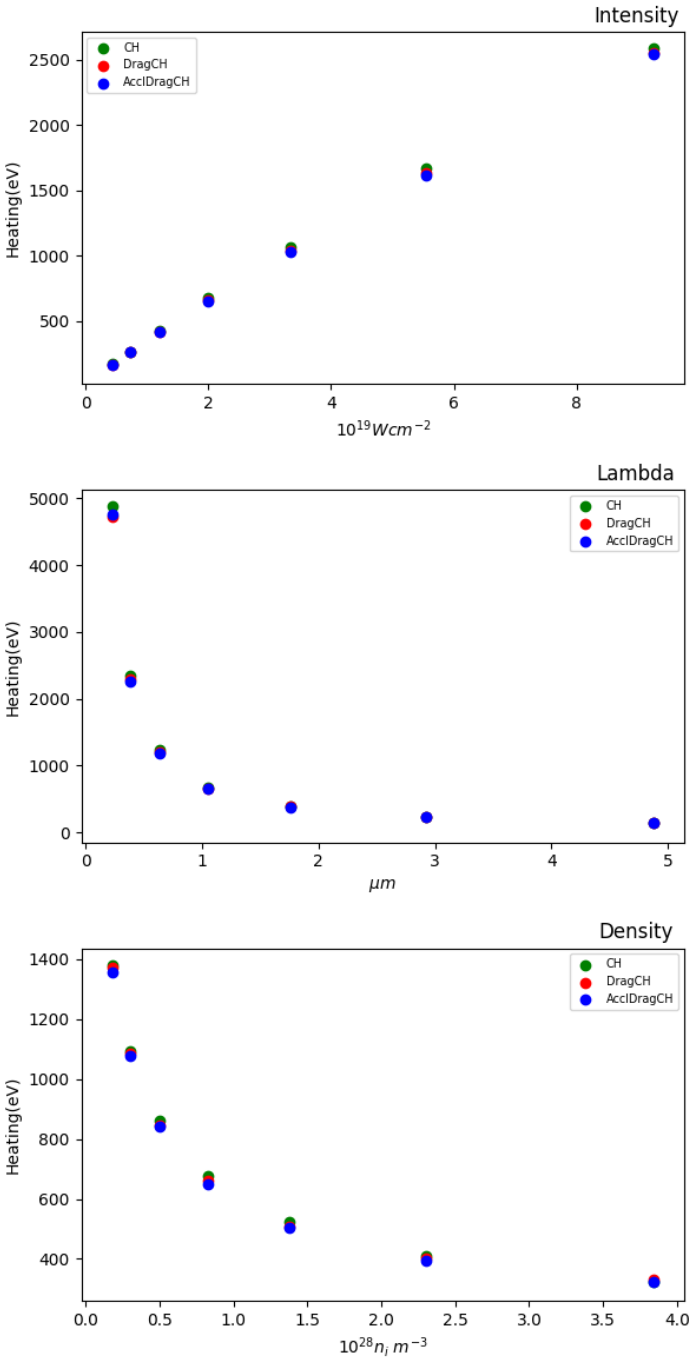

FIGURE 4.6: Plots showing temperatures reached in the various simulations for CH, with the standard run, CH, drag turned off, CH_{drag}, and a true rigid beam, $CH_{dragaccel}$.

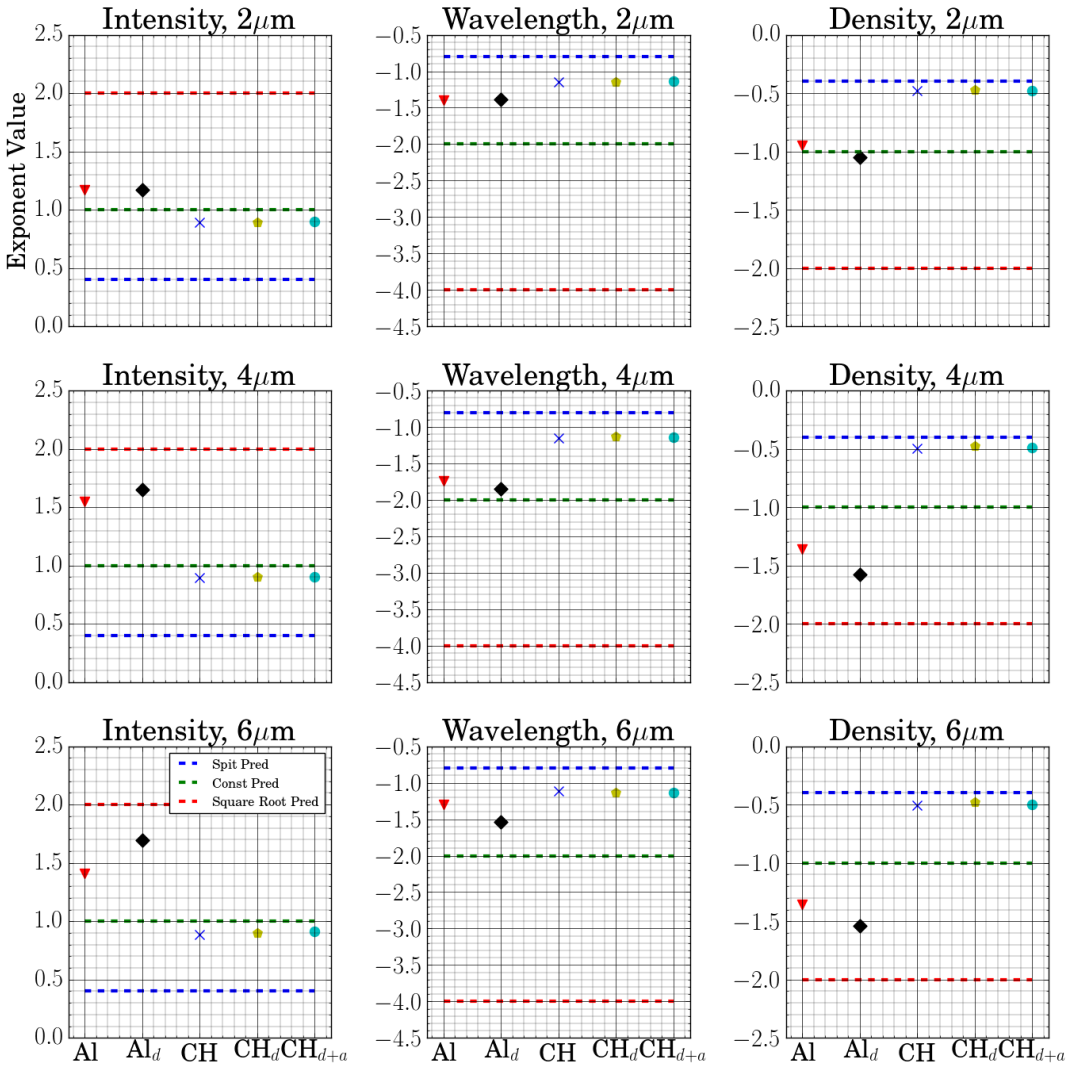

FIGURE 4.7: Figures showing the respective dependencies for I_L, λ_L & n_i in Al & CH. The subscript on the target depicts physical features turned off in the simulations. With d meaning drag has been turned off & d+a meaning both drag and acceleration have been turned off. The blue line represents the predicted Spitzer scaling, equation 4.6, while the orange line is the constant resistivity scaling, equation 4.9, & the green line is the square root resistivity, equation 4.10

.

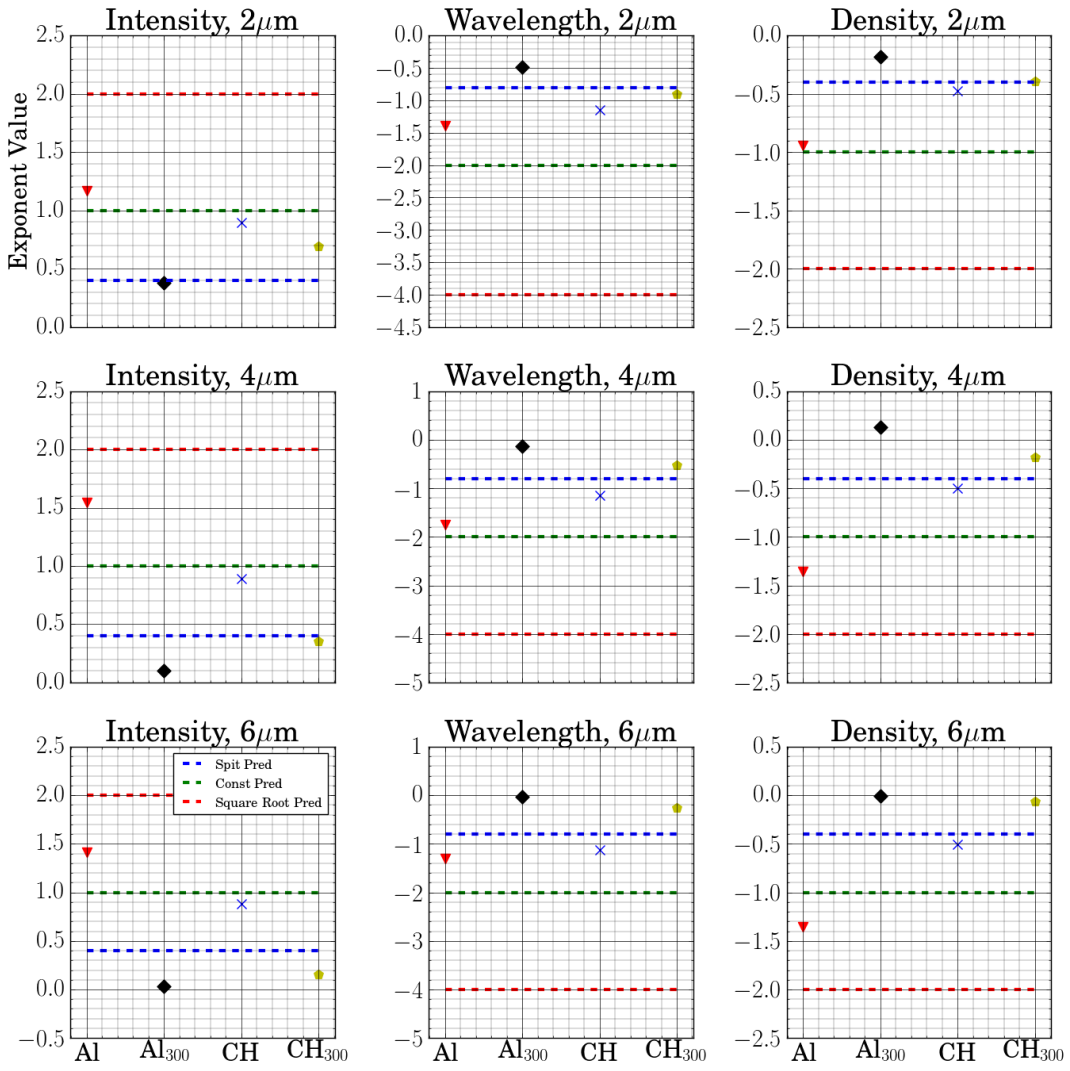

FIGURE 4.8: Figures showing the respective dependencies for I_L, λ_L & n_i in Al & CH which are set at a starting temperature of 300 eV. The blue line represents the predicted Spitzer scaling, equation 4.6, while the orange line is the constant resistivity scaling, equation 4.9, & the green line is the square root resistivity, equation 4.10.

4.4.3 Low Temperature Resistivity

From the previous graphs & tables, it can be seen that each of the targets are primarily described by low temperature scalings. This therefore raises the question of whether for simulations initialised at high enough temperature, the exponents are better described via Spitzer scalings. To investigate this, simulations were performed by starting Al & CH at 300 eV, denoted by Al_{300} & CH_{300}, with the exponents being found in figure 4.8 & tables 4.10 - 4.12.

Run	I	λ	n_i
Al	1.17037	-1.39737	-0.94616
Al_{300}	0.37674	-0.48238	-0.17757
CH	0.89455	-1.14409	-0.47616
CH_{300}	0.69361	-0.89574	-0.39153

TABLE 4.10: Exponents for targets starting at 300 eV simulations at depth of 2 μm.

Run	I	λ	n_i
Al	1.54547	-1.74238	-1.35978
Al_{300}	0.10347	-0.12865	-0.12965
CH	0.89452	-1.14852	-0.49701
CH_{300}	0.35588	-0.52057	-0.17690

TABLE 4.11: Exponents for targets starting at 300 eV simulations at depth of 4 μm.

Run	I	λ	n_i
Al	1.41015	-1.29582	-1.35218
Al_{300}	0.03053	-0.03558	-0.00728
CH	0.88295	-1.11727	-0.50418
CH_{300}	0.15600	-0.25548	-0.06068

TABLE 4.12: Exponents for targets starting at 300 eV simulations at depth of 6 μm.

Figure 4.8 & tables 4.10 - 4.12 clearly show that the simulations starting at 300 eV are operating in a different resistivity regime for both targets, with the CH target presenting dependencies closer to Spitzer in this run. This therefore shows that the low temperature resistivity has a major role in determining the maximum temperature of the target.

4.5 Conclusion

In this Chapter the predicted scalings of laser-target parameters, I_L, λ_L, n_i, for Ohmic heating from both the Spitzer resistivity model and a simple low temperature model were compared with the aid of numerical simulations. Results showed

that the use of Spitzer resistivity from the onset is insufficient, with scalings being more inline with the simple low temperature resistivity model used. The scalings therefore confirm that the evolution of the target through the low temperature phase is crucial to the overall temperature reached in the target at later stages and therefore fundamentally affects how one expects target heating to scale with core experimental parameters.

Chapter 5

The Role of Ionisation and Specific Heat Capacity in Ohmic Heating Scaling Predictions

5.1 Overview

In the following Chapter, a 0D heating model is presented which investigates the assumptions made in the derivations of the scalings in the previous Chapter: fixed ionisation and specific heat capacity. Results show that the assumption is valid, with calculated dependencies being very similar. It is also found that fixing the specific heat capacity and ionisation state result in higher overall temperatures compared to varying these two parameters. This was expanded further by fixing specific heat capacity and ionisation independently of one another and adding another resistivity model to the discussion. Results indicate that fixing the specific heat capacity produces larger temperatures than fixing the ionisation state. This suggests that there is a temperature dependence which is not considered when using the ideal gas heat capacity and thus underlines the importance of correctly characterising the specific heat capacity.

5.2 Background

In the previous Chapter the conclusion was drawn that the Spitzer resistivity does not fully represent various dependencies for the heating of a target from 1 eV but a prescriptive low temperature model, equation 4.7, provides a better description of the dependencies. As noted however, this resistivity model assumes that the ionisation state, Z^*, & specific heat capacity, C, are constant. Obviously this is not consistent with physical reality due to the resistivity being dependent upon Z^*, as shown in section 3.3. To consider these assumptions, a 0D heating model is constructed and discussed in the following section.

5.3 Model Description

The 0D heating model, which evolves temporally, will be referred to as HEAD: HEAting Dependencies. The model aims to solve the following equation

$$\frac{\partial T}{\partial t} = \frac{\eta \mathbf{j}_f^2}{C} \tag{5.1}$$

via the finite difference technique.

HEAD takes the initial temperature of the model to be 1 eV and the current density, $\mathbf{j}_f$, is calculated via equation 3.79,

$$\mathbf{j}_f = \frac{e\beta I_L}{\epsilon_f}. \tag{5.2}$$

where ϵ_f is calculated via equation 2.64. $\mathbf{j}_f$ is taken to be independent of time.

The ionisation state is calculated via the corrected TF model, equation 3.25. In the calculation of this model, the degeneracy for all targets is taken to be $g_0 = 2$ & $g_1 = 1$ [108]. First ionisation values for all materials considered are taken from the NIST website. The physical switch for Z^* is called "TF Constant", with True meaning that Z^* is fixed at its initial value, Z^*[1 eV], while False will allow for Z^* to vary. A plot of the TF model calculation can be found in figure 3.1.

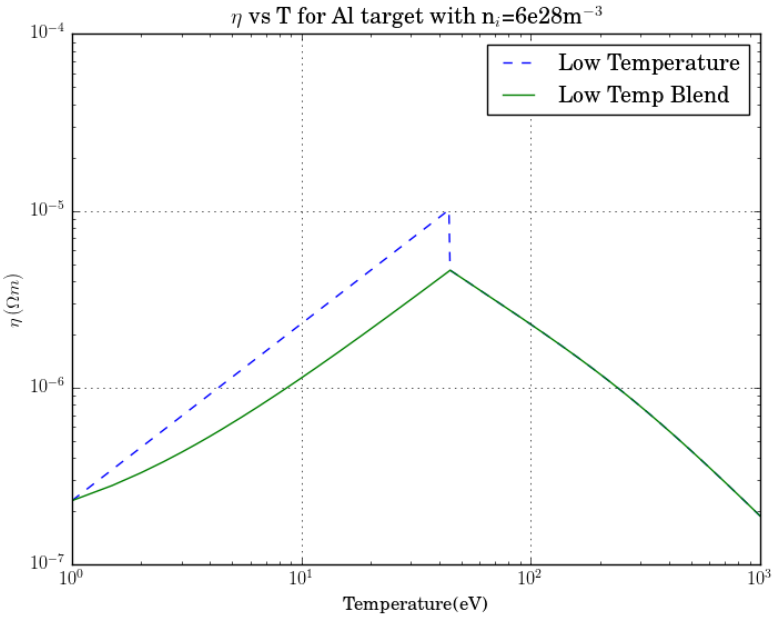

FIGURE 5.1: Figure showing Low Temperature resistivity, dashed blue line, vs Blended Low Temperature Resistivity, solid green line, between 1-1000 eV for an Aluminium target with $n_i = 6{\times}10^{28}$ m^{-3}.

To model the heat capacity, the TF-corrected model originally presented in unpublished work by Bell (1980) [117], which is also used by Davies (2002) [141] & ZEPHYROS [105], is used. In this approach, the specific heat capacity is assumed to be calculated at constant volume i.e.

$$C = \left(\frac{\partial E}{\partial T}\right)_V, \tag{5.3}$$

with this volume being that calculated for a fully bound atom.

To calculate the specific heat capacity of the entire target, equation 5.3 is multiplied by $n_e e$. The specific heat capacity has a similar physical switch to Z^*, with True fixing C to its initial value, C[1 eV], while False will allow C to vary.

HEAD can also take any resistivity model and was initially set-up up with the prescriptive model of low temperature, equation 4.7,

$$\eta = \eta_0 \left(\frac{T}{T_0}\right)^{\alpha}, \tag{5.4}$$

where T_0 is the initial temperature, 1 eV, & η_0 is the resistivity of the material at 1 eV. This initial value is calculated via the Lee-More model. Furthermore a switch temperature, T_c, for this resistivity model is taken at 44 eV [119]. Temperatures below this are represented by this low temperature approach, while temperatures above this are described by the Spitzer resistivity.

The implementation of this low temperature resistivity does come with its own caveats. For example the resistivity curve from equation 5.4 for an Al target, with $\alpha = 1$, is shown by the blue line in figure 5.1. Here it can be noted that there is a large discontinuity when switching between the two resistivity models at 44 eV. This is of course not physical at all. To correct for this, the following equation is used in place equation 5.4

$$\eta = \eta_0 + (\eta_{s,T_c} - \eta_0)\left(\frac{T - T_s}{T_c}\right)^{\alpha} \tag{5.5}$$

where η_{s,T_c} is the Spitzer resistivity at the switch temperature and T_s is the start temperature of the simulation, 1 eV in this case.

This curve, represented as the green line in figure 5.1, provides a far more realistic resistivity curve.

As it was discussed, after T_c the resistivity is described via the Spitzer approach, section 3.3.1. In HEAD this takes the prescriptive form, equation 3.34,

$$\eta = 10^{-4}\frac{Z^* ln\Lambda}{T^{\frac{3}{2}}}. \tag{5.6}$$

To calculate ln Λ, the temperature is reformulated to include the Fermi temperature, equation 3.37,

$$T_{corr} = \sqrt{T^2 + T_F^2}. \tag{5.7}$$

This correction stops the screening value dropping below the Thomas-Fermi screening length.

b_{max} is treated via the Debye length

$$b_{max} = \left(\frac{k_B T_{corr} \epsilon_0}{n_e e^2} \right)^{\frac{1}{2}}. \tag{5.8}$$

b_{min} is taken to be deBroglie wavelength [18]

$$b_{min} = \sqrt{\frac{2\pi\hbar^2}{m_e k_B T}} \tag{5.9}$$

As well as this, the Coulomb logarithm follows a similar formulation the Lee-More approach, equation 3.44,

$$\ln\Lambda = \max\left[2, \frac{1}{2}\ln\left(1 + \frac{b_{max}^2}{b_{min}^2}\right)\right]. \tag{5.10}$$

The Spitzer resistivity was not used due to the unrealistically higher values predicted at 1 eV, $\sim 1\times10^{-4}\,\Omega$m. By considering the first time step in equation 5.1 for Al, with a current density, $3.75\times10^{16}\,\mathrm{Am}^{-2}$, specific heat capacity, 4×10^{9} eV and δt, 1e-15, it can be seen that the temperature is 35157.25 eV which is non-physical. Furthermore, Milchberg et al (1988) [47, 141] showed that the resistivity of Al at 1 eV was $1.9\times10^{-7}\,\Omega$m, which is roughly 3 orders of magnitude smaller than the Spitzer predictions.

5.4 Simulation Setup

The first approach of this model was to repeat the simulations done in Chapter 4. The heating time is assumed to be 1 ps, with a step size of 1 fs and the various parameters varied are reprinted here for ease of the reader. The first table, 5.1, also includes the fixed current densities used in the simulations.

Run	I ($\mathrm{Wcm^{-2}}$)	λ (μm)	n_i	$\mathbf{j}_f$ $\left(10^{16}\,\mathrm{Am^{-2}}\right)$
A	2×10^{19}	1.053	See table 2	3.75
B	9.25×10^{19}			7.07
C	5.55×10^{19}			5.66
D	3.33×10^{19}			4.58
E	1.2×10^{19}			3.11
F	7.2×10^{18}			2.63
G	4.32×10^{18}			2.28
H	2×10^{19}	4.875	See table 2	0.67
I		2.925		1.15
J		1.755		2.04
K		0.6318		7.32
L		0.379		15.54
M		0.227		36.50
N		1.053	See table 2	3.75
O			See table 2	3.75
P			See table 2	3.75
Q			See table 2	3.75
R			See table 2	3.75
S			See table 2	3.75

TABLE 5.1: Parameters used in each run, with Run A representing the standard run.

Run	n_i (Al)	n_i (Ti)	n_i (Au)	n_i (CH)
A	6	5.71	5.9	0.829
N	27.8	26.4	27.3	3.4
O	16.7	15.9	16.4	2.3
P	10	9.52	9.83	1.38
Q	3.6	3.43	3.54	0.497
R	2.16	2.06	2.124	0.298
S	1.296	1.2744	1.2334	0.179

TABLE 5.2: Different ion densities used for the four targets given in units of $\times10^{28}$ $\mathrm{m^{-3}}$.

Each of these runs are performed twice, depending on the resistivity model & Z^* or SHC condition, with this being shown in table 5.3.

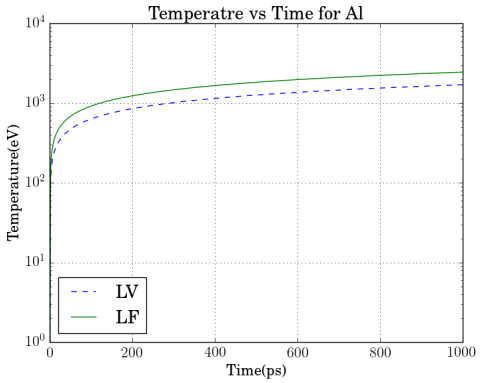

(A) Heating profiles for LF, solid green, and LV, dashed blue, for Al.

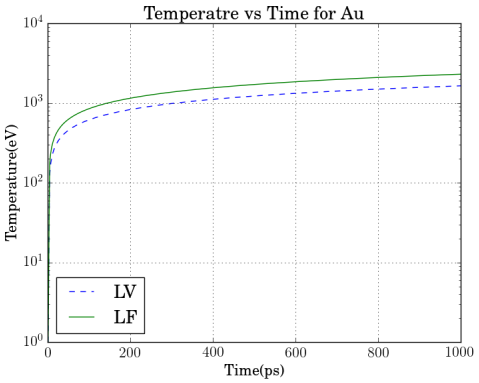

(B) Heating profiles for LF, solid green, and LV, dashed blue, for Au.

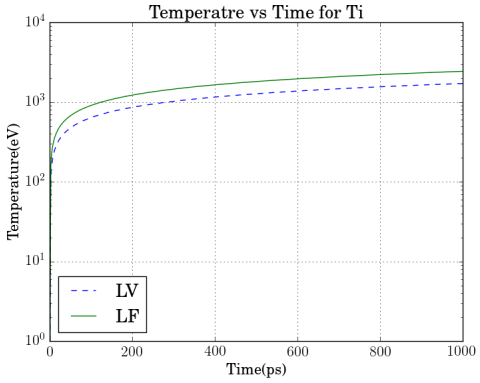

(C) Heating profiles for LF, solid green, and LV, dashed blue, for Ti.

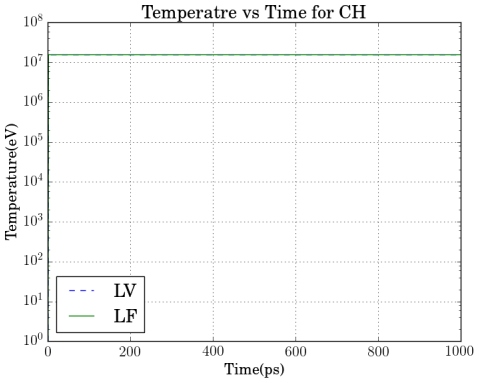

(D) Heating profiles for LF, solid green, and LV, dashed blue, for CH.

FIGURE 5.2: Figures showing heating profiles for Run A in the respective runs: LF, solid green, and LV, dashed blue, in (a) Al, (b) Au, (c) Ti & (d) CH.

Name	Resistivity	Z* Constant	C constant
Low Temperature Fixed (LF)	Low Temperature	True	True
Low Temperature Vary (LV)		False	False

TABLE 5.3: Two runs performed in HEAD. The description of how Z* & C are fixed is found in section 5.3 - values are fixed at the initial temperature of the model: 1 eV

5.5 Initial Results

Temperature profiles for Run A LF & LV in the 4 targets is presented in figure 5.2. Maximum temperatures are presented in tables 5.4 - 5.6. Exponent values from these runs are presented in figure 5.3 and table 5.7.

Run	B (eV)	C (eV)	D (eV)	A (eV)	E (eV)	F (eV)	G (eV)
Al I_L							
LF	4213	3489	2913	2456	2097	1818	1604
LV	2942	2430	2024	1703	1452	1257	1108
Au I_L							
LF	3985	3301	2747	2313	1971	1706	1504
LV	2829	2345	1956	1650	1409	1222	1079
Ti I_L							
LF	4192	3474	2901	2441	2082	1804	1592
LV	2958	2446	2040	1716	1464	1268	1117
CH I_L							
LF	5.5e7	3.5e7	2.3e7	1.6e7	1.1e7	7.6e6	5.7e6
LV	5.5e7	3.5e7	2.3e7	1.6e7	1.1e7	7.6e6	5.7e6

TABLE 5.4: Maxmimum temperatures for varying I_L described in tables 5.1 - 5.3

Run	H (eV)	I (eV)	J (eV)	A (eV)	K (eV)	L (eV)	M (eV)
Al λ_L							
LF	557	895	1461	2456	4334	8234	1.8e4
LV	383	616	1008	1703	3028	5848	1.4e4
Au λ_L							
LF	513	833	1368	2313	4100	8000	1.6e4
LV	375	604	983	1650	2910	5607	1.1e4
Ti λ_L							
LF	550	886	1449	2441	4314	8163	1.7e4
LV	388	623	1018	1716	3044	5801	1.2e4
CH λ_L							
LF	4.9e5	1.5e6	4.6e6	1.6e7	5.9e7	2.7e8	1.5e9
LV	4.9e5	1.5e6	4.6e6	1.6e7	5.9e7	2.7e8	1.5e9

TABLE 5.5: Maxmimum temperatures for varying λ_L described in tables 5.1 - 5.3

Run	N (eV)	O (eV)	P (eV)	A (eV)	Q (eV)	R (eV)	S (eV)
Al n_i							
LF	1345	1640	2003	2456	3191	1.1e4	8.4e4
LV	819	1048	1337	1703	2422	1.1e4	8.4e4
Au n_i							
LF	1275	1551	1890	2313	2842	3503	4769
LV	805	1024	1301	1650	2089	2646	3936
Ti n_i							
LF	1338	1631	1992	2441	3019	4944	3.9e4
LV	829	1059	1349	1716	2201	4379	3.9e4
CH n_i							
LF	1.1e6	2.6e6	6.6e6	1.6e7	2.9e7	3.8e7	4.5e7
LV	1.1e6	2.6e6	6.6e6	1.6e7	2.9e7	3.8e7	4.5e7

TABLE 5.6: Maxmimum temperatures for varying n_i described in tables 5.1 - 5.3

Variable	LF	LV
Al		
I_L	0.32	0.32
λ_L	-1.11	-1.14
n_i	-1.17	-1.34
Ti		
I_L	0.32	0.32
λ_L	-1.10	-1.11
n_i	-0.89	-1.04
Au		
I_L	0.32	0.32
λ_L	-1.12	-1.10
n_i	-0.42	-0.50
CH		
I_L	0.74	0.74
λ_L	-2.58	-2.58
n_i	-1.25	-1.25

TABLE 5.7: Exponents for Al, Au, Ti & CH target for the different runs.

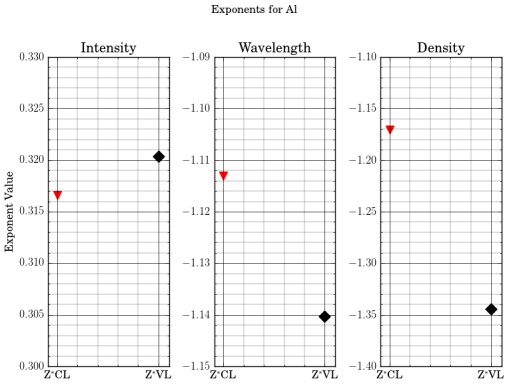

(A) Exponents from HEAD for Al.

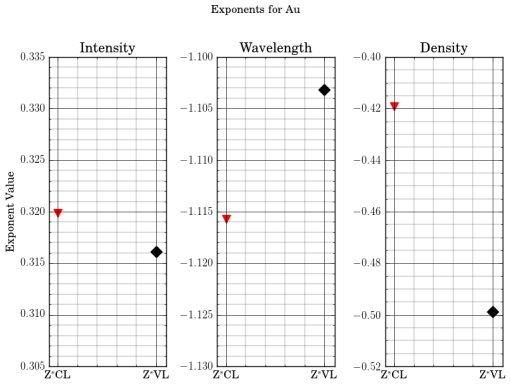

(B) Exponents from HEAD for Au.

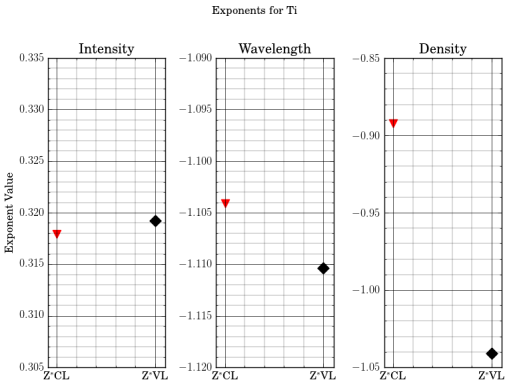

(C) Exponents from HEAD for Ti.

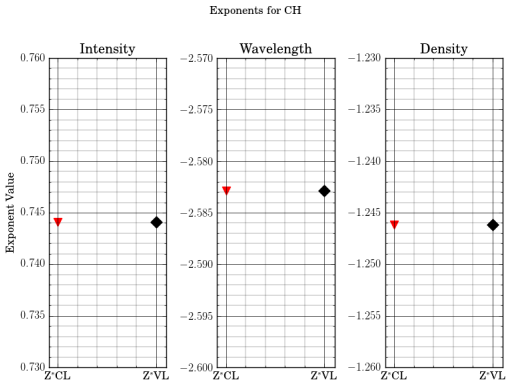

(D) Exponents from HEAD for CH.

FIGURE 5.3: Figures showing respective exponents for I_L, λ_L & n_i in (a) Al, (b) Au, (c) Ti & (d) CH. Acronyms described in table 5.3.

There are a variety of points to be noted from figures 5.2 & 5.3 and tables 5.4 - 5.7. From the heating profiles it can be seen that when the ionisation and heat capacity are treated as constant, LF, higher temperatures are found throughout all the targets. While the resistivity might be smaller in LF due to Z^* being fixed, the specific heat capacity is also fixed, resulting in higher temperatures. This therefore suggests that the specific heat capacity is more important in the heating profile of the respective targets. The one difference in this is the heating profile from CH, figure 5.2d. This is due to the large η_0, $\sim 10^{-5}\,\Omega$m, and small specific heat capacity which results in the two runs producing similar temperatures, as seen in tables 5.4 - 5.6, and thus the same exponents as seen in table 5.7.

It can also be noted that the exponents produced from I_L are considerably lower compared to the other exponents, with these being best described via the Spitzer. These lower exponents are due to the weaker heating exhibited in these runs, as seen in table 5.4. The weaker heating can be considered from the variables which

will change the rate of heating in this model, equation 5.1, $\mathbf{j}_f$ & C. The variation of $\mathbf{j}_f$, equation 5.2, has a weaker dependence on I_L than from λ_L as seen in table 5.1. Thus $\mathbf{j}_f$ will vary less in the I_L runs thereby resulting in less variation in the temperatures and smaller exponents.

Another point to be noted from the exponents is that the largest variation between LF & LV is in the dependency from n_i. This can be considered from the maximum temperatures from the density runs as seen figure 5.4 & table 5.6. Here it can be noted that for both Al & Ti, the temperatures produced in LV are smaller for runs N-Q while becoming comparable to LF for runs R-S. This is due to the reduction in the specific heat capacity which allows for rapid heating of the target,resulting in similar temperatures and thus larger exponents for LV.

These maximum temperatures from figure 5.4 & table 5.6 also show why the exponents in Au are far smaller compared to the other targets. Unlike the other runs, there is no rapid increase in temperature with a decrease in density. This is due to the decrease in Z^* being smaller as seen in table 5.8. The smaller reduction in Z^* results in a smaller reduction in the specific heat capacity and thus a smaller increase in temperature and smaller exponents.

Target	Z^* Ratio (Run A/ Run S)
Al	16.84
Au	8.23
Ti	19.77

TABLE 5.8: Exponents for Al, Au, Ti & CH target for the different runs.

Overall the results show that the assumption of a fixed Z^* & SHC lead to similar exponents, with only Au n_i suggesting it is not.

5.6 Variation of Z^* & SHC

As it was noted in figure 5.2 & tables 5.4 - 5.6, fixing Z^* & SHC results in higher temperatures. To consider this point in more detail, two things are done 1) Add a more complete resistivity model to fully elucidate these effects and 2) Expand table 5.3 to allow for the variation of Z^* & C independently. The reason for the full

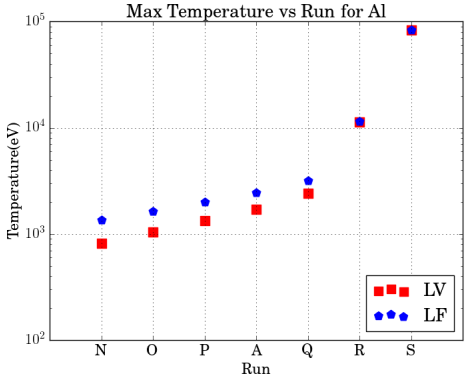

(A) Maximum temperatures reached in varying density for LV, red squares, & LF, blue pentagon, in Al.

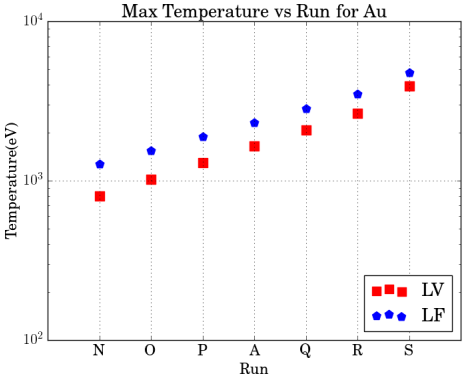

(B) Maximum temperatures reached in varying density for LV, red squares, & LF, blue pentagon, in Au.

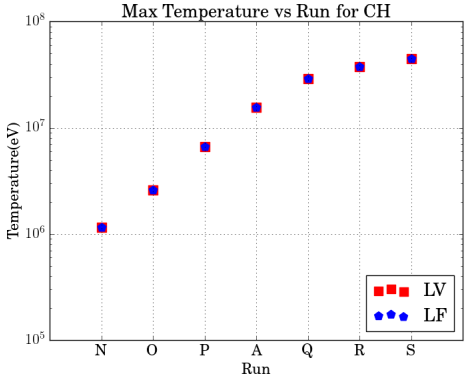

(C) Maximum temperatures reached in varying density for LV, red squares, & LF, blue pentagon, in CH.

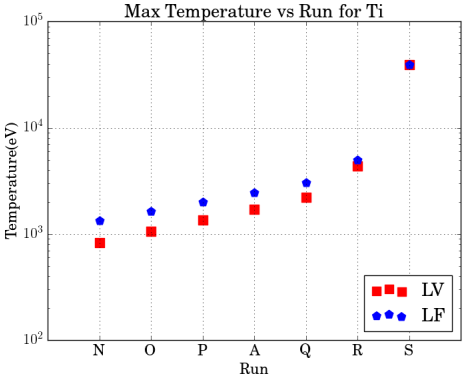

(D) Maximum temperatures reached in varying density for LV, red squares, & LF, blue pentagon,in Ti.

FIGURE 5.4: Maximum temperatures reached in varying density for LV, red squares, & LF, blue pentagon, in (a) Al (b) Au (c) CH & (d) Ti.

resistivity model is so that a description of electron statistics, such as degeneracy, can be included in the discussion. The first point is presented in section 5.6.1 and the second point, along with the results is presented in section 5.6.2.

5.6.1 A full resistivity model

For a full resistivity model the Robinson Resistivity was chosen, section 3.3.2.2. This requires solving equation 3.70,

$$\eta = \frac{3m_e}{4\pi e^2}\left[\int_0^\infty \mathbf{p}^3\tau(p)\left|\frac{\partial f_0}{\partial p}\right| d\mathbf{p}\right]^{-1}, \tag{5.11}$$

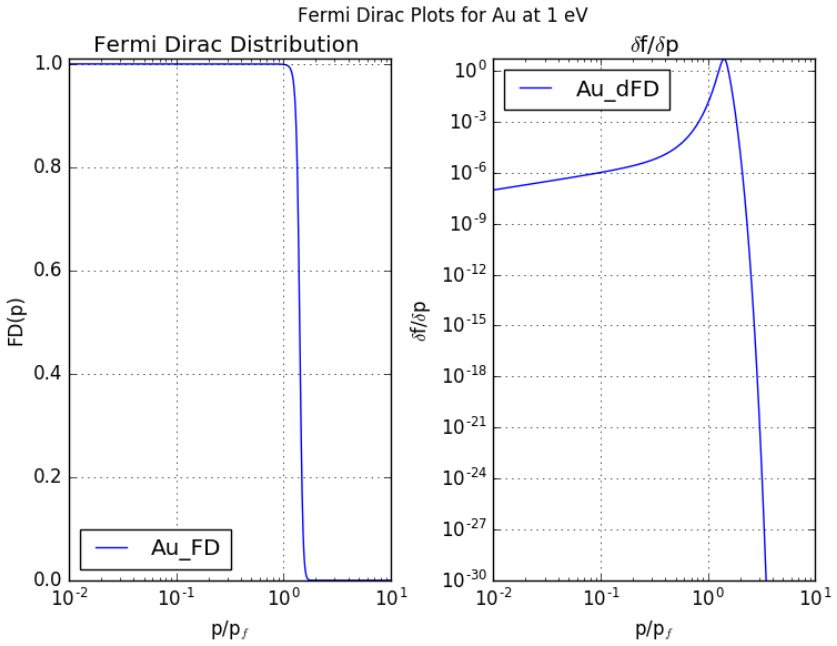

FIGURE 5.5: Figure of Fermi Dirac Distribution & $\frac{\partial f_0}{\partial p}$ for Au at 1 eV.

and therefore means that the Fermi-Dirac distribution, its change with respect to momentum, and collisions will all need to be resolved.

The Fermi-Dirac distribution requires for the chemical potential to be solved. This was done by solving equation 3.3

$$\frac{n_e \lambda_{th}^3}{2} = I_{\frac{1}{2}}(\alpha), \tag{5.12}$$

where $\alpha = \frac{\mu}{k_B T}$ & $\mathrm{I}_{\frac{1}{2}}$ is a Fermi integral to the $\frac{1}{2}$th order, equation 3.4.

The Fermi-integral was solved via the Newton-Raphson method for α. Plots of the Fermi-Dirac distribution & $\frac{\partial f_0}{\partial p}$ can be found in figure 5.5 for Au at 1 eV.

In calculating the collisions, only electron-ion & electron-electron collisions were selected. This means that for materials, Al & CH, where electron-neutral collisions are a non-trivial part of the resistivity at 1 eV, $\mathrm{Z}^*\,[1\mathrm{eV}] < 1$, are neglected [4].

The collision calculations also requires for the Lindhard theory to be calculated, equation 3.63. Figure 5.6 presents the Lindhard screening length, red, the Thomas-Fermi screening, Lindhard theory at T = 0 green, and the Debye length, blue.

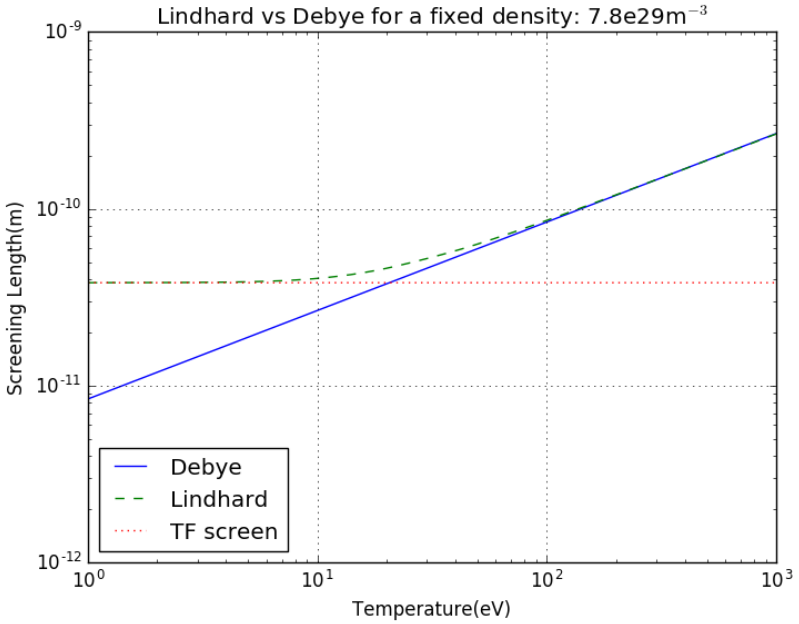

FIGURE 5.6: Figure showing various screening lengths vs temperature for a fixed of solid density of $1{\times}10^{29}$ m^{-3}. The blue solid line represents λ_D, green dashed line the Lindhard screening and red dotted line the Thomas Fermi screening.

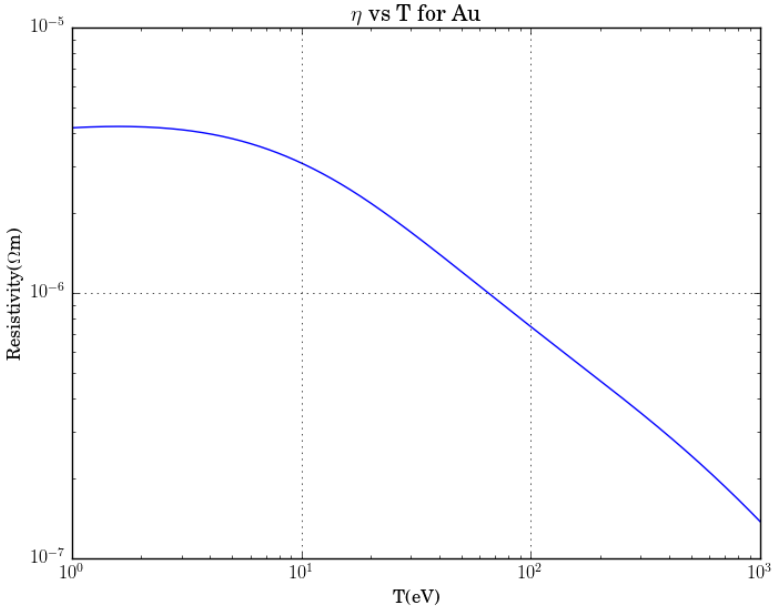

FIGURE 5.7: Robinson Resistivity for Au, $n_i = 5.9{\times}10^{28}$ m^{-3}, between 1 - 1000 eV

The resistivity curve for Au can be seen in figure 5.7.

5.6.2 Varying Z* & SHC

Table 5.3 was expanded so that Z* & C were varied independently, with table 5.9 presenting the runs undertaken.

Name	Z* Constant	C constant
Fixed (F)	True	True
Fixed Z (FZ)	True	False
Fixed C (FC)	False	True
Vary (V)	False	False

TABLE 5.9: Runs performed for Z* & SHC. We denote each variable by L (low temperature) or R (Robinson) + F, FZ, FC or V as appropriate.

To keep from the convolution of results, only Run A, table 5.1, was considered. Cu was also added, with its parameters found in table 5.10.

Target	ρ (kg m^{-3})	Density (m^{-3})	Z
Cu	8603	8.05×10^{28}	29

TABLE 5.10: Material Properties used in the construction of the cone

The temperature profiles for the 3 targets with the four runs, table 5.9, can be found in figures 5.8 - 5.10. Here the contrast in the heating profiles can be seen, with fixing the parameters resulting in higher temperatures, suggesting that the specific heat capacity has a temperature dependence. This can be considered from the internal energy of a material

$$E_e = f(T)Z^*(T)n_i k_B T. \tag{5.13}$$

For an ideal gas, T>>T_f, this reduces to

$$E_e = \frac{3}{2}n_e k_B T. \tag{5.14}$$

Here it can be seen that the use of the ideal gas neglects the temperature dependence of f(T) & Z*(T) in equation 5.14. The neglection of this temperature dependence will therefore result in an overestimation of the specific heat capacity

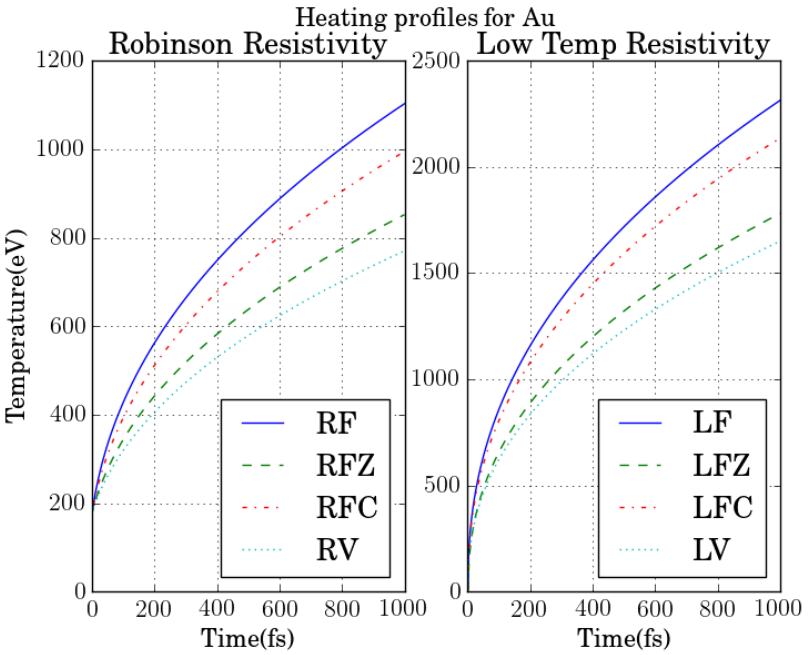

FIGURE 5.8: Temperature profiles for Au with Robinson Resistivity, R, & Low Temperature, L, Resistivity for runs described in table 5.9. The fixing of the Z^* & SHC follow the same process as originally discussed in 5.3 - values are fixed at the initial temperature of the model: 1 eV

and will underestimate the heating in the low temperature regime. This will result in an incorrect description of the target and predicted smaller exponents as shown in Chapter 4 and this Chapter.

5.7 Conclusion

In this Chapter a 0D heating model, which evolves temporally, was constructed to test the assumption made for derivations of the analytical scalings in the previous Chapter: the ionisation state, Z^*, and the specific heat capacity, C, are constant. Results from this model showed that the assumption of fixing two parameters results in similar exponents. Results from the model also showed that fixing these two parameters produces larger overall temperatures compared to the variable case. To expand upon this, the ionisation state and specific heat capacity were varied independently while also adding another resistivity, Robinson, to the investigation. Results showed that fixing the specific heat capacity has a larger impact on the temperature when compared to fixing the ionisation state. This

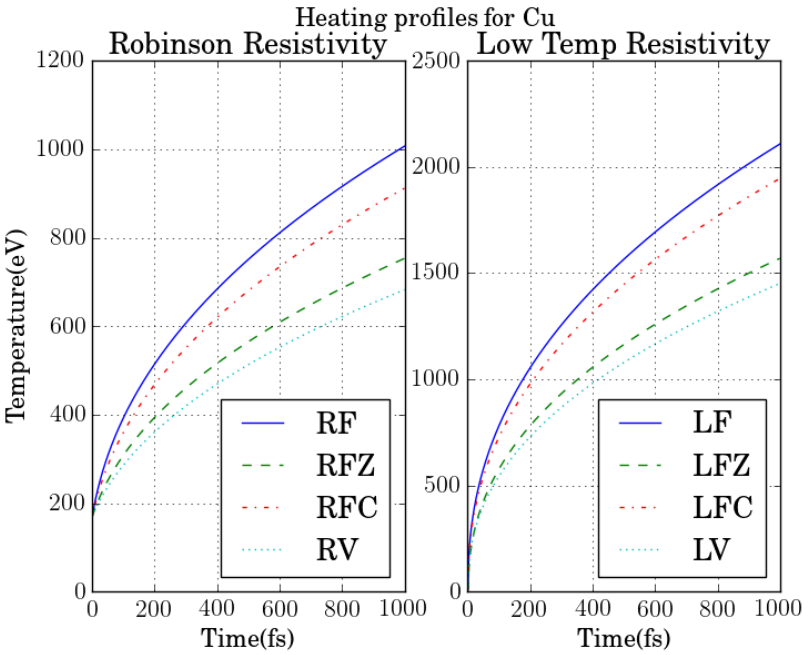

FIGURE 5.9: Temperature profiles for Cu with Robinson Resistivity, R, & Low Temperature, L, Resistivity for runs described in table 5.9. The fixing of the Z^* & SHC follow the same process as originally discussed in 5.3 - values are fixed at the initial temperature of the model: 1 eV

therefore shows that the selection of specific heat capacity is of crucial importance to producing accurate analytical and numerical results.

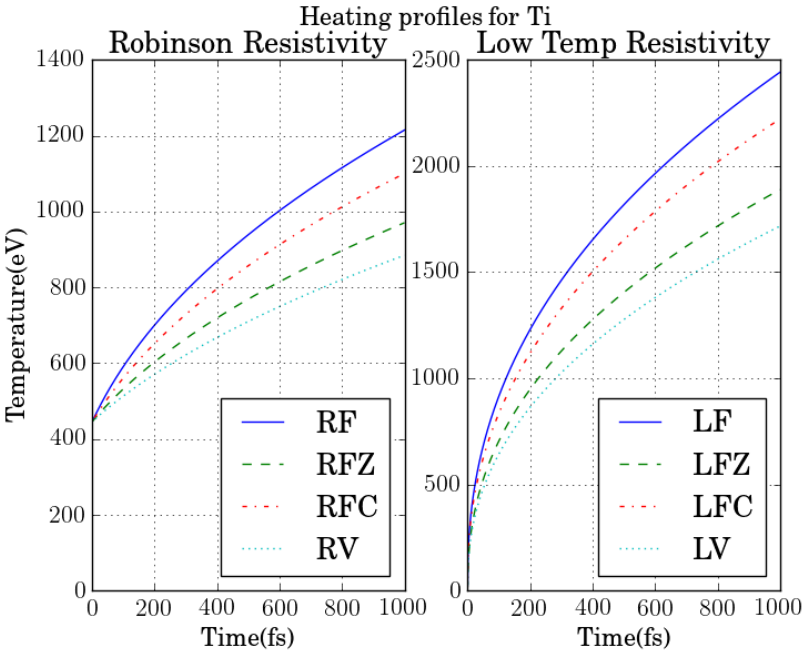

FIGURE 5.10: Temperature profiles for Ti with Robinson Resistivity, R, & Low Temperature, L, Resistivity for runs described in table 5.9. The fixing of the Z^* & SHC follow the same process as originally discussed in 5.3 - values are fixed at the initial temperature of the model: 1 eV

Chapter 6

The Production of A Uniform Heating Region From An Inverse Conical Taper In A Resistive Collimated Target

6.1 Overview

In the following Chapter, the generation of uniform heating for fast electron heating experiments is investigated via various targets designs based upon the inverse conical taper, section 3.4.3.2. Results show that a 2 material design with "square" geometry of an Al "cone", which has a truncated inverse pyramid shape in this geometry, connected to a Cu wire produce not only the highest temperatures but also larger regions of uniform heating. The higher temperatures are found not only due to the larger specific heat capacity and resistivity of Cu, resulting in larger confining magnetic fields, but also due to the fact that these magnetic fields extended into the target, further collimating the beam. Uniform heating was found to be generated from inhomogeneous transport of the fast electron beam through the wire, which results in the fast electron current not decreasing monotonically but instead varying spatially which produces regions of quasi-uniform heating. While the exact reasons for this were not fully elucidated, further work considered the optimisation of this uniform heating and the role of inhomogeneous transport. First, a variety of different Z wires were investigated. Smaller Z wires result in a

monotonically decreasing fast electron current density and thus no uniform heating. Higher Z wires did result in a larger variation in the transport of the fast electron beam but this was also found to suppress uniform heating. Other work investigated varying the confinement parameter via either changing I_L or λ_L. For λ_L it was found that due to the large change in the current density, completely different transport properties were obtained leading to a change in the uniform heating. Decreasing λ_L resulted in the generation of large magnetic fields within the wire, suppressing uniform heating due to the constantly varying transport pattern. Increasing λ_L resulted in a rapid reduction of the spatial variation of the fast electron beam and regions of uniform heating in shallower regions of the wire. On the other hand, varying I_L resulted in similar transport patterns to the original run. Increasing I_L resulted in a reduction in the spatial modifications of the fast electron beam, resulting in an absence of uniform heating. Decreasing I_L produced larger spatial modifications of the beam and resulted in slightly shallower regions of uniform heating. Work also considered whether the uniform heating observed is dependent upon a certain β value. Results showed that the uniform heating is independent of β but the depth at which it occurs is dependent upon β due to the current density dependence upon it. Finally, the effect of geometry was considered by comparing a target in cylindrical geometry which had the same area as the "square" wire. It was found that uniform heating occurred in both geometries but the transport of the fast electrons is changed. This change arises due to the cylindrical target having a larger radius, leading to weaker interior magnetic fields and thus a far more stable transport pattern compared to the "square" target.

6.2 Introduction

If Ohmic heating is to be used in the generation of HDM, sections 1.2.4 & 3.6, periods of uniform heating will be preferable so that a consistent picture is produced. However, as it was previously discussed in section 3.4.3.2, the fast electron beam has a half angle, θ_{fe}. This causes the fast electron beam to spread, leading not only to a reduction in heating but also variations in the current density. Unlike other parameters, i.e. ϵ_f, τ_H etc, this parameter cannot be tuned by varying laser parameters. Instead novel target designs, such as the inverse conical taper proposed by Robinson et al (2015) [97, 111] which was also discussed in section 3.4.3.2, are

used. The inverse conical taper reduces θ_{fe} via collisions with the conical wall, after which the fast electron will have an angle θ and a resulting velocity

$$v_{new} = v_{old} \cos\theta. \tag{6.1}$$

While the inverse conical taper will reduce the longitudinal dispersion of the fast electron beam it will not be completely removed therefore still resulting in periods of non-uniform heating. In what follows, a variety of different targets are presented which aim to reduce the effect of this longitudinal spreading and to optimise uniform heating so it could possible be used in an experimental setting.

6.3 Conical Design

The truncated cone was always constructed of Aluminium, with an side length of 10 μm which expanded to 18 μm over a distance of 50 μm thus giving a cone half-angle of 5.71°. The wire, connected to the cone, had a radius of 10 μm and was 150 μm long, resulting in the tota target, cone+wire, being 200 μm in length. In all approaches, it was assumed that the cone and wire had a "square" geometry. While this means that the "cone" will actually be an inverse truncated pyramid, it will still have the same characteristic properties as the cylindrical cone, i.e. a reduction in fast electron angle. The five targets designed, labelled I-V, are shown schematically in figure 6.1 & descriptions of the cones can be found in table 6.1.

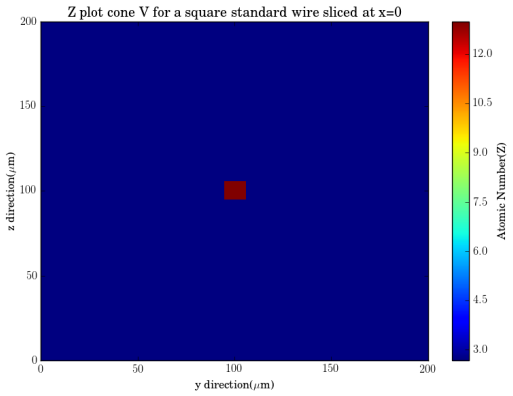

(A) Atomic Number(Z) for Cone I at x = 0

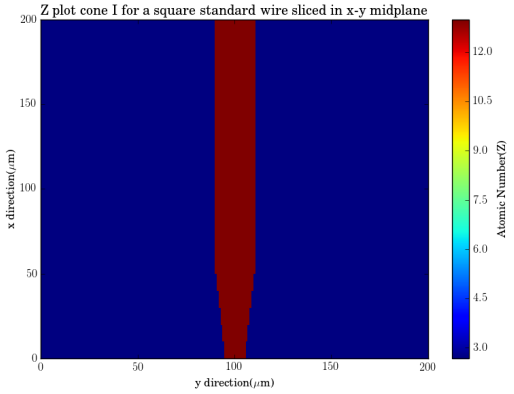

(B) Atomic Number(Z) for Cone I in x-y midplane

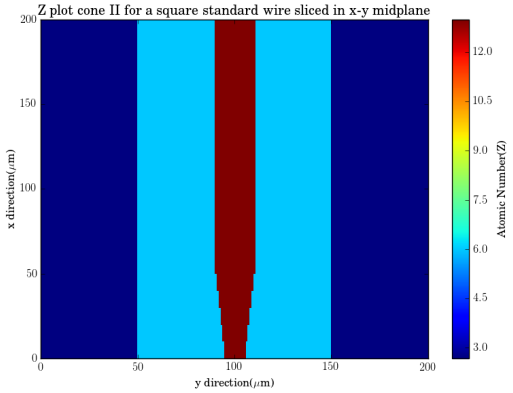

(C) Atomic Number(Z) for Cone II in x-y midplane

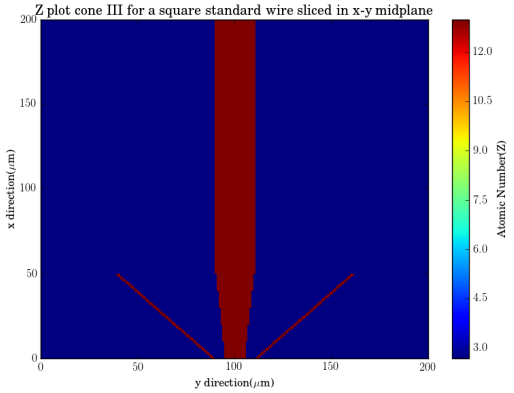

(D) Atomic Number(Z) for Cone III in x-y midplane

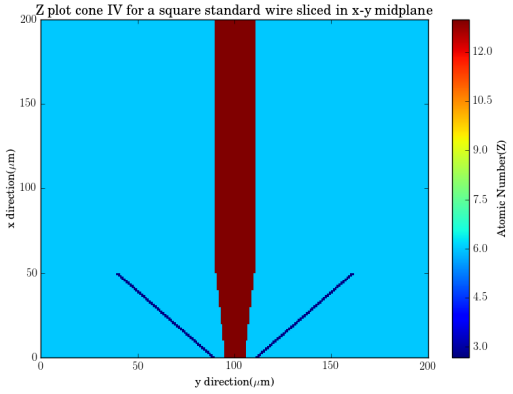

(E) Atomic Number(Z) for Cone IV in x-y midplane

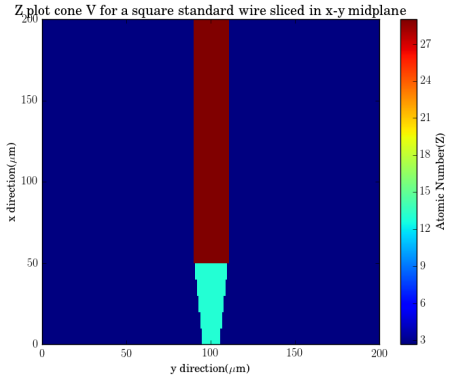

(F) Atomic Number(Z) for Cone V in x-y midplane

FIGURE 6.1: Atomic Number(Z) plots for cones I - V.

Cone	Wire material	Substrate	Extra target material
I	Al	CH_2	N
II		CH_2 (0-50, 150-200), C (50-150)	N
III		CH_2	Y: diagonal struts (Al)
IV		C	Y: diagonal struts (CH_2)
V	Cu	CH_2	N

TABLE 6.1: Cone characteristics

The material properties used are found in table 6.2.

Target	ρ (kg m^{-3})	Density (m^{-3})	Z
Al	2705	6×10^{28}	13
C (Vitreous)	1500	7.49×10^{28}	6
CH_2	925	3.96×10^{28}	2.67
Cu	8603	8.05×10^{28}	29

TABLE 6.2: Material Properties used in the construction of the cone

6.4 Numerical Setup

The five targets were then simulated on ZEPHYROS, section 3.5. Each simulation has a grid size of 200 × 200 × 200, with each cell being 1 μm in size. 4×10^8 macro-particles were used, resulting in 99502 being injected per time step and 1243 being injected per cell. The Lee-More resistivity was used throughout. The temporal profile of the laser beam is a top-hat function of 1 ps. The laser radius was also treated as a top-hat function, with this being equal to the initial cone radius, 5 μm. The fast electrons were described via an exponential distribution: $\exp\left(-\frac{E}{T_F}\right)$. β, section 2.7.2, was taken to be 0.3. The magnetic field evolution was described via equation 3.92. 6 separate simulations were performed, with these being presented in table 6.3.

Run	I_L (Wcm^{-2})	λ (μm)	τ_L (ps)	Fast e- Temp (MeV)	Fast Electron Angle (θ)
A	5×10^{19}	1	1	2.61	0
B					15
C					30
D					45
E					60
F					75

TABLE 6.3: Parameters used in each run, with Run A representing the standard run.

6.5 Results

6.5.1 Initial Results

The heating profiles from each of the cones for each of the runs were taken in the middle of y & z plane, y = z = 100 μm, and were measured between 40 - 100 μm. To qualify uniform heating from these lineouts, the following algorithm was used.

Algorithm 1 Uniform Heating I

```
1: function Finding Values(temp_input)
2:     disn_list = [ ]
3:     temp_list = [ ]
4:     for i in range(len(temp_input)) do
5:         if 39 =< i =< 99 then:
6:             diff_one = temp_input[i] - temp_input[i-1]
7:             diff_two = temp_input[i] - temp_input[i-2]
8:             diff_three = temp_input[i-1] - temp_input[i-2]
9:             if all(abs(diff_one, diff_two, diff_three)) =< 2 then:
10:                disn_list ← i, i-1, i-2
11:            end if
12:        end if
13:    end for
14:    order_list = Remove duplicates and order: disn_list
15:    for j,k in enumerate(order_list) do:
16:        temp_list[k] = temp_input[j-1]
17:    end for
18:    calculate_uniformheating (temp_list, order_list)
19: end function
20: function Calculating Uniform Heating(temp_list, order_list)
21:    res_disn = [ ]
22:    res_temp = [ ]
23:    p = 0                                  ▷ Iterator used to access results list
24:    for m in range(len(disn_list)) do:
25:        res_disn: ← disn_list[m], res_temp: ← temp_list[m]
26:        if abs(res_disn[p]-res_disn[p-1] > 1) or m+1 == len(order_list) then
27:            if not m+1 == len(order_list) then
28:                remove last element from both lists
29:                p = 0
30:            end if
31:            average_temp = avg(res_temp)
32:            Difference = max(res_temp) - min(res_temp)
33:            Distance = res_disn
```

Algorithm 2 Uniform Heating II

```
            if Difference <= 2 then
                print(average_temp)
                print(Difference = max(res_temp) - min(res_temp))
                print(Distance = res_disn)
            end if
            res_disn = [ ]
            res_temp = [ ]
            res_disn: ← disn_list[k], res_temp: ← temp_list[m]
        end if
        p += 1
    end for
end function
temp_input = read output temperature files ▷ temp_input is a list containing temperatures
Finding Values(temp_input)
```

This method does mean that we allow for small variations within regions of uniform heating and as such the average temperature, $\bar{T}$, is used instead. As well as this, the variation in the temperature, δT = T_{max}-T_{min}, is presented with values > 2 eV neglected.

One thing which can be noted from the algorithm is that some periods of uniform heating in this algorithm will be neglected i.e. consider the following.

Algorithm 3 Example List

```
disn_list = [77, 78, 79, 80, 81, 82, 83, 84, 85]
temp_list = [227.1, 226.1, 226.8, 227.8, 228.4, 229.1, 230.0, 230.1, 231.8]
difference = 5.7
```

Here it can be seen that there are two periods of uniform heating could be gained from here: 77-80 & 83-85. However while these are periods of uniform heating, they are not optimum in heating experiments. By this it is meant that the ideal period of uniform heating will be an almost constant period temperature surrounded by considerably different temperatures, therefore allowing for it to be easily detected in an experimental setting. The scenario above fails due to the two periods of

uniform heating not being easily distinguishable from one another, leading to the overall picture of the temperatures being a linear growth, as seen by the *difference* value.

Graphs of the temperature lineouts for the 6 runs can be found in figure 6.2 and the uniform heating exhibited in these figures is found in table 6.4.

Cone	Run	Distance (μm)	$\bar{T}$ (eV)	δT (eV)
I	D	60-65	329.67	1.70
III	C	79-81	133.33	2.00
	D	61-64	329.50	2.00
		91-98	217.17	2.00
		84-89	170.38	1.70
IV	F	53-58	101.43	1.60
		81-86	138.17	2.00
V	D	68-70	304.67	1.70
		75-82	316.15	1.80
	E	75-77	216.87	2.00
	F	60-62	165.03	2.00

TABLE 6.4: Regions of uniform heating with T_{max} - $T_{min} \leq 2.0$

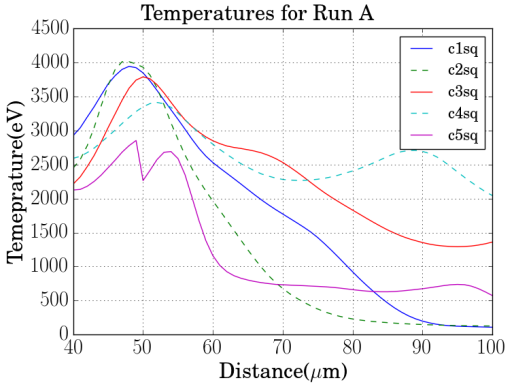

(A) Temperature lineout for Run A

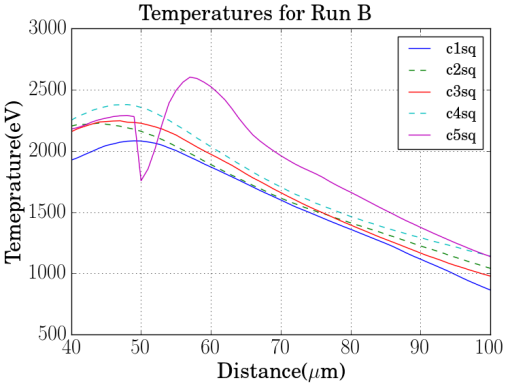

(B) Temperature lineout for Run B

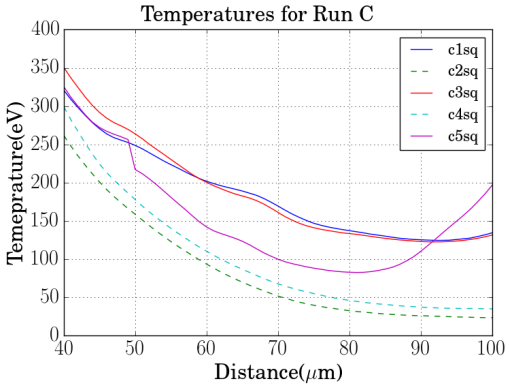

(C) Temperature lineout for Run C

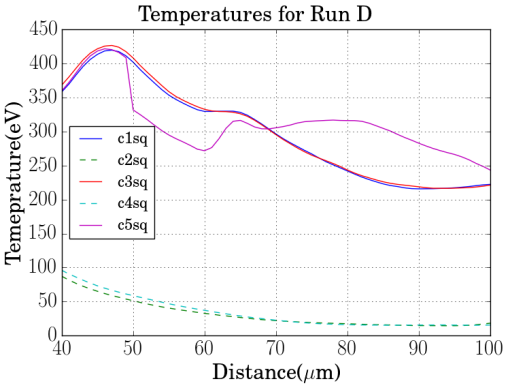

(D) Temperature lineout for Run D

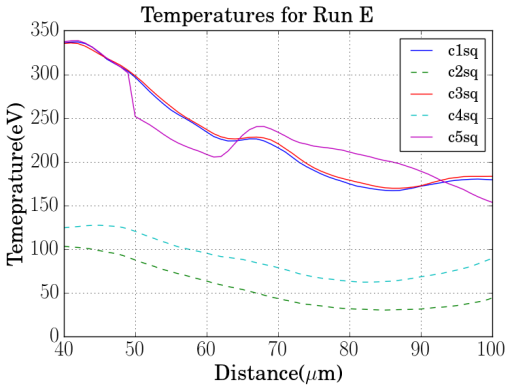

(E) Temperature lineout for Run E

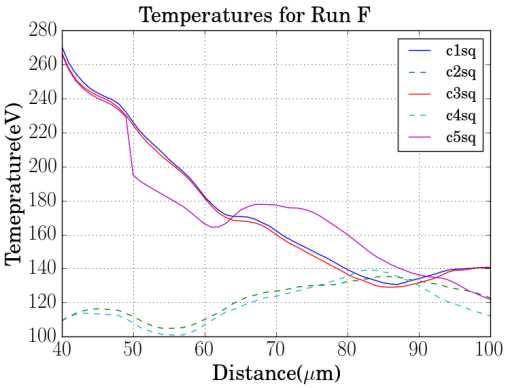

(F) Temperature lineout for Run F

FIGURE 6.2: Temperature lineout for cones sliced in y-z midplane. Dashed line denotes targets with Carbon in the substrate.

There are a few things of interest to note from figure 6.2 & table 6.4. First and foremost, it is noted that uniform heating is only present in Runs D-F but not observed, barring Cone III Run C, for Runs A-C. Secondly, it is also seen from these two sets of runs that in the latter case, A-C, the substrate plays little to no role in the overall temperature evolution of the guiding structure while it plays a major role in the temperature evolution for the runs, D-F. Each of these are discussed in more detail in the following two sections.

The reason for Runs A-C substrate playing little role in the evolution of the temperature can be considered from the confinement condition, equation 3.100, which is

$$B_\phi L_\phi > \frac{\gamma_e m_e c}{e}\left(1-\cos\theta_{fe}\right) = \frac{\mathbf{P}_f}{e}\left(1-\cos\theta_{fe}\right). \tag{6.2}$$

where $\mathbf{P}_f$ is the fast electron momentum.

The confinement conditions are therefore

Run	θ_{fe} (Degrees)	$(B_\phi L_\phi) >$
A	0	$0 \cdot \frac{\mathbf{P}_f}{e}$
B	15	$0.034 \cdot \frac{\mathbf{P}_f}{e}$
B′	9.29	$0.013 \cdot \frac{\mathbf{P}_f}{e}$
C	30	$0.133 \cdot \frac{\mathbf{P}_f}{e}$
C′	24.29	$0.089 \cdot \frac{\mathbf{P}_f}{e}$
D	45	$0.292 \cdot \frac{\mathbf{P}_f}{e}$
D′	39.29	$0.226 \cdot \frac{\mathbf{P}_f}{e}$
E	60	$0.500 \cdot \frac{\mathbf{P}_f}{e}$
E′	54.29	$0.416 \cdot \frac{\mathbf{P}_f}{e}$
F	75	$0.741 \cdot \frac{\mathbf{P}_f}{e}$
F′	69.29	$0.646 \cdot \frac{\mathbf{P}_f}{e}$

TABLE 6.5: Confinement criteria for A - F. The superscript denotes the angle after one collision with cone.

It can clearly be seen from the criteria presented in table 6.5, that almost all of the fast electrons will be confined within the guiding structure for Runs A-C, therefore resulting in the propagation of the fast electrons being the defining feature of the

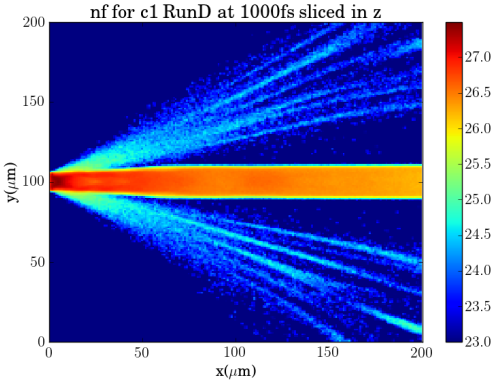

(A) $\log_{10}$ plot of fast electron density sliced at z = 100 μm for cone I Run D

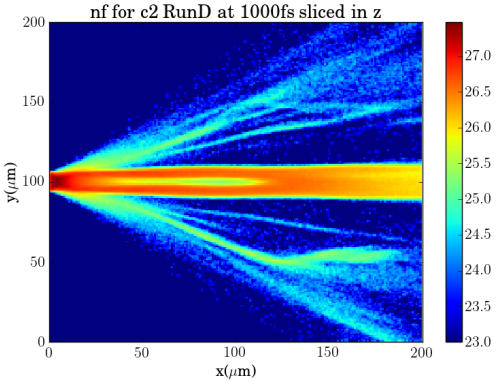

(B) $\log_{10}$ plot of fast electron density sliced at z = 100 μm for cone II Run D

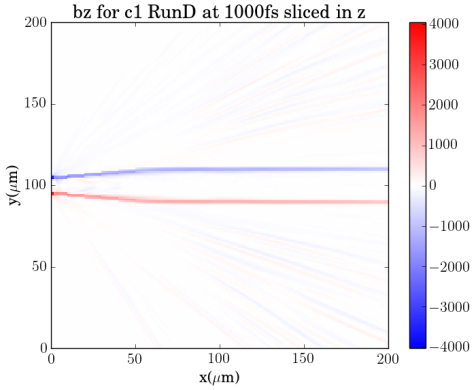

(C) B_z at z = 100 μm for Cone I.

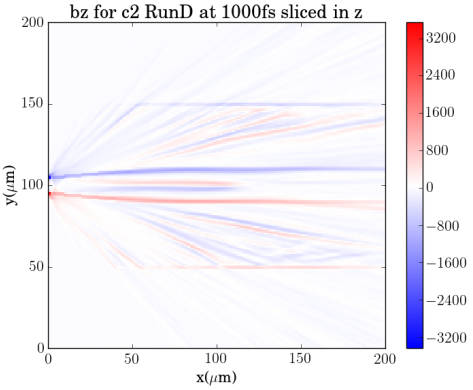

(D) B_z at z = 100 μm for Cone II.

FIGURE 6.3: 2D plots for cone I & II showing (a) - (b): n_f & (c) - (d): B_z respectively. All plots sliced at z = 100 μm.

heating profiles. The larger density of fast electrons within the wire results in both stronger heating and larger magnetic fields. This, in-turn, results in far larger variation in the current density producing greater variations in the heating profiles, as seen in figures 6.2a - 6.2c. The one slight variation in this trend occurs in Run C. Here it can be noted that the temperatures produced are lower than the ones found in Run D, which has a 15° larger θ_{fe}. This is due to hollowing of the fast electron beam from interior magnetic fields.

In the D-F cases however it is noted that the there is a difference in the heating profiles between the cones with a CH_2 substrate, I, III & V, and a C substrate, II & IV. In each of these runs, it can be seen that targets with a C substrate produce temperatures $\sim$ 100 eV lower than the CH_2 counterparts. These low temperatures are due to the hollowing of the fast electron beam which can be seen by taking 2D plots of n_f & B_z in x-y midplane for I & II, figure 6.3. The hollowing of II, figure 6.3b, is caused by the generation of magnetic fields within the guiding structure,

figure 6.3d. Due to the resistivity of carbon being larger compared to CH_2, the confining azimuthal magnetic field will be weaker, figure 6.4c, which results in less fast electrons being confined. This, in turn, will lead to more inhomogeneities in the fast electron propagation resulting in interior magnetic fields which push fast electrons away from the center of the target - hollowing the beam. This is in stark contrast to I where negligible magnetic fields occur within the guiding structure. One possible consequence of this hollowing is that the target will only be heated to 10s eV which could lead to a possible method for the generation of WDM.

The struts used, III-IV figure 6.1d - 6.1e, have no impact on the overall temperature of the target. This could be due to the fact that the struts are too far out to really impact the temperature and tighter struts could be built to encourage stronger uniform heating.

While there is limited uniform heating in the targets, table 6.4, it can be seen that V produces the most significant regions of uniformity with Run D being the most successful. V differs from all the other cones, with an Al cone & Cu wire. The transition between Al & Cu is seen throughout figure 6.2. Both the transition and uniformity in longitudinal heating can be considered from the equation for Ohmic heating, equation 3.89 which is reprinted here for ease of the reader

$$\frac{\partial T_{b,x}}{\partial t} = \frac{\eta \mathbf{j}_{f,x}^2}{C}, \tag{6.3}$$

where T_b is the background temperature of the target.

The immediate drop between the two targets is thus due to the increase of the specific heat capacity. Regions of uniform heating, across all types of targets, arise from a uniformity in current density. This can clearly be evident in figure 6.4a which shows $\mathbf{j}_x^2$, sliced in the y-z midplane, for Run D across cones I, II & V. The reason for these extended uniformities in the current density arises from how the fast electron flow develops, which will be strongly influenced by the specific heat capacity and resistivity. Due to Copper having a larger Z & specific heat capacity, the resistivity is not only larger than Al but stays larger for longer thus resulting in larger confining magnetic fields, figures 6.4b & 6.4c. As well as this, it can be seen that the structure of the magnetic field differs from the Al case, with this extending inside the guiding structure resulting in a larger L_ϕ. From

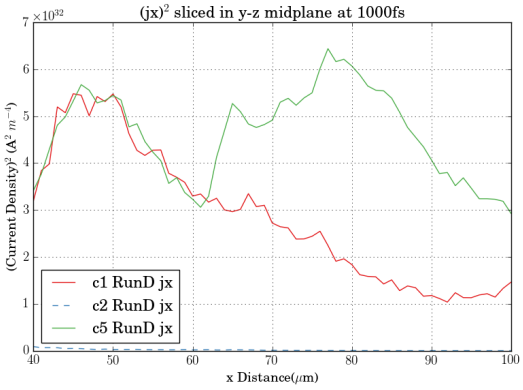

(A) $\mathbf{j}_x^2$ sliced in y-z midplane for Cones I, II & V Run D.

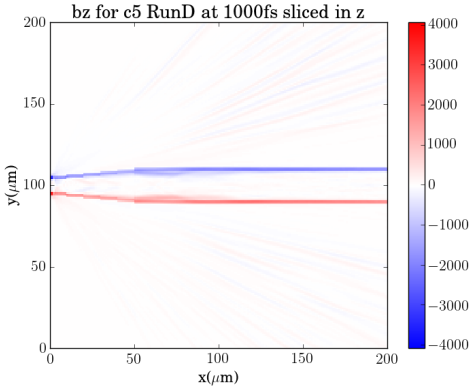

(B) B_z at y = 100 μm for Cone V.

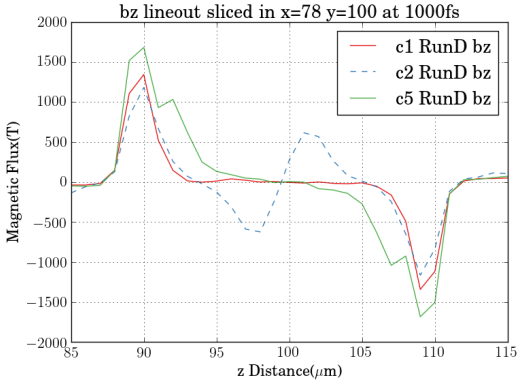

(C) B_z lineout at x = 78 μm, y = 100 μm for Cones I, II & V.

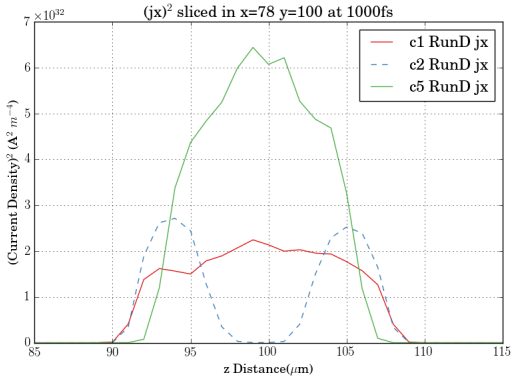

(D) Plot showing $\mathbf{j}_x^2$ sliced at x = 78 μm, y = 100 μm for Cone I, Cone II & Cone V, Run D.

FIGURE 6.4: (a) $\mathbf{j}_x^2$ sliced in y-z midplane for Cones I, II & V. (b) B_z sliced y = 100 μm for Cone V. (c) B_z lineout at x = 78 μm, y = 100 μm for Cones I, II & V. (d) $\mathbf{j}_x^2$ sliced at x = 78 μm, y = 100 μm for Cone I, II & V. All plots come from RunD.

the confinement criteria, equation 6.2, this results in more fast electrons being confined within the wire and thus larger temperatures in the guiding structure. Due to the magnetic field extending into the wire, it also acts to further collimate the fast electron beam within the wire, as seen in figure 6.4d. Furthermore, the higher current density also leads to term (a) from equation 3.92 to reinforce the collimation. This leads to higher current densities in the center of the target which may affect uniformity.

While this may give a description of why higher temperatures are seen and why uniform heating may last longer in a Cu wire, the question still remains: Why does this occur? This is considered in more detail in the following section.

6.5.2 Uniform Heating for Cone V Run D

A striking feature of $\mathbf{j}_x^2$ in figure 6.4a is that after 60 μm the Cu wire current density increases which is in stark contrast to the Al wire current density. The suggestion here is therefore that non-uniformities in the current density leads to regions of uniformity. This can be considered from the temporal evolution of $\mathbf{j}_x^2$ along the propagation axis, lineouts, and the overall magnitude of the current $\mathbf{j}^2 = \sqrt{\mathbf{j}_x^2 + \mathbf{j}_y^2 + \mathbf{j}_z^2}$ in 2D plots as shown in figures 6.5 & 6.6.

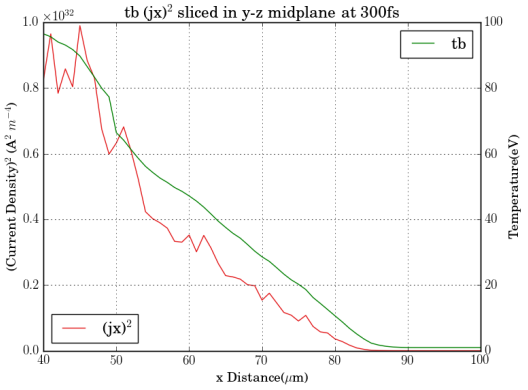

(A) Lineout for $\mathbf{j}_x^2$ & tb at 300 fs.

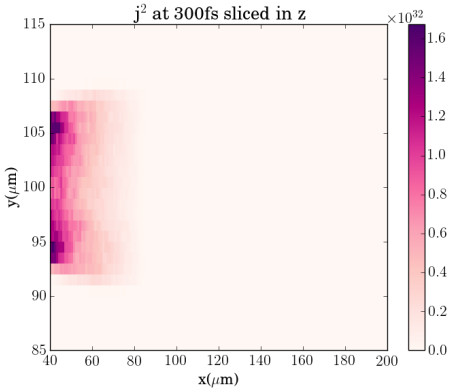

(B) $\mathbf{j}^2$ at z = 100 μm for 300 fs

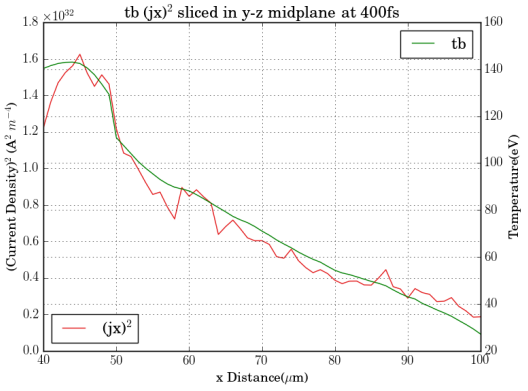

(C) Lineout for $\mathbf{j}_x^2$ & tb at 400 fs.

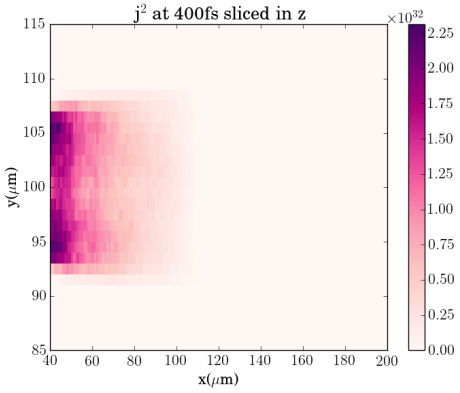

(D) $\mathbf{j}^2$ at z = 100 μm for 400 fs

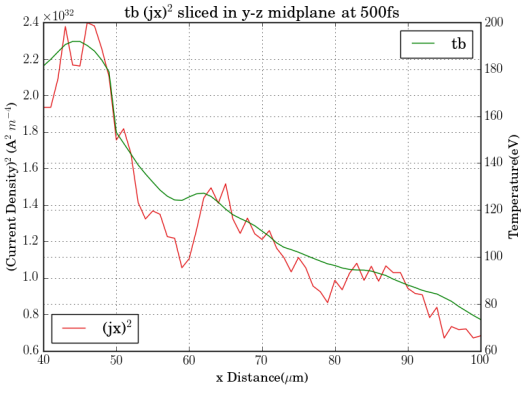

(E) Lineout for $\mathbf{j}_x^2$ & tb at 500 fs.

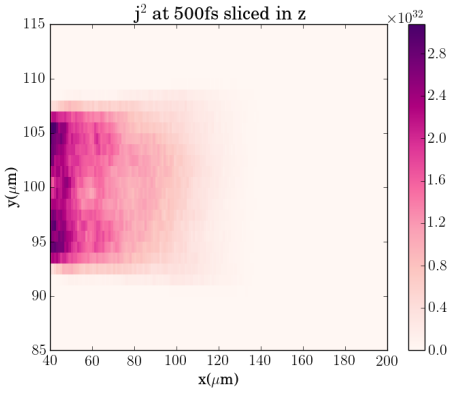

(F) $\mathbf{j}^2$ at z = 100 μm for 500 fs

FIGURE 6.5: 300 - 500 fs for (a), (c), (e): $\mathbf{j}_x^2$, red, & background temperature, tb, green, and (b), (d), (f): 2D plot of $\mathbf{j}^2$ at z = 100 μm

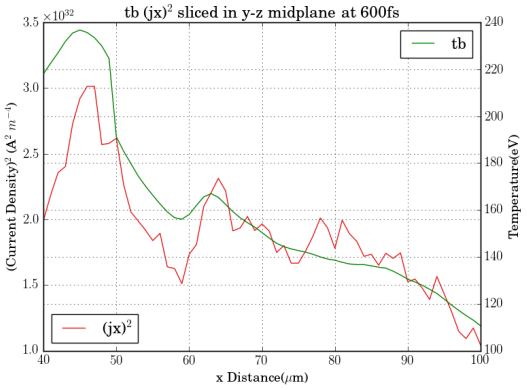

(A) Lineout for $\mathbf{j}_x^2$ & tb at 600 fs.

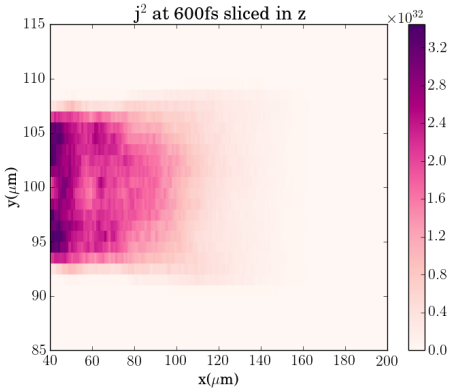

(B) $\mathbf{j}^2$ at z = 100 μm for 600 fs

(C) Lineout for $\mathbf{j}_x^2$ & tb at 700 fs.

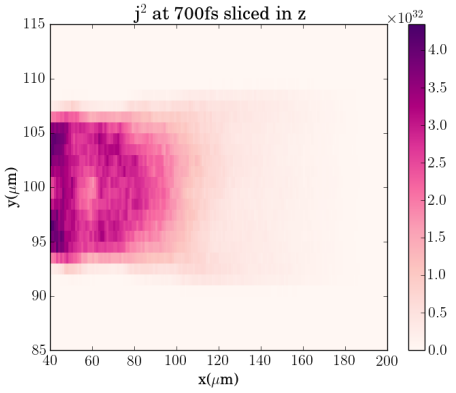

(D) $\mathbf{j}^2$ at z = 100 μm for 700 fs

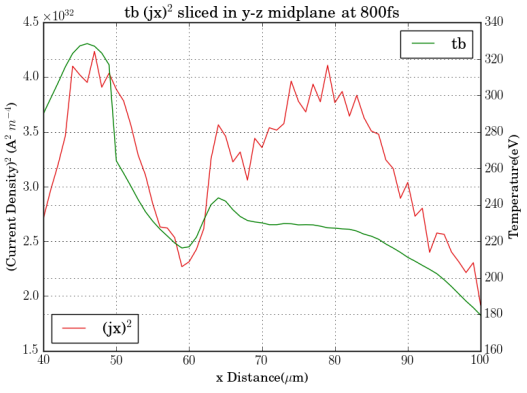

(E) Lineout for $\mathbf{j}_x^2$ & tb at 800 fs.

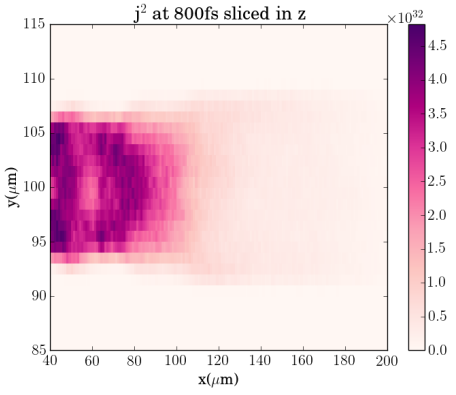

(F) $\mathbf{j}^2$ at z = 100 μm for 800 fs

FIGURE 6.6: 600 - 800 fs for (a), (c), (e): $\mathbf{j}_x^2$, red, & background temperature, tb, green, and (b), (d), (f): 2D plot of $\mathbf{j}^2$ at z = 100 μm

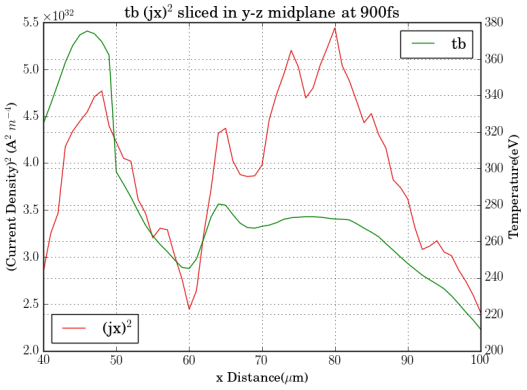

(A) Lineout for $\mathbf{j}_x^2$ & tb at 900 fs.

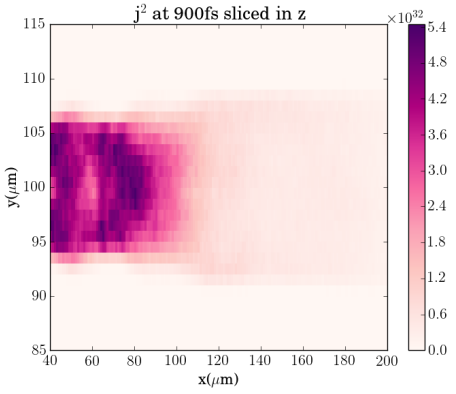

(B) $\mathbf{j}^2$ at z = 100 μm for 900 fs

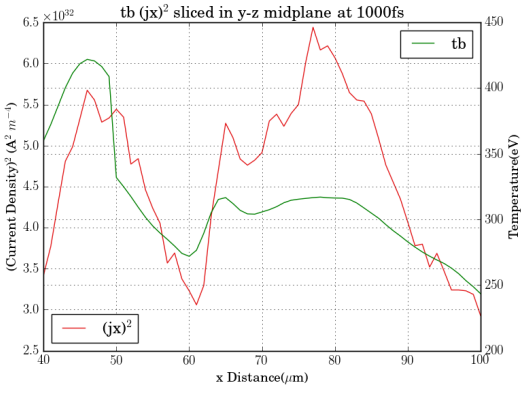

(C) Lineout for $\mathbf{j}_x^2$ & tb at 1000 fs.

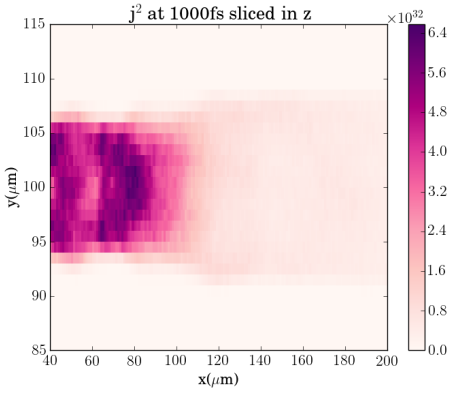

(D) $\mathbf{j}^2$ at z = 100 μm for 1000 fs

FIGURE 6.7: 700 - 1000 fs for (a) & (c): $\mathbf{j}_x^2$, red, & background temperature, tb, green, and (b) & (d): 2D plot of $\mathbf{j}^2$ at z = 100 μm

From both these figures it can be seen that there are spatial variations in the current density which grow in time. At 500 fs, figures 6.5e & 6.5f, modulations in the $\mathbf{j}_x^2$ occur at 58 μm where the beam is hollowed. At 600 fs, figure 6.6a & 6.6b, it is seen not only is this hollowing effect enhanced but that there is a collimation of the fast electron beam, with fast electrons pushed towards the target center, which leads to the peak in temperature. As the target evolves in time, these hollowing and collimating effects also grow. At 900 fs, figures 6.7a & 6.7b, it is seen that a smaller hollowing of the beam starts at 68 μm before the collimating effect occurs at 73 μm. This leads to uniform heating being induced after this collimating effect as seen in the final time step, figures 6.7c & 6.7d. Thus, regions of uniform heating occur due to inhomogeneous transport of the fast electron beam.

While the reason for this inhomogeneous transport was not considered in this thesis, it is noted that the extension of the magnetic field, figures 6.4b & 6.4c, leads to a further collimation of the beam which can possibly aid in the uniformity of the heating. Furthermore, throughout the rest of this Chapter, Cone V Run D will be the sole focus of our attention. In the following sections, the optimisation of the uniform heating from the variation in material of wire & laser parameters are considered. While this may not completely elucidate the exact reasons why this effect occurs, it will allow us to qualify what the optimum characteristics are.

6.5.3 Wire Material

With a change of material at the cone-wire interface producing favourable regions of uniform heating, a further investigation was carried out. In this approach, the material of the wire was varied with the respective materials found in table 6.6.

Target	ρ (kg m^{-3})	Density ($\times 10^{28}$ m^{-3})	Z
Au	19410	5.9	79
Li	534	4.57	3
Ti	4577	5.71	22

TABLE 6.6: Material Properties for the wire

The simulations follow the same parameters outlined in section 6.4, with the divergence angle being treated as Run D, table 6.3.

Temperature profiles in the y-z midplane for these 3 targets, which are compared to cones I & V, are presented in figure 6.8 & tabulated values of uniform heating are presented in table 6.7.

Cone	Distance (μm)	$\bar{T}$ (eV)	δT (eV)
Au	76-79	375.75	1.10
Ti	97-100	243.27	1.20

TABLE 6.7: Regions of uniform heating for various materials with T_{max} - $T_{min} \leq 2.0$

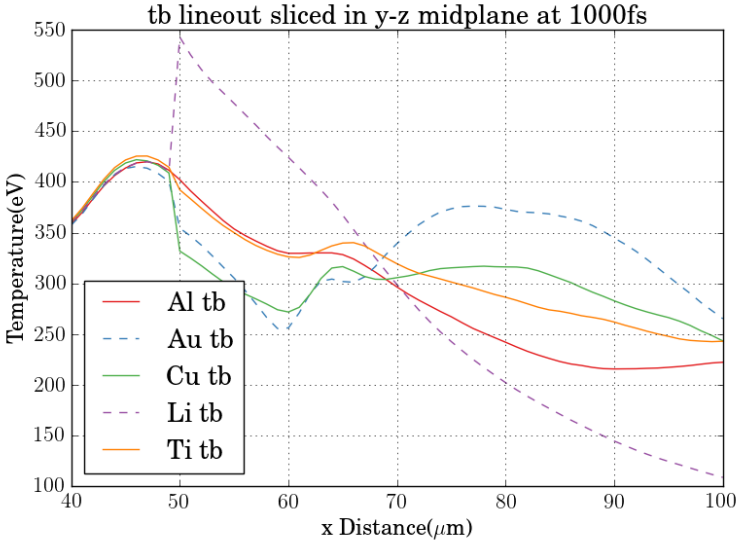

FIGURE 6.8: Temperature profile in y-z midplane for various wire materials. All simulations follow Run D parameters.

The temperature profiles presented in figure 6.8 build upon the argument presented in the previous sections. Due to Li having a smaller specific heat capacity, it results in a rapid heating of the wire immediately after the material interface. This rapid heating, combined with the smaller resistivity due to a smaller Z, leads to the smallest resistivity across the various materials. This results in a weaker magnetic field and allows for more fast electrons to leave the guide wire. For targets with a higher Z than Al, such as Ti, Cu & Au, there is the characteristic drop in temperature once the fast electrons move between the cone and wire before all of the targets produce temperatures larger compared to the Al wire, with the reasons for this being discussed in the preceding sections. However, while all 3 of these materials produce temperatures larger than Al, it is noted that the temperature profile within the wire differ substantially. The lowest Z of these 3 targets, Ti, results in a temperature profile closer to Al with a continual decrease in temperature while Cu sees a plateau in temperature and Au sees an increase in temperature. This can once again be considered from the current density and magnetic field profiles as presented in figure 6.9.

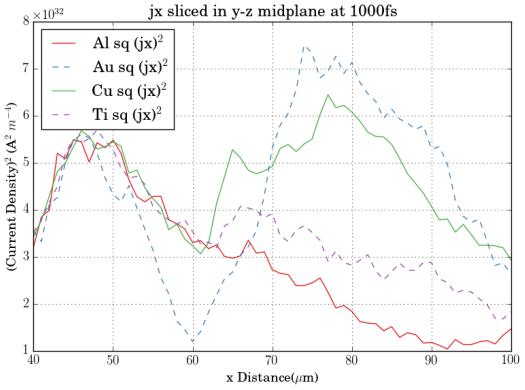

(A) $\mathbf{j}_x^2$ for Al, Au, Cu & Ti

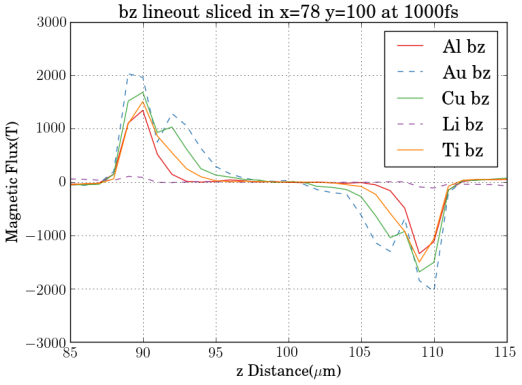

(B) B_z at x = 78 μm, y = 100 μm for materials.

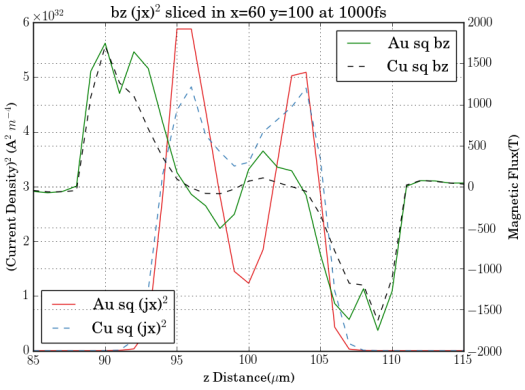

(C) B_z(red & blue lines) & $\mathbf{j}_x^2$(green and black lines) at x = 78 μm, y = 100 μm for Au(solid line) & Cu(dashed line).

FIGURE 6.9: (a) $\mathbf{j}_x^2$ sliced in y-z midplane for Au & Cu, (b) B_z lineout at x = 78 μm, y = 100 μm for Cones I, V & materials discussed in table 6.2, (c) B_z lineout at x = 60 μm, y = 100 μm for Au & Cu.

Figure 6.9a explains why no uniform heating is experienced in Ti. Here it can be noted that $\mathbf{j}_x^2$ follows a similar profile to Al, with a continuous decrease in the current density. As it was noted in section 6.5.2 uniform heating occurs due to spatial modulations in the current density and thus no uniform heating is found in Ti. This is in contrast to Au where the largest density modulations occur. This is due to the large size of the collimating and hollowing fields found within Au as seen in figures 6.9b & 6.9c respectively. While the collimating field will result in larger temperatures compared to Cu, at 75-85 μm, the hollowing field is far larger leading to a rapid reduction of the current density. These larger variations in the current density therefore prevent uniform heating from occurring.

These results therefore suggest that there is an optimum Z value for uniform heating, around the Cu value, for which the fields are large enough to collimate

the fast electron beam but not large enough to generate large interior magnetic fields which result in a larger hollowing of the beam.

6.5.4 Optimum Parameters

Throughout the above discussion all laser parameters were kept constant. Thus, a question which arises from this is what happens to the regions of uniform heating when the confinement condition is increased or decreased. To consider this a variety of runs were performed, with these being found in table 6.8.

Run	I_L ($\times 10^{19}$ Wcm^{-2})	λ (μm)	τ_L (ps)	$I_L \cdot \tau_L$	Fast e- Temp (MeV)
1	5	1	1	5×10^{19}	2.61
2	2.5		2		1.72
3	7.5		0.666		3.29
4	5	0.5	1		1.11
5		2			5.66

TABLE 6.8: Variation in parameters.

Once again temperature profiles in the y-z midplane for these runs are presented in figure 6.10 & tabulated values of uniform heating are presented in table 6.9.

Run	Distance (μm)	$\bar{T}$ (eV)	δT (eV)
2	66-71	574.03	1.60
3	59-61	169.63	1.90
4	61-63	347.73	1.90
	66-69	353.05	1.50
5	53-59	114.76	1.40

TABLE 6.9: Regions of uniform heating for runs with T_{max} - $T_{min} \leq 2.0$

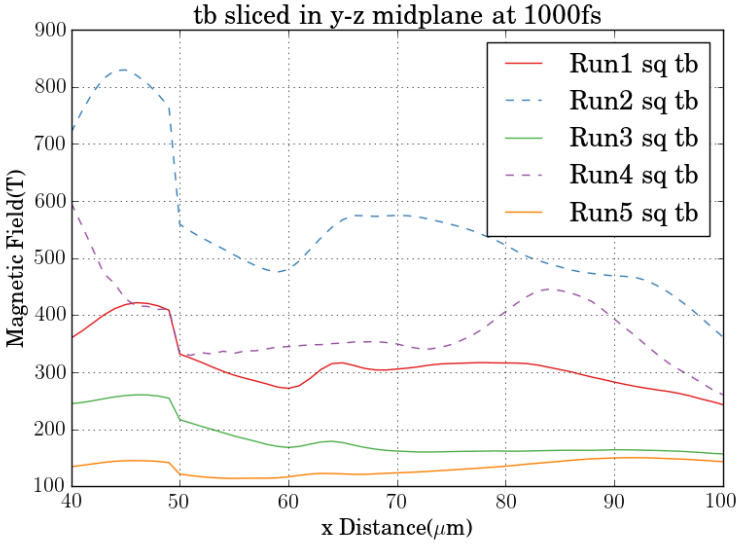

FIGURE 6.10: Temperature profile in y-z midplane for various laser parameters. Run D divergence angle used.

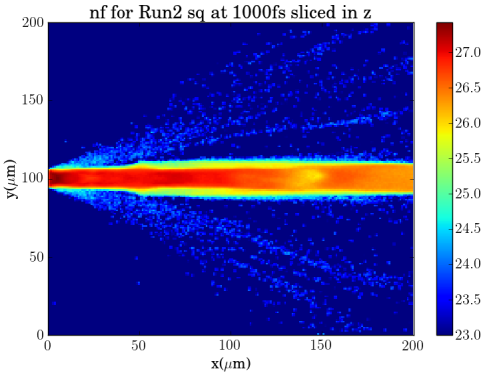

(A) $\log_{10}$ plot of fast electron density sliced at z = 100 μm for Run 2, decreased I_L.

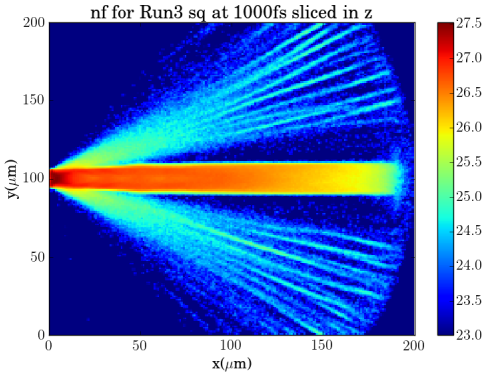

(B) $\log_{10}$ plot of fast electron density sliced at z = 100 μm for Run 3, increased I_L.

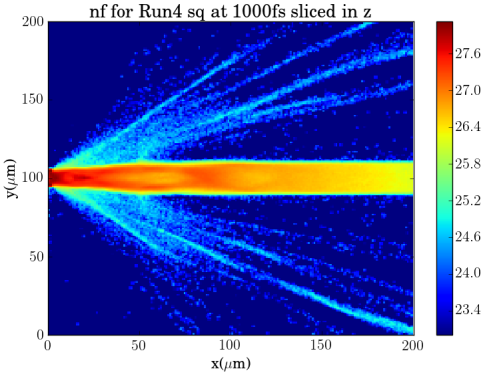

(C) $\log_{10}$ plot of fast electron density sliced at z = 100 μm for Run 4, decreased λ_L.

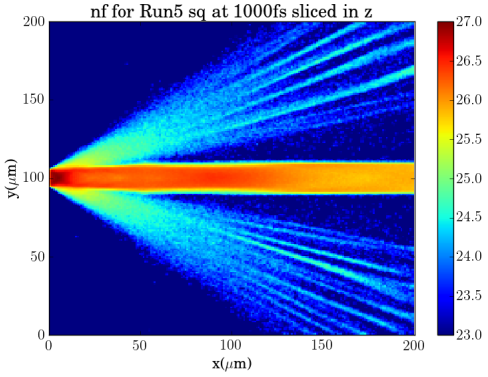

(D) $\log_{10}$ plot of fast electron density sliced at z = 100 μm for Run 5, increased λ_L.

FIGURE 6.11: $\log_{10}$ plot of fast electron density sliced at z = 100 μm for (a) Run 2, (b) Run 3, (c) Run 4 & (d) Run 5.

The reasons for the higher temperatures in runs 2 & 4 can be considered from equations 4.5 & 6.2 [98]. A reduction in λ_L will result in a reduction of the ponderomotive energy, equation 2.64, which results in a higher current density, equation 4.5. This higher current density will lead to larger magnetic fields, equation 3.92, and thus a larger left hand side for equation 6.2, leading to more fast electrons being confined. For the intensity variation, while a decrease in intensity will result in a lower current density this is offset by a lower velocity of the fast electrons, resulting in a smaller right side for equation 6.2 and thus more fast electrons confined. The inverse of this explains why a reduction in the confinement is also observed. These phenomenon can be seen in figure 6.11.

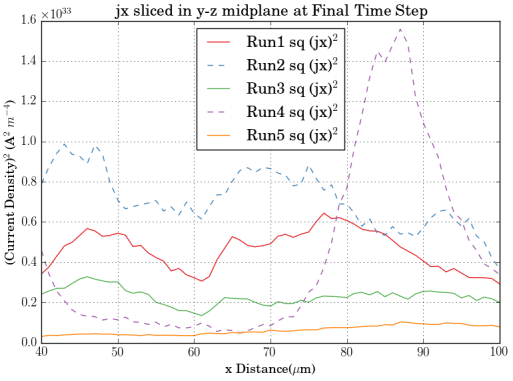

(A) (a) $\mathbf{j}_x^2$ sliced in y-z midplane for Runs 1-5.

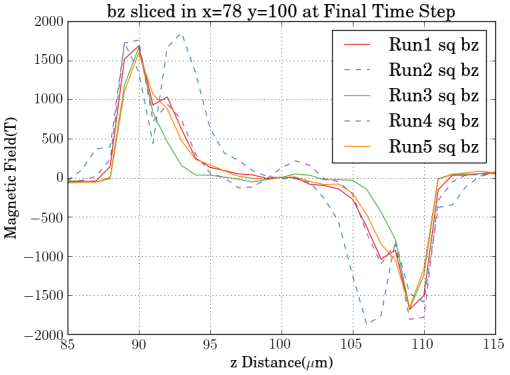

(B) B_z sliced at x = 78 μm and y = 100 μm for Runs 1-5.

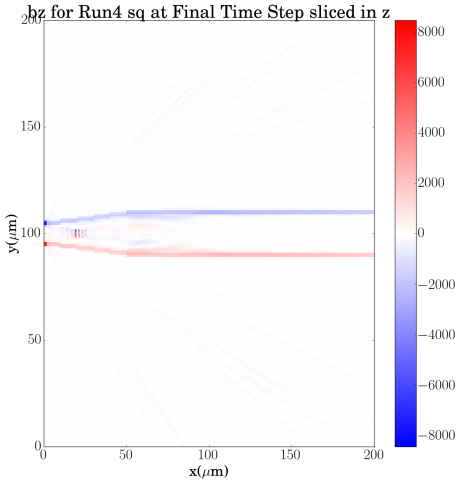

(C) B_z sliced at z = 100μm for Run 4.

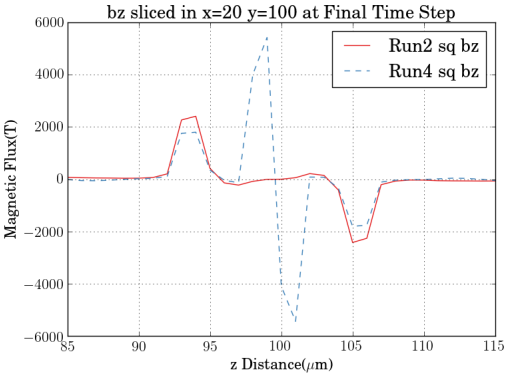

(D) B_z lineout at x = 20 μm, y = 100 μm for Runs 2 & 4

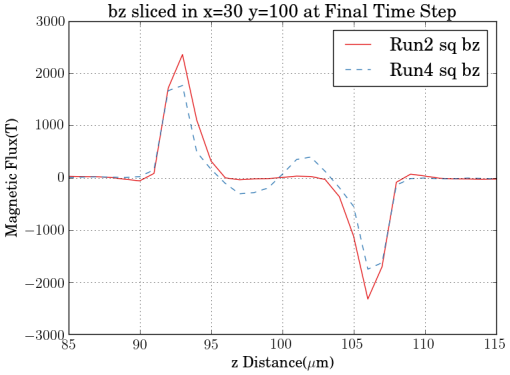

(E) B_z lineout at x = 30 μm, y = 100 μm for Runs 2 & 4

FIGURE 6.12: (a) $\mathbf{j}_x^2$ sliced in y-z midplane for Runs 1-5. (b) B_z sliced at x = 78 μm and y = 100 μm for Runs 1-5. (c) B_z sliced in x-y midplane for Run 4. (d) B_z lineout at x = 20 μm, y = 100 μm for Runs 2 & 4. (e) B_z lineout at x = 30 μm, y = 100 μm for Runs 2 & 4.

With regards to uniform heating from these runs, it can be seen that the variation results in differing results. When varying I_L it is noted that the $\mathbf{j}_x^2$ profile, figure 6.12a, follow very similar patterns: an increase in density, before a trough and followed by another increase in density. However the differences come in the relative amplitudes sizes of these variations. An increases in I_L, i.e. a decrease in the confinement parameter, therefore results in an overall smaller current density and thus a smaller increases in density and no uniform heating due to the smaller density modulations. While the decrease in I_L, an increase in the confinement parameter, therefore results in larger density modulations compared to Run 1, it does still result in uniform heating which occur at a similar position to Run 1. In comparison, varying λ_L results in disparate heating profiles due to the large variation in $\mathbf{j}_f$. The increase in λ_L, resulting in a decrease in both $\mathbf{j}_f$ and the confinement parameter, results in the characteristic hollowing and collimation being dramatically reduced. This does however result in a small region of uniform heating which occurs far sooner, at around 53-59 μm depth, than in any other result. The decrease in λ_L, resulting in an increase in both $\mathbf{j}_f$ and the confinement parameter, leads to the generation of large magnetic fields within the guiding structure, as seen in figure 6.12c. This leads to an even more inhomogeneous transport of the fast electron beam which undergoes rapid hollowing and collimation in the wire as seen in figures 6.12d & 6.12e preventing uniform heating.

6.5.5 The Role of β in uniform heating

In the previous section, it was shown that a variation in current density leads to differing periods of uniform heating. Another parameter which impacts the current density is the laser fast electron conversion efficiency β, equation 3.78, which was kept at 0.3 throughout all simulations. Thus, a question which arises is: does this period of uniform heating occurs only at $\beta = 0.3$ or if it is independent of β? To consider this, β was both increased and decreased with the runs found in table 6.10.

Run	I_L ($\times 10^{19}$ Wcm^{-2})	λ (μm)	τ_L (ps)	β	Fast e- Temp (MeV)
$\beta_{0.3}$	5	1	1	0.3	2.61
$\beta_{0.2}$				0.2	
$\beta_{0.4}$				0.4	

TABLE 6.10: Runs used for varying β.

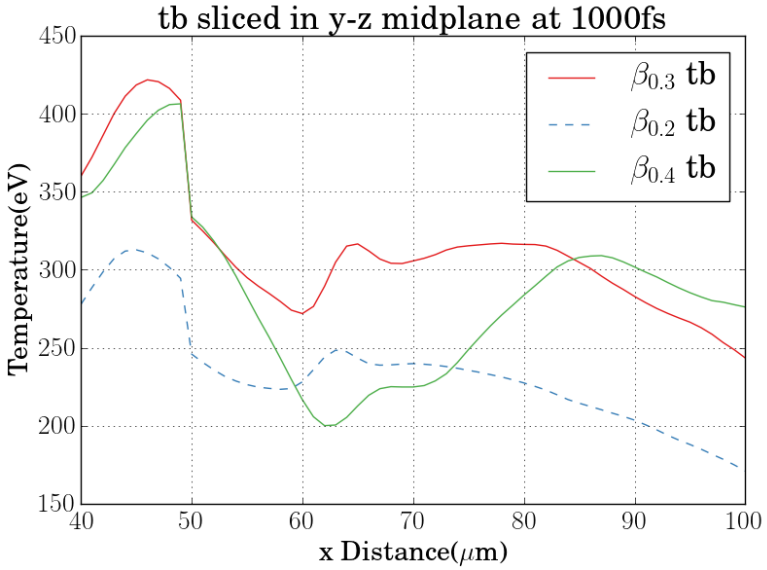

FIGURE 6.13: Temperature profile in y-z midplane for various laser parameters. Run D divergence angle used.

Temperature profiles in the y-z midplane for these respective runs can be found in figure 6.13 and the tabulated forms of uniform heating are presented in table 6.11.

Run	Distance (μm)	$\bar{T}$ (eV)	δT (eV)
$\beta_{0.3}$	68-70	304.67	1.70
	75-82	316.15	1.80
$\beta_{0.2}$	56-59	223.93	1.40
	66-73	238.80	1.90
$\beta_{0.4}$	67-71	224.80	2.00
	85-88	308.53	1.40

TABLE 6.11: Regions of uniform heating for β variation, with T_{max} - $T_{min} \leq$ 2.0. $\beta_{0.3}$ has been added for convenience of the reader.

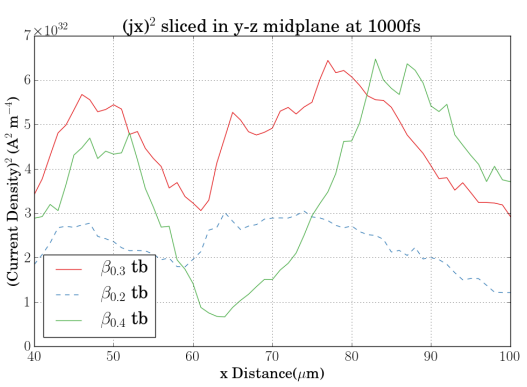

(A) j_x^2 sliced in the midplane for the 3β values.

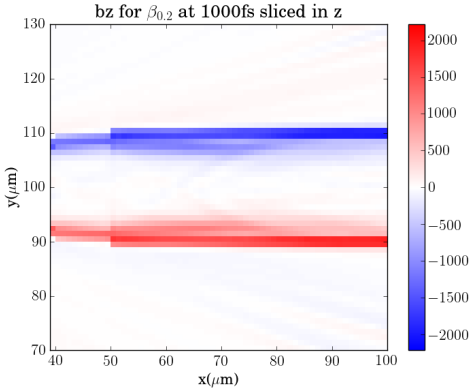

(B) B_z sliced at z = 100μm for $\beta = 0.2$ between x = 40 - 100 μm & y = 70 - 130 μm

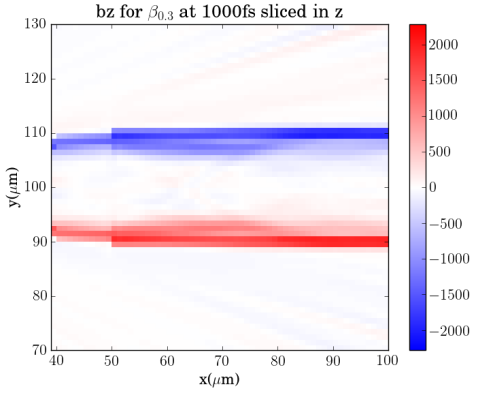

(C) B_z sliced at z = 100μm for $\beta = 0.3$ between x = 40 - 100 μm & y = 70 - 130 μm

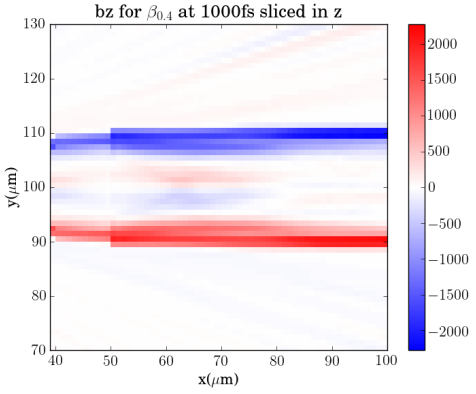

(D) B_z sliced at z = 100μm for $\beta = 0.4$ between x = 40 - 100 μm & y = 70 - 130 μm

FIGURE 6.14: Figure showing a) j_x^2 in the midplane for the 3 β values, (b)-(d) B_z sliced at z = 100 μm for $\beta = 0.4$ between x = 40 - 100 μm & y = 70 - 130 μm for b) $\beta = 0.2$, c) $\beta = 0.3$, d) $\beta = 0.4$.

The results from both figure 6.13 and table 6.11 show that the periods of uniform heating are independent of the β value, with the temperature profiles sharing the same characteristic traits as discussed in section 6.5.2. All runs also experience two periods of uniform heating, with all runs sharing one at a minimum distance of 68-70 μm. The other period of uniform heating is dependent upon the value of β, with larger values occurring deeper into the target. This can be considered from the $\mathbf{j}_x^2$ plot, figure 6.14a. The larger current density results in larger interior magnetic fields, figure 6.14d, which result in larger periods of inhomogenous transport. Due to the uniform heating occurs after this period of inhomogeneous transport, section 6.5.2, the uniform heating will occur deeper in the target for $\beta_{0.4}$ and at a shallower depth for $\beta_{0.2}$.

6.5.6 Varying Conical Geometry

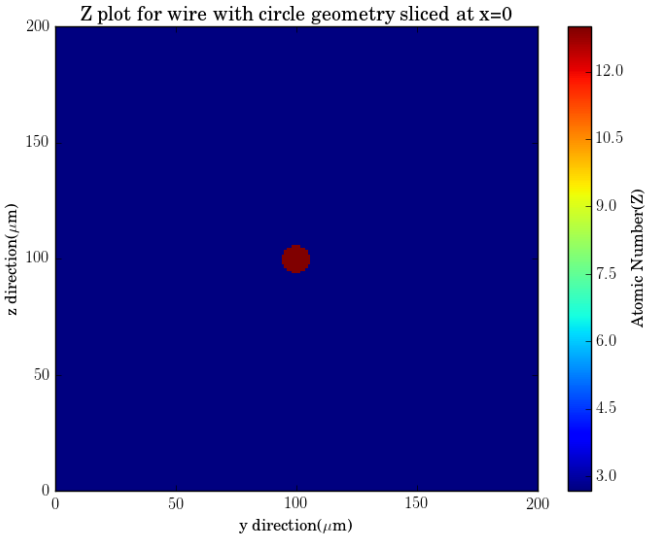

FIGURE 6.15: Atomic Number (Z) at x = 0 for Cone V with a cylindrical geometry

As it was noted in section 6.3, the geometry assumed in the above results follows a "square" geometry, figure 6.1. While the geometry of the guide wire can be any, as long as there is a perpendicular resistivity gradient to the propagation of fast electrons (see figure 3.6 [101, 105, 144]), the most commonly used geometry is that of a cylindrical wire [4, 98, 102, 103]. A question which therefore arises is how does the cylindrical geometry compare to the "square" used in this chapter. To perform this comparison, some care must be taken as the area of the square is given by l^2, where l is the side of a square, while the area of circle is given by πr^2 thus meaning a direct comparison will be of little use. However if we consider our "circle" wire with $r = \sqrt{\frac{A_s}{\pi}}$, where A_s is the area of the square at that expansion, it allows for a fair comparison between the two geometries. It must be noted however that there is a caveat with this approach. As it was previously discussed in section 6.4, the grid size is taken to be 200^3 grid with a spacing of 1 μm in all directions. This means that the areas will not be exact but as shown in table 6.12, all values are within a 12% range therefore allowing for a reasonable comparison.

	Square	Circle	Circle Sim	% Difference
Start				
Length (l) or Radius (r) (μm)	10 (l)	5.64 (r)	6 (r)	
Area (μm^2)	100	100	113.10	11.6
Exp 1				
Length (l) or Radius (r) (μm)	12 (l)	6.77 (r)	7 (r)	
Area (μm^2)	144	144	153.94	6.0
Exp 2				
Length (l) or Radius (r) (μm)	14 (l)	7.90 (r)	8 (r)	
Area (μm^2)	196	196	201.06	2.6
Exp 3				
Length (l) or Radius (r) (μm)	16 (l)	9.03 (r)	9 (r)	
Area (μm^2)	256	256	254.47	0.6
Exp 4				
Length (l) or Radius (r) (μm)	18 (l)	10.16 (r)	10 (r)	
Area (μm^2)	324	324	314.16	3.0
Wire				
Length (l) or Radius (r) (μm)	20 (l)	11.28 (r)	11 (r)	
Area (μm^2)	400	400	380.13	5.0

TABLE 6.12: Runs used for "circle" wire so that its area would match "square". Circle Sim denotes the value used in ZEPHYROS.

To kept consistency between the two targets, it is assumed that $r_{laser} = r_{cone}$ meaning that r_{laser} is taken to be 6 μm, compared to the 5 μm for the Square. All other parameters follow Cone V Run D.

Temperature profiles in the y-z midplane for these respective runs can be found in figure 6.16 and the tabulated forms of uniform heating are presented in table 6.13.

Run	Distance (μm)	$\bar{T}$ (eV)	δT (eV)
Square	68-70	304.67	1.70
	75-82	316.15	1.80
Circle	74-81	261.08	1.40

TABLE 6.13: Regions of uniform heating for the two geometries, with T_{max} - $T_{min} \leq 2.0$. Square has been added for convenience of the reader.

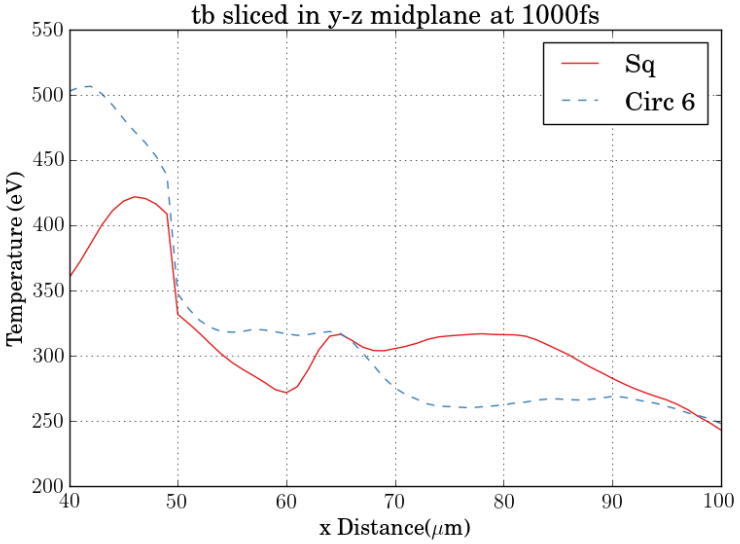

FIGURE 6.16: Temperature profile in y-z midplane for targets described in table 6.12

Figure 6.16 & table 6.13 show that the uniform heating generated inside the wire is independent of geometry, with both targets producing uniform heating in the region of 75 - 81 μm. However, it is also clear to see that the two geometries produce contrasting heating profiles, with "circle" producing a relatively stable profile with lower temperatures while the "square" target produces inhomogeneous transport with higher temperatures. Thus, the geometries play a crucial role in defining the periods of uniform heating. To consider the reasons for this in more detail, we take both $\mathbf{j}_x$ and B_z profiles as presented in figure 6.17.

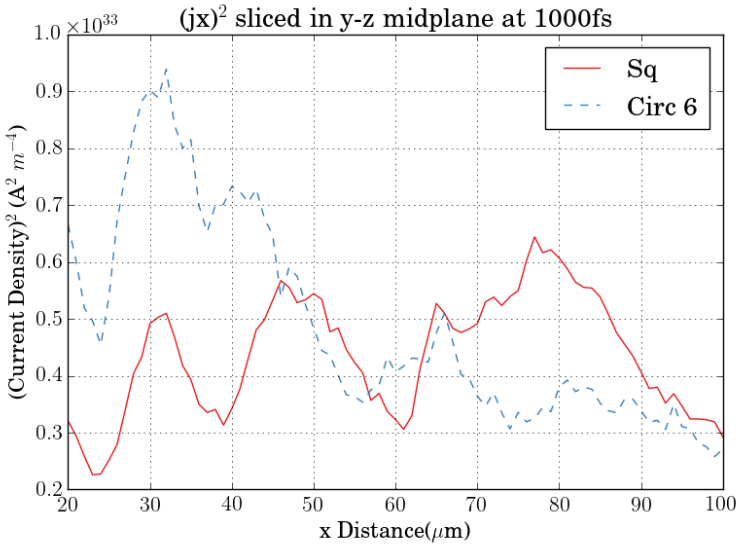

(A) Lineout for $\mathbf{j}_x^2$ in y-z midplane at 1000 fs for Square and Circle.

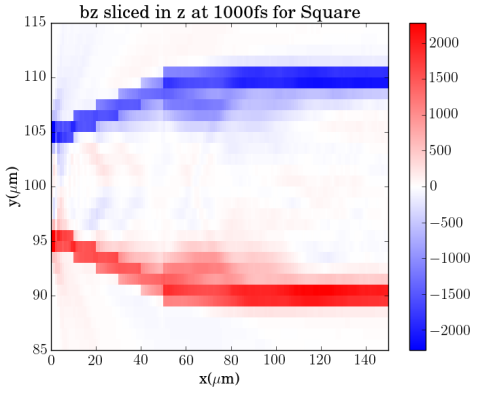

(B) 2D plot for B_z sliced in z for Square at 1000 fs

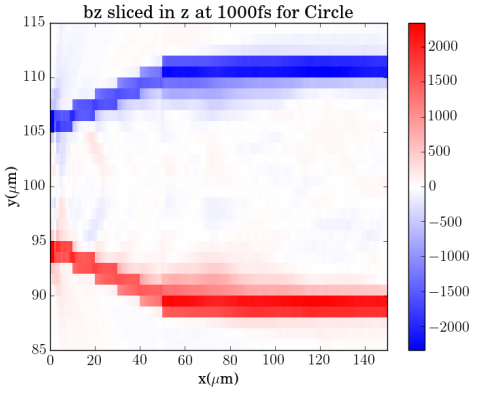

(C) 2D plot for B_z sliced in z for Circle at 1000 fs

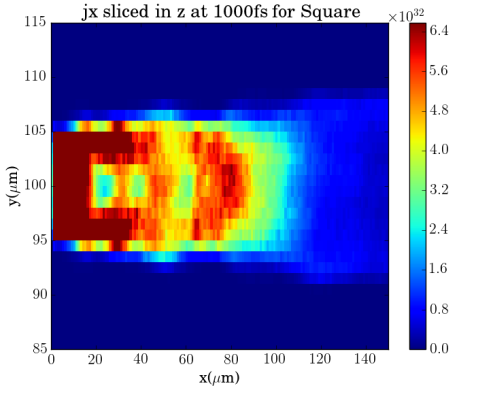

(D) 2D plot for $\mathbf{j}_x^2$ sliced in z for Square at 1000 fs

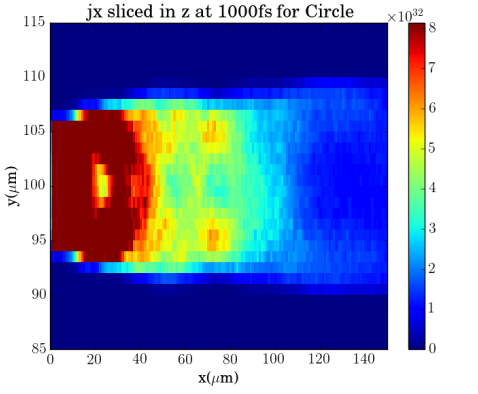

(E) 2D plot for $\mathbf{j}_x^2$ sliced in z for Circle at 1000 fs

FIGURE 6.17: Plots showing Square and Circle at 1000 fs: a) $\mathbf{j}_x^2$ in y-z midplane, b) - c): 2D plot for $\mathbf{j}_x^2$ sliced in z for Square and Circle respectively, d) - e): 2D plot for b_z sliced in z for Square and Circle respectively

Figure 6.17a clearly shows the distinct transport patterns in the two geometries. Unlike the "square" target which experiences inhomogeneous transport with periods of hollowing followed by collimation in the center of the wire, as discussed in section 6.5.2, the "circle" target follows far more of a step profile with smaller periods of increasing current density. These effects can be considered from the interior magnetic fields presented in figures 6.17b & 6.17c. As it can be seen in both the cone, 22 μm & 32 μm, and the wire, where the collimating magnetic field extends into the target, the interior magnetic field is weaker in the "circle" target. This is due to the fast electron beam having a larger radius, starting at 6 μm vs 5 μm for "square", therefore leading to a weaker field generation, equation 3.91. These weaker fields means that the fast electron beam will experience far less pull or push from the center of the target, leading to a far more uniform profile compared to "square".

From our definition of uniform heating, periods of uniform heating which are distinguishable section 6.5.1, it would be suggested that "square" is superior to the "circle" wire due to not only having two periods of uniform heating but also that both periods of uniform heating being considerably different from the rest of the temperatures. However, it must be noted that this conclusion is only relevant to wires with this area and other area combinations may produce differing results.

6.6 Conclusion

In this chapter, the generation of uniform heating, which could be used in an experimental setting, was investigated from a variety of inverse conical taper designs with a "square" geometry. It was found that the strongest regions of uniform heating, and highest temperatures, are produced from a material transition between an Al "cone", a truncated inverse pyramid in this geometry, & Cu wire. The higher temperatures are due to the Cu wire having a large resistivity & specific heat capacity, which causes for the resistivity to decrease at a slower rate and thus results in stronger confining magnetic fields. Furthermore, these fields are found to extend into the wire, further collimating the fast electron beam. The uniform heating arises from spatial modifications in the transport of the fast electron beam. The exact reasons for this were not fully elucidated but a variety of further investigations were carried out to further the investigation of this phenomenon. Further

work investigated the impact on uniformity of heating by varying the wire material. Lower Z wires resulted in limited spatial modulations of the fast electron beam and therefore weak production of quasi-uniform heating regions. While the higher Z targets produced even larger and wider magnetic fields, and thus higher temperatures, the spatial modifications in the transport are larger resulting in lack of uniform heating. Work also considered increasing and decreasing of the confinement parameter via either I_L or λ_L respectively. Both sets of results showed that the variation in current density impacted the overall uniformity of heating with this being dependent upon the parameter. Increasing I_L, which decreases the confinement parameter, resulted in a reduction of the density modulations therefore resulting in a weak production of uniform heating. While decreasing I_L, which increases the confinement parameter, resulted in larger density modifications and a resultant region of uniform heating was generated. On the other other, the variation in λ_L caused a completely different transport patterns due to the large modification of the current density. Increasing λ_L, which reduced current density, leads to a large reduction in the modulations in the current but a region of uniform heating are found just after the material interface. A decreased λ_L, an increased current density, produces no uniform heating at all due to the large interior fields generated within the wire. Investigations were also carried out to see if the uniform heating was dependent upon the value of the fast electron conversion efficiency, β. Results showed that while the production of uniform heating is independent of β, the depths at which it occurs are changed with a higher β pushing the uniform heating deeper into the target due to the larger current density. Finally a cylindrical geometry was compared to a "square" wire with the same area. It was found that while uniform heating is independent in both wires, the transport patterns are strongly dependent upon the geometry, with the cylindrical geometry being found to have far weaker interior magnetic fields due a wider fast electron beam and thus leading to a more stable pattern.

Chapter 7

Conclusions and Future Work

7.1 Summary and Conclusions

In this thesis numerical investigations for Ohmic heating in plain, Chapters 4 - 5, and resistive structured targets, Chapter 6, were investigated. Each of these Chapters will be described in more detail below.

In Chapter 4, simple analytical scalings for Ohmic heating were derived based on either the Spitzer resistivity or a prescriptive low temperature resistivity. Results from 3D PIC-hybrid simulations show that the scalings with various laser-target parameters, I_L, λ_L & n_i, is underestimated via the Spitzer resistivity while being more accurately represented by the prescriptive low temperature resistivity. These results show that the low temperature regime has a crucial role in the temporal evolution of the target.

In Chapter 5 assumptions from the prescriptive low temperature resistivity model of constant ionisation and specific heat capacity were investigated via a 0D Ohmic heating model. Results from the model showed that the assumption of constant Z^* & specific heat capacity is an adequate assumption. It was noted from the heating model that fixing both Z^* & specific heat capacity results in higher temperatures compared to the run with variable parameters. This argument was expanded by both using a full resistivity model and varying Z^* and specific heat capacity independently. Results from this further investigation show that fixing the specific heat capacity results in higher temperatures than fixing Z^*. The results from the

specific heat capacity thus suggest that there is a temperature dependence on the specific capacity. This is in stark contrast to the ideal gas heat capacity which is used in the derivation of the scaling relations which suggest that there is no temperature dependency at all. Thus, the selection of an ideal gas heat capacity is not adequate due its neglection of this temperature dependence.

In Chapter 6 the production of uniform heating for use in the generation of HDM was investigated via a variety of designs using the inverse conical taper. For targets with a square geometry, a 2 material approach of an Al "cone", a truncated inverse pyramid in this geometry, & Cu wire, were found to exhibit the strongest regions of uniform heating and highest temperatures compared to a pure Al structure. The resultant higher temperatures are due to both a larger resistivity and specific heat capacity which leads to stronger confining magnetic fields. Moreover, the magnetic fields are not only larger but are also found to further extend into the wire, leading to further collimation of the beam therefore resulting in overall higher temperatures in the Cu wire. Uniform heating was due to the inhomogeneous transport of the fast electron beam in wire. This was in stark contrast to Al which had a monotonically decreasing current density, leading to no uniform heating. While this effect was not fully explored in this work, investigations were carried out to consider the various ways to optimise this uniform heating. First, the material of the wire with Z values smaller and larger than Cu. Results showed that decreasing the Z lead to no inhomogeneities in the transport and thus no uniform heating is found. Increasing Z leads to larger temperatures due to the larger magnetic fields. However, the fast electron beam was found to have even larger non-uniformities which lead to no uniform heating within the wire. Secondly, the confinement parameter was also considered with it being increased & decreased by varying either I_L or λ_L. These two variables had dramatically different results. The variation of λ_L leads to large a variation in the fast electron current density and thus very different transport patterns. Decreasing λ_L, increased confinement parameter, results in a far larger current density, leading to large magnetic fields generated in the wire therefore increase the inhomogeneities in the transport and thus no uniform heating. Increasing λ_L, decreased confinement parameter, results in a far smaller current density and results in limited inhomogeneities of the transport beam but uniform heating region is found within the wire. The variation in I_L produced similar transport patterns to the original Cu Wire. Decreasing I_L, increased confinement parameter, results in a larger current density and thus larger

inhomogeneities, smaller compared to I_L variation, with a uniform heating region occurring within the wire. Increasing I_L, decreased confinement parameter, results in a smaller current density and thus smaller inhomogeneities, therefore resulting in the suppression of uniform heating occurring within the wire. Work then went on to consider if uniform heating was dependent upon the fast electron conversion efficiency, β. Results showed that uniform heating was produced in all runs, with the β value determining where the periods of uniform heating would occur. Finally, the role of geometry was considered by also construction the cone & wire in cylindrical geometry which had roughly the same area as the "square" approach. Results found that uniform heating was produced in both wires but the transport of the fast electron beam varied greatly. The variation was itself generated due to the cylindrical approach having a larger radius, leading to lower field generation and thus meaning that the fast electron beam followed a more uniform transport pattern.

7.2 Future Work

In this section, some outlines for future work are considered.

The investigation into simple analytical scalings showed that exponents from the low temperature resistivity model better fits the numerical results. Future work from this would be to consider experimental evidence which corroborates these numerical findings. If an experimental approach was to be undertaken, there are considerations which need to be made. Due to ZEPHYROS assuming an ideal scenario, with fast electrons injected through a dump into the target, no considerations were made with regards to the laser pulse and absorption mechanisms occurring within an experiment. Due to this, any experimental run will need to consider either pulse cleaning techniques or the use of structured targets, as discussed in section 3.6, will need to be employed to fully characterise the nature of the pulse. For a characterisation of temperatures at various depth, as was done in Chapter 4, a layered target of the required material and other transport layers is recommended, section 3.6, so that the diagnostics can distinguish between Kα emissions at different depths. Some of the variations investigated, e.g. a variation of the wavelength down to the 4th harmonic, may not be achievable in the experimental setting but variation of parameters such as I_L and n_i, e.g. by comparing

foam targets to solids, should be considered.

With regards to the inverse conical design, there are a variety of avenues this work can be taken along. Work should be undertaken to fully elucidate the reason for the emergence of regions of uniform heating. Further work will also need to consider the two geometries and carry out further investigations to fully elucidate the reasons for the differences in both geometries. Following this, work could also look at using a cladding suggested by Alraddadi et al (2016, 2018) [102, 103]. This would result in a target where the guide wire was cladded with a lower Z material, and graded until a certain Z, i.e. the substrate. This cladding, as discussed in section 3.4.3.2 results in a reduction of the interior magnetic fields. This could result in either uniform heating over larger scales in a variety materials higher than Cu or it could also help elucidate the role of the interior magnetic fields in the role of uniform heating.

Appendix A

Thomas-Fermi Analytic Formulas

A.1 Thomas-Fermi Analytic Formulas

T = 0, any density	
$\rho_1 = \rho/(AZ)$	ρ in g/cm^3
$x = \alpha\ (\rho\ /(ZA))^{\beta}$	$\alpha = 14.3139$
$Z^* = Zx/(1 + x + \sqrt{1+2x})$	$\beta = 0.6624$
Any temperature and density	
$\rho_1 = \rho/(AZ)$	
$T_1 = T\ /\ Z^{\frac{4}{3}}$	$a_1 = 0.003323$
$T_f = T_1/(1 + T_1)$	$a_2 = 0.9718$
$A = a_1 T_1^{a_2} + a_3 T_1^{a_4}$	$a_3 = 9.26148\times10^{-5}$
$B = -\exp(b_0 + b_1 T_f + b_2 T_f^7)$	$a_4 = 3.10165$
$C = c_1\ T_f + c_2$	$b_0 = -1.7630$
$Q_1 = A\ \rho_1^{\beta}$	$b_1 = 1.43175$
$Q = (\rho_1^C + Q_1^C)^{\frac{1}{C}}$	$b_2 = 0.31546$
$x = \alpha\ Q^{\beta}$	$c_1 = -0.366667$
$Z^* = Zx/(1 + x + \sqrt{1+2x})$	$c_2 = 0.983333$

TABLE A.1: Analytic Formulas for ionisation degree Z*. T is taken in units of eV. Model reproduced from Atzeni (2004) [18]

Bibliography

[1] T H Maiman. Stimulated optical radiation in Ruby. *Nature*, 187(4736): 493–494, 1960. ISSN 00280836. doi: 10.1038/187493a0. URL http://www.nature.com.ezp-prod1.hul.harvard.edu/nature/journal/v187/n4736/abs/187493a0.html{%}5Cnhttp://www.nature.com.ezp-prod1.hul.harvard.edu/nature/journal/v187/n4736/pdf/187493a0.pdf.

[2] D Strickland and G A Mourou. Compression of Amplified Chirped Optical Pulses. *Optics Communications*, 56(3):219–221, 1985. doi: https://doi.org/10.1016/0030-4018(85)90120-8.

[3] A R Bell, A P L Robinson, M Sherlock, R J Kingham, and W Rozmus. Fast electron transport in laser-produced plasmas and the KALOS code for solution of the Vlasov-Fokker-Planck equation. *Plasma Physics and Controlled Fusion*, 48(3):R37———R57, 2006. ISSN 07413335. doi: 10.1088/0741-3335/48/3/R01. URL http://stacks.iop.org/0741-3335/48/i=3/a=R01?key=crossref.ab0ba53f8162ac23b354c6b27212081c.

[4] A P L Robinson, D J Strozzi, J R Davies, L Gremillet, J J Honrubia, T Johzaki, R J Kingham, M Sherlock, and A A Solodov. Theory of Fast Electron Transport for Fast Ignition. *Nuclear Fusion*, 54(5):54003, 2014. ISSN 17414326. doi: 10.1088/0029-5515/54/5/054003. URL http://arxiv.org/abs/1304.1040{%}0Ahttp://dx.doi.org/10.1088/0029-5515/54/5/054003.

[5] Paul McKenna, David Neely, Robert Bingham, and Dino A. Jaroszynski. *Laser-plasma interactions and applications*. 2013. ISBN 9783319000381. doi: 10.1007/978-3-319-00038-1.

[6] Andrea Macchi, Marco Borghesi, and Matteo Passoni. Ion acceleration by superintense laser-plasma interaction. *Reviews of Modern Physics*, 85(2): 751–793, 2013. ISSN 00346861. doi: 10.1103/RevModPhys.85.751.

[7] Timur Zh Esirkepov, James K Koga, Atsushi Sunahara, Toshimasa Morita, Masaharu Nishikino, Kei Kageyama, Hideo Nagatomo, Katsunobu Nishihara, Akito Sagisaka, Hideyuki Kotaki, Tatsufumi Nakamura, Yuji Fukuda, Hajime Okada, Alexander S Pirozhkov, Akifumi Yogo, Mamiko Nishiuchi, Hiromitsu Kiriyama, Kiminori Kondo, Masaki Kando, and Sergei V Bulanov. Prepulse and amplified spontaneous emission effects on the interaction of a petawatt class laser with thin solid targets. *Nuclear Instruments and Methods in Physics Research, Section A: Accelerators, Spectrometers, Detectors and Associated Equipment*, 745:150–163, 2014. ISSN 01689002. doi: 10.1016/j.nima.2014.01.056. URL http://dx.doi.org/10.1016/j.nima.2014.01.056.

[8] Julien Fuchs, Patrick Audebert, Marco Borghesi, Henri Pépin, and Oswald Willi. Laser acceleration of low emittance, high energy ions and applications. *Comptes Rendus Physique*, 10(2-3):176–187, 2009. ISSN 16310705. doi: 10.1016/j.crhy.2009.03.011. URL http://dx.doi.org/10.1016/j.crhy.2009.03.011.

[9] J. Fuchs, T. E. Cowan, P. Audebert, H. Ruhl, L. Gremillet, A. Kemp, M. Allen, A. Blazevic, J. C. Gauthier, M. Geissel, M. Hegelich, S. Karsch, P. Parks, M. Roth, Y. Sentoku, R. Stephens, and E. M. Campbell. Spatial uniformity of laser-accelerated ultrahigh-current mev electron propagation in metals and insulators. *Physical Review Letters*, 91(25):2–5, 2003. ISSN 10797114. doi: 10.1103/PhysRevLett.91.255002.

[10] C. M. Brenner, S. R. Mirfayzi, D. R. Rusby, C. Armstrong, A. Alejo, L. A. Wilson, R. Clarke, H. Ahmed, N. M.H. Butler, D. Haddock, A. Higginson, A. McClymont, C. Murphy, M. Notley, P. Oliver, R. Allott, C. Hernandez-Gomez, S. Kar, P. McKenna, and D. Neely. Laser-driven x-ray and neutron source development for industrial applications of plasma accelerators. *Plasma Physics and Controlled Fusion*, 58(1), 2015. ISSN 13616587. doi: 10.1088/0741-3335/58/1/014039.

[11] O Tresca, D C Carroll, X H Yuan, B Aurand, V Bagnoud, C M Brenner, M Coury, J Fils, R J Gray, T Kühl, C Li, Y T Li, X X Lin, M N Quinn, R G Evans, B Zielbauer, M Roth, D Neely, and P McKenna. Controlling the properties of ultraintense laser-proton sources using transverse refluxing of hot electrons in shaped mass-limited targets. *Plasma Physics*

and Controlled Fusion, 53(10):105008, 2011. ISSN 07413335. doi: 10.1088/0741-3335/53/10/105008. URL http://stacks.iop.org/0741-3335/53/i=10/a=105008?key=crossref.5372c5cb6bd06a0e428c70312e314cef.

[12] S M Pfotenhauer, O Jäckel, A Sachtleben, J Polz, W Ziegler, H P Schlenvoigt, K U Amthor, M C Kaluza, K W D Ledingham, R Sauerbrey, P Gibbon, A P L Robinson, and H Schwoerer. Spectral shaping of laser generated proton beams. *New Journal of Physics*, 10, 2008. ISSN 13672630. doi: 10.1088/1367-2630/10/3/033034.

[13] P Gibbon. *Short Pulse Laser Interactions with Matter: An Introduction*. Imperial College Press, 2005. ISBN 1860941354. doi: 10.1142/P116.

[14] P McKenna, A P L Robinson, D Neely, M P Desjarlais, D C Carroll, M N Quinn, X H Yuan, C M Brenner, M Burza, M Coury, P Gallegos, R J Gray, K L Lancaster, Y T Li, X X Lin, O Tresca, and C.-G. Wahlström. Effect of Lattice Structure on Energetic Electron Transport in Solids Irradiated by Ultraintense Laser Pulses. *Physical Review Letters*, 106(18):185004, 2011. ISSN 0031-9007. doi: 10.1103/PhysRevLett.106.185004. URL https://link.aps.org/doi/10.1103/PhysRevLett.106.185004.

[15] M. Roth, A. Blazevic, M. Geissel, T. Schlegel, T. E. Cowan, M. Allen, J. C. Gauthier, P. Audebert, J. Fuchs, J. Meyer-Ter-Vehn, M. Hegelich, S. Karsch, and A. Pukhov. Energetic ions generated by laser pulses: A detailed study on target properties. *Physical Review Special Topics - Accelerators and Beams*, 5(6):31–38, 2002. ISSN 10984402. doi: 10.1103/PhysRevSTAB.5.061301.

[16] D. A. Maclellan, D. C. Carroll, R. J. Gray, N. Booth, M. Burza, M. P. Desjarlais, F. Du, B. Gonzalez-Izquierdo, D. Neely, H. W. Powell, A. P.L. Robinson, D. R. Rusby, G. G. Scott, X. H. Yuan, C. G. Wahlström, and P. McKenna. Annular fast electron transport in silicon arising from low-temperature resistivity. *Physical Review Letters*, 111(9), 2013. ISSN 00319007. doi: 10.1103/PhysRevLett.111.095001.

[17] David Andrew Maclellan. Effects of Electrical Resistivity on Fast Electron Transport in Relativistic Laser-Solid Interactions. 2014.

[18] S Atzeni and J Meyer-ter Vehn. *The Physics of Inertial Fusion*. Clarendon Press, Oxford, 2004. ISBN 0198562640. doi: 10.1093/acprof:oso/9780198562641.001.0001.

[19] Max Tabak, James Hammer, Michael E Glinsky, William L Kruer, Scott C Wilks, John Woodworth, E Michael Campbell, Michael D Perry, and Rodney J Mason. Ignition and high gain with ultra-powerful lasers. *Physics of Plasmas*, 1(5):1626–1634, 1994. ISSN 1070664X. doi: 10.1063/1.870664. URL http://scitation.aip.org/content/aip/journal/pop/1/5/10.1063/1.870664{%}5Cnhttp://scitation.aip.org/content/aip/journal/pop/1/5/10.1063/1.870664;jsessionid=2gj3ri51mlcdh.x-aip-live-02.

[20] A Pukhov and J Meyer-Ter-Vehn. Laser Hole Boring into Overdense Plasma and Relativistic Electron Currents for Fast Ignition of ICF Targets. *Physical Review Letters*, 79(14):2686–2689, 1997. ISSN 10797114. doi: 10.1103/PhysRevLett.79.2686.

[21] C D Chen, P K Patel, D S Hey, A J MacKinnon, M H Key, K U Akli, T Bartal, F N Beg, S Chawla, H Chen, R R Freeman, D P Higginson, A Link, T Y Ma, A G MacPhee, R B Stephens, L D Van Woerkom, B Westover, and M Porkolab. Bremsstrahlung and K-alpha fluorescence measurements for inferring conversion efficiencies into fast ignition relevant hot electrons. *Physics of Plasmas*, 16(8), 2009. ISSN 1070664X. doi: 10.1063/1.3183693.

[22] S Atzeni. Laser driven inertial fusion: The physical basis of current and recently proposed ignition experiments. *Plasma Physics and Controlled Fusion*, 51(12):124029, 2009. ISSN 07413335. doi: 10.1088/0741-3335/51/12/124029.

[23] J R Davies. Alfvén limit in fast ignition. *Physical Review E - Statistical Physics, Plasmas, Fluids, and Related Interdisciplinary Topics*, 69(6):4, 2004. ISSN 1063651X. doi: 10.1103/PhysRevE.69.065402.

[24] Mordecai D Rosen. The physics issues that determine inertial confinement fusion target gain and driver requirements: A tutorial. *Physics of Plasmas*, 6(5):1690–1699, 1999. ISSN 10897674. doi: 10.1063/1.873427. URL http://link.aip.org/link/PHPAEN/v6/i5/p1690/s1{&}Agg=doi.

[25] L C Jarrott, M S Wei, C McGuffey, A A Solodov, W Theobald, B Qiao, C Stoeckl, R Betti, H Chen, J Delettrez, T Döppner, E M Giraldez, V Y Glebov, H Habara, T Iwawaki, M H Key, R W Luo, F J Marshall, H S Mclean, C Mileham, P K Patel, J J Santos, H Sawada, R B Stephens,

T Yabuuchi, and F N Beg. Visualizing fast electron energy transport into laser-compressed high-density fast-ignition targets. *Nature Physics*, 12(5): 1–7, 2016. ISSN 17452481. doi: 10.1038/nphys3614. URL http://dx.doi.org/10.1038/nphys3614.

[26] M H Key, M D Cable, T E Cowan, K G Estabrook, B A Hammel, S P Hatchett, E A Henry, D E Hinkel, J D Kilkenny, J A Koch, W L Kruer, A B Langdon, B F Lasinski, R W Lee, B J MacGowan, A MacKinnon, J D Moody, M J Moran, A A Offenberger, D M Pennington, M D Perry, T J Phillips, T C Sangster, M S Singh, M A Stoyer, M Tabak, G L Tietbohl, M Tsukamoto, K Wharton, and S C Wilks. Hot electron production and heating by hot electrons in fast ignitor research. *Physics of Plasmas*, 5(5): 1966–1972, 1998. ISSN 1070-664X. doi: 10.1063/1.872867. URL http://aip.scitation.org/doi/10.1063/1.872867.

[27] P A Norreys, R H H Scott, K L Lancaster, J S Green, A P L Robinson, M Sherlock, R G Evans, M G Haines, S Kar, M Zepf, M H Key, J King, T Ma, T Yabuuchi, M S Wei, F N Beg, P Nilson, W Theobald, R B Stephens, J Valente, J R Davies, K Takeda, H Azechi, M Nakatsutsumi, T Tanimoto, R Kodama, and K A Tanaka. Recent fast electron energy transport experiments relevant to fast ignition inertial fusion. *Nuclear Fusion*, 49(10):104023, 2009. ISSN 00295515. doi: 10.1088/0029-5515/49/10/104023. URL http://stacks.iop.org/0029-5515/49/i=10/a=104023?key=crossref.7ce7f56dff4cef78ceb220f177693b11.

[28] P Norreys, D Batani, S Baton, F N Beg, R Kodama, P M Nilson, P Patel, F Perez, J J Santos, R H H Scott, V T Tikhonchuk, M Wei, and J Zhang. Fast electron energy transport in solid density and compressed plasma. *Nuclear Fusion*, 54(5), 2014. ISSN 17414326. doi: 10.1088/0029-5515/54/5/054004.

[29] R. R. Freeman, D. Batani, S. Baton, M. Key, and R. Stephens. The generation and transport of large currents in dense materials: The physics of electron transport relative to fast ignition. *Fusion Science and Technology*, 49(3):297–315, 2006. ISSN 15361055. doi: 10.13182/FST06-A1150.

[30] D. R. Rusby, L. A. Wilson, R. J. Gray, R. J. Dance, N. M.H. Butler, D. A. MacLellan, G. G. Scott, V. Bagnoud, B. Zielbauer, P. McKenna, and D. Neely. Measurement of the angle, temperature and flux of fast electrons

emitted from intense laser-solid interactions. *Journal of Plasma Physics*, 81 (5):1–9, 2015. ISSN 14697807. doi: 10.1017/S0022377815000835.

[31] S. Fujioka, H. Nishimura, H. Takabe, N. Yamamoto, K. Nishihara, D. Salzmann, T. Norimatsu, N. Miyanaga, K. Mima, H. Azechi, A. Sunahara, Y. Shimada, Y. Izawa, K. Nagai, F. Wang, J. Zhong, G. Zhao, Y. Li, Q. Dong, S. Wang, Y. Zhang, J. Zhang, Y-J Rhee, Y-W Lee, and D-H Kwon. Laser-produced plasmas as unique x-ray souces for industry and astrophysics. *Journal of Physics: Conference Series*, 244(PART 1), 2010. ISSN 17426596. doi: 10.1088/1742-6596/244/1/012001.

[32] U. Zastrau, P. Audebert, V. Bernshtam, E. Brambrink, T. Kämpfer, E. Kroupp, R. Loetzsch, Y. Maron, Yu Ralchenko, H. Reinholz, G. Röpke, A. Sengebusch, E. Stambulchik, I. Uschmann, L. Weingarten, and E. Förster. Temperature and Kα -yield radial distributions in laser-produced solid-density plasmas imaged with ultrahigh-resolution x-ray spectroscopy. *Physical Review E - Statistical, Nonlinear, and Soft Matter Physics*, 81(2):1–4, 2010. ISSN 15393755. doi: 10.1103/PhysRevE.81.026406.

[33] D. J. Hoarty, N. Sircombe, P. Beiersdorfer, C. R.D. Brown, M. P. Hill, L. M.R. Hobbs, S. F. James, J. Morton, E. Hill, M. Jeffery, J. W.O. Harris, R. Shepherd, E. Marley, E. Magee, J. Emig, J. Nilsen, H. K. Chung, R. W. Lee, and S. J. Rose. Modelling K shell spectra from short pulse heated buried microdot targets. *High Energy Density Physics*, 23:178–183, 2017. ISSN 15741818. doi: 10.1016/j.hedp.2017.04.004. URL http://dx.doi.org/10.1016/j.hedp.2017.04.004.

[34] C. R. D. Brown, D. J. Hoarty, S. F. James, D. Swatton, S. J. Hughes, J. W. Morton, T. M. Guymer, M. P. Hill, D. A. Chapman, J. E. Andrew, A. J. Comley, R. Shepherd, J. Dunn, H. Chen, M. Schneider, G. Brown, P. Beiersdorfer, and J. Emig. Measurements of Electron Transport in Foils Irradiated with a Picosecond Time Scale Laser Pulse. *Physical Review Letters*, 106(18): 185003, 2011. ISSN 0031-9007. doi: 10.1103/PhysRevLett.106.185003. URL https://link.aps.org/doi/10.1103/PhysRevLett.106.185003.

[35] R G Evans, E L Clark, R T Eagleton, A M Dunne, R D Edwards, W J Garbett, T J Goldsack, S James, C C Smith, B R Thomas, R Clarke, D J Neely, and S J Rose. Rapid heating of solid density material by a petawatt

laser. *Applied Physics Letters*, 86(19):1–3, 2005. ISSN 00036951. doi: 10.1063/1.1920422.

[36] S N Chen, G Gregori, P K Patel, H K Chung, R G Evans, R R Freeman, E Garcia Saiz, S H Glenzer, S B Hansen, F Y Khattak, J A King, A J Mackinnon, M M Notley, J R Pasley, D Riley, R B Stephens, R L Weber, S C Wilks, and F N Beg. Creation of hot dense matter in short-pulse laser-plasma interaction with tamped titanium foils. *Physics of Plasmas*, 14(10), 2007. ISSN 1070664X. doi: 10.1063/1.2777118.

[37] D J Hoarty, P Allan, S F James, C R D Brown, L M R Hobbs, M P Hill, J W O Harris, J Morton, M G Brookes, R Shepherd, J Dunn, H Chen, E Von Marley, P Beiersdorfer, H K Chung, R W Lee, G Brown, and J Emig. The first data from the Orion laser; measurements of the spectrum of hot, dense aluminium. *High Energy Density Physics*, 9(4):661–671, 2013. ISSN 15741818. doi: 10.1016/j.hedp.2013.06.005.

[38] N Booth, A P L Robinson, P Hakel, R J Clarke, R J Dance, D Doria, L A Gizzi, G Gregori, P Koester, L Labate, T Levato, B Li, M Makita, R C Mancini, J Pasley, P P Rajeev, D Riley, E Wagenaars, J N Waugh, and N C Woolsey. Laboratory measurements of resistivity in warm dense plasmas relevant to the microphysics of brown dwarfs. *Nature Communications*, 6 (May 2014):8742, 2015. ISSN 20411723. doi: 10.1038/ncomms9742. URL http://www.nature.com/doifinder/10.1038/ncomms9742.

[39] J. E. Bailey, G. A. Rochau, R. C. Mancini, C. A. Iglesias, J. J. MacFarlane, I. E. Golovkin, C. Blancard, Ph Cosse, and G. Faussurier. Experimental investigation of opacity models for stellar interior, inertial fusion, and high energy density plasmas. *Physics of Plasmas*, 16(5), 2009. ISSN 1070664X. doi: 10.1063/1.3089604.

[40] P. K. Patel, A. J. Mackinnon, M. H. Key, T. E. Cowan, M. E. Foord, M. Allen, D. F. Price, H. Ruhl, P. T. Springer, and R. Stephens. Isochoric heating of solid-density matter with an ultrafast proton beam. *Physical Review Letters*, 91(12):10–13, 2003. ISSN 10797114. doi: 10.1103/PhysRevLett.91.125004.

[41] R J Garland, M Borghesi, and A P L Robinson. Analysis of the fast electron scaling theory for the heating of a solid target. *Physics of Plasmas*, 23(8),

2016. ISSN 10897674. doi: 10.1063/1.4961004. URL http://dx.doi.org/10.1063/1.4961004.

[42] S Eliezer. *The Interaction of High-Power Lasers With Plasmas*, volume 45. CRC Press, 1st edition, 2003. ISBN 0 7503 0747 1. doi: 10.1088/0741-3335/45/2/701.

[43] Gerard A Mourou, Toshiki Tajima, and Sergei V Bulanov. Optics in the relativistic regime. *Reviews of Modern Physics*, 78(2), 2006. ISSN 00346861. doi: 10.1103/RevModPhys.78.309.

[44] T Dzelzainis, G Nersisyan, D Riley, L Romagnani, H Ahmed, A Bigongiari, M Borghesi, D Doria, B Dromey, M Makita, S White, S Kar, D Marlow, B Ramakrishna, G Sarri, M Zaka-Ul-Islam, M Zepf, and C L S Lewis. The TARANIS laser: A multi-Terawatt system for laser-plasma investigations. *Laser and Particle Beams*, 28(3):451–461, 2010. ISSN 02630346. doi: 10.1017/S0263034610000467. URL http://www.journals.cambridge.org/abstract{_}S0263034610000467.

[45] Sebastian Keppler, S Alexander, Marco Hornung, Hartmut Liebetrau, Joachim Hein, and Malte Christoph Kaluza. The generation of amplified spontaneous emission in high-power CPA laser systems. *Laser Photonics Review*, 277(2):264–277, 2016. doi: 10.1002/lpor.201500186.

[46] K. U. Akli, P. K. Patel, R. Van Maren, R. B. Stephens, M. H. Key, D. P. Higginson, B. Westover, C. D. Chen, A. J. Mackinnon, T. Bartal, F. N. Beg, S. Chawla, R. Fedosejevs, R. R. Freeman, D. S. Hey, G. E. Kemp, S. LePape, A. Link, T. Ma, A. G. MacPhee, H. S. McLean, Y. Ping, Y. Y. Tsui, L. D. Van Woerkom, M. S. Wei, T. Yabuuchi, and S. Yuspeh. A Dual Channel x-ray spectrometer for fast ignition research. *Journal of Instrumentation*, 5 (7), 2010. ISSN 17480221. doi: 10.1088/1748-0221/5/07/P07008.

[47] H M Milcherbg, R R Freeman, S C Davey, and R M More. Resistivity of a Simple Metal from Room Temperature to 10ˆ6 K. *Physical Review Letter*, 61(20), 1988. doi: 10.1103/PhysRevLett.61.2364.

[48] João Jorge Santos, D. Batani, S. D. Baton, F. N. Beg, T. Ceccotti, A. Debayle, F. Dorchies, J. L. Feugeas, C. Fourment, L. Gremillet, J. J. Honrubia, S. Hulin, A. Morace, P. Nicolaï, F. Pérez, H. Sawada, H. P. Schlenvoigt, V. T. Tikhonchuk, X. Vaisseau, B. Vauzour, and M. Wei.

Supra-thermal electron beam stopping power and guiding in dense plasmas. *Journal of Plasma Physics*, 79(4):429–435, 2013. ISSN 00223778. doi: 10.1017/S0022377813000305.

[49] R. H. H. Scott, F. Perez, J. J. Santos, C. P. Ridgers, J. R. Davies, K. L. Lancaster, S. D. Baton, Ph. Nicolai, R. M. G. M. Trines, A. R. Bell, S. Hulin, M. Tzoufras, S. J. Rose, and P. A. Norreys. A study of fast electron energy transport in relativistically intense laser-plasma interactions with large density scalelengths. *Physics of Plasmas*, 19(5):053104, 2012. ISSN 1070-664X. doi: 10.1063/1.4714615. URL http://aip.scitation.org/doi/10.1063/1.4714615.

[50] R H H Scott, F Pérez, M J V Streeter, E L Clark, J R Davies, H P Schlenvoigt, J J Santos, S Hulin, K L Lancaster, F Dorchies, C Fourment, B Vauzour, A A Soloviev, S D Baton, S J Rose, and P A Norreys. Fast electron beam measurements from relativistically intense, frequency-doubled laser-solid interactions. *New Journal of Physics*, 15, 2013. ISSN 13672630. doi: 10.1088/1367-2630/15/9/093021.

[51] M. H. Key, J. C. Adam, K. U. Akli, M. Borghesi, M. H. Chen, R. G. Evans, R. R. Freeman, H. Habara, S. P. Hatchett, J. M. Hill, A. Heron, J. A. King, R. Kodama, K. L. Lancaster, A. J. MacKinnon, P. Patel, T. Phillips, L. Romagnani, R. A. Snavely, R. Stephens, C. Stoeckl, R. Town, Y. Toyama, B. Zhang, M. Zepf, and P. A. Norreys. Fast ignition relevant study of the flux of high intensity laser-generated electrons via a hollow cone into a laser-imploded plasma. *Physics of Plasmas*, 15(2), 2008. ISSN 1070664X. doi: 10.1063/1.2834727.

[52] J. Fuchs, P. Antici, E. D'Humières, E. Lefebvre, M. Borghesi, E. Brambrink, C. A. Cecchetti, M. Kaluza, V. Malka, M. Manclossi, S. Meyroneinc, P. Mora, J. Schreiber, T. Toncian, H. Pépin, and P. Audebert. Laser-driven proton scaling laws and new paths towards energy increase. *Nature Physics*, 2(1):48–54, 2006. ISSN 17452473. doi: 10.1038/nphys199.

[53] R J Gray, D C Carroll, X H Yuan, C M Brenner, M Burza, M Coury, K L Lancaster, X X Lin, Y T Li, D Neely, M N Quinn, O Tresca, C G Wahlström, and P McKenna. Laser pulse propagation and enhanced energy coupling to fast electrons in dense plasma gradients. *New Journal of Physics*, 16, 2014. ISSN 13672630. doi: 10.1088/1367-2630/16/11/113075.

[54] X X Lin, Y T Li, B C Liu, F Liu, F Du, S J Wang, X Lu, L M Chen, L Zhang, X Liu, J Wang, F Liu, X L Liu, Z H Wang, J L Ma, Z Y Wei, and J Zhang. Effect of prepulse on fast electron lateral transport at the target surface irradiated by intense femtosecond laser pulses. *Physical Review E*, 82 (4):46401, 2010. ISSN 1539-3755. doi: 10.1103/PhysRevE.82.046401. URL https://link.aps.org/doi/10.1103/PhysRevE.82.046401.

[55] M. Coury, D. C. Carroll, A. P.L. Robinson, X. H. Yuan, C. M. Brenner, M. Burza, R. J. Gray, K. L. Lancaster, Y. T. Li, X. X. Lin, D. A. MacLellan, H. Powell, M. N. Quinn, O. Tresca, C. G. Wahlström, D. Neely, and P. McKenna. Injection and transport properties of fast electrons in ultraintense laser-solid interactions. *Physics of Plasmas*, 20(4), 2013. ISSN 1070664X. doi: 10.1063/1.4799726.

[56] J R Davies. Laser absorption by overdense plasmas in the relativistic regime. *Plasma Physics and Controlled Fusion*, 51(1):14006, 2009. ISSN 07413335. doi: 10.1088/0741-3335/51/1/014006.

[57] E. V. Marley, R. Shepherd, P. Beiersdorfer, G. Brown, H. Chen, J. Dunn, M. Foord, H. Scott, R. London, A. B. Steel, D. Hoarty, S. James, C. R.D. Brown, M. Hill, P. Allan, and L. Hobbs. Measurement and simulation of the temperature evolution of a short pulse laser heated buried layer target. *High Energy Density Physics*, 25:15–19, 2017. ISSN 15741818. doi: 10.1016/j.hedp.2017.09.002. URL https://doi.org/10.1016/j.hedp.2017.09.002.

[58] G Malka and J L Miquel. Experimental confirmation of ponderomotive-force electrons produced by an ultrarelativistic laser pulse on a solid target. *Physical Review Letters*, 77(1):75–78, 1996. ISSN 10797114. doi: 10.1103/PhysRevLett.77.75.

[59] D J Hoarty, P Allan, S F James, C R D Brown, L M R Hobbs, M P Hill, J W O Harris, J Morton, M G Brookes, R Shepherd, J Dunn, H Chen, E Von Marley, P Beiersdorfer, H K Chung, R W Lee, G Brown, and J Emig. Observations of the effect of ionization-potential depression in hot dense plasma. *Physical Review Letters*, 110(26):1–5, 2013. ISSN 00319007. doi: 10.1103/PhysRevLett.110.265003.

[60] M. Storm, B. Eichman, C. Orban, S. Jiang, G. Fiksel, C. Stoeckl, G. Dyer, T. Ditmire, R. Stephens, W. Theobald, J. A. Delettrez, R. R. Freeman, and

K. Akli. Kαx-ray imaging of laser-irradiated, limited-mass zirconium foils. *Physics of Plasmas*, 21(7), 2014. ISSN 10897674. doi: 10.1063/1.4889881.

[61] L V Kelydsh. IONIZATION IN THE FIELD OF A STRONG ELECTROMAGNETIC WAVE. *Sov. Phys. JETP*, 20(5), 1965.

[62] Maxim V Ammosov, Nikolai B Delone, and Vladimir P Krainov. Tunnel ionization of complex atoms and of atomic ions in an alternating electromagnetic field. *Sov. Phys. JETP*, 64(December 1986):138–141, 1986. ISSN 0044-4510. doi: 10.1117/12.938695. URL http://proceedings.spiedigitallibrary.org/proceeding.aspx?articleid=1243407.

[63] Andrea Macchi. *A Superintense Laser-Plasma Interaction Theory Primer*. Springer Netherlands, 1 edition, 2013. ISBN 978-94-007-6124-7. doi: 10.1007/978-94-007-6125-4. URL http://link.springer.com/10.1007/978-94-007-6125-4.

[64] F Amiranoff. Fast electron production in ultra-short high-intensity laser – plasma interaction. *Measurement Science & Technology*, 12:1795–1800, 2001. URL http://iopscience.iop.org/0957-0233/12/11/306.

[65] Scott C Wilks and William L Kruer. Absorption of ultrashort, ultra-intense laser light by solids and overdense plasmas. *IEEE Journal of Quantum Electronics*, 33(11):1954–1968, 1997. ISSN 00189197. doi: 10.1109/3.641310.

[66] N A Krall and A W Trivelpiece. *Principle of Plasma Physics*. 1973.

[67] F F Chen. *Introduction to Plasma Physics and Controlled Fusion*. Plenum Press, New York, 2nd edition, 1984. ISBN 9788578110796.

[68] H Kersten. *Fundamentals of Plasma Physics III*, volume 49. Cambridge University Press, 2007. ISBN 9780521821162. doi: 10.1088/0741-3335/49/2/B01.

[69] T J M Boyd and J J Sanderson. *The Physics of Plasmas*. Cambridge University Press, 2003. ISBN 9780874216561. doi: 10.1007/s13398-014-0173-7.2. URL http://www.ncbi.nlm.nih.gov/pubmed/15003161{%}5Cnhttp://cid.oxfordjournals.org/lookup/doi/10.1093/cid/cir991{%}5Cnhttp://www.scielo.cl/pdf/udecada/v15n26/art06.pdf{%}5Cnhttp://www.scopus.com/inward/record.url?eid=2-s2.0-84861150233{&}partnerID=tZOtx3y1.

[70] R O Dendy. *Plasma Dynamics*. Clarendon Press, 1st edition, 1990. ISBN 978-0198520412. URL http://ukcatalogue.oup.com/product/9780198520412.do.

[71] P McKenna, D C Carroll, O Lundh, F Nürnberg, K Markey, S Bandyopadhyay, D Batani, R G Evans, R Jafer, S Kar, D Neely, D Pepler, M N Quinn, R Redaelli, M Roth, C G Wahlström, X H Yuan, and M Zepf. Effects of front surface plasma expansion on proton acceleration in ultraintense laser irradiation of foil targets. *IEEE International Conference on Plasma Science*, (2008):591–596, 2009. ISSN 07309244. doi: 10.1109/PLASMA.2009.5227320.

[72] B Bezzerides, S J Gitomer, and D W Forslund. Randomness, maxwellian distributions, and resonance absorption. *Physical Review Letters*, 44(10): 651–654, 1980. ISSN 10797114. doi: 10.1103/PhysRevLett.44.651.

[73] F N Beg, A R Bell, A E Dangor, C N Danson, A P Fews, M E Glinsky, B A Hammel, P Lee, P A Norreys, and M Tatarakis. A study of picosecond laser-solid interactions up to 1019W cm-2. *Physics of Plasmas*, 4(2):447–457, 1997. ISSN 1070664X. doi: 10.1063/1.872103.

[74] S C Wilks, W L Kruer, M Tabak, and A B Langdon. Absorption of ultraintense laser pulses. *Physical Review Letters*, 69(9):1383–1386, 1992. ISSN 00319007. doi: 10.1103/PhysRevLett.69.1383. URL http://prl.aps.org/abstract/PRL/v69/i9/p1383{_}1.

[75] M Sherlock. Universal scaling of the electron distribution function in one-dimensional simulations of relativistic laser-plasma interactions. *Physics of Plasmas*, 16(10), 2009. ISSN 1070664X. doi: 10.1063/1.3240341.

[76] M C Levy, S C Wilks, M Tabak, and M G Baring. Conservation laws and conversion efficiency in ultraintense laser-overdense plasma interactions. *Physics of Plasmas*, 20(10), 2013. ISSN 1070664X. doi: 10.1063/1.4821607.

[77] A P L Robinson and M Sherlock. Magnetic collimation of fast electrons produced by ultraintense laser irradiation by structuring the target composition. *Physics of Plasmas*, 14(8), 2007. ISSN 1070664X. doi: 10.1063/1.2768317.

[78] A P L Robinson, R J Kingham, C P Ridgers, and M Sherlock. Effect of transverse density modulations on fast electron transport in dense plasmas. *Plasma Physics and Controlled Fusion*, 50(6):65017–65019, 2008. ISSN 07413335. doi: 10.1088/0741-3335/50/6/065019.

[79] J J Santos, F Amiranoff, S D Baton, L Gremillet, M Koenig, E Martinolli, M Rabec Le Gloahec, C Rousseaux, D Batani, a. Bernardinello, G Greison, and T Hall. Fast Electron Transport in Ultraintense Laser Pulse Interaction with Solid Targets by Rear-Side Self-Radiation Diagnostics. *Physical review letters*, 89(2):8–11, 2002. ISSN 0031-9007. doi: 10.1103/PhysRevLett.89.025001. URL http://link.aps.org/doi/10.1103/PhysRevLett.89.025001.

[80] Y Ping, R Shepherd, B F Lasinski, M Tabak, H Chen, H K Chung, K B Fournier, S B Hansen, A Kemp, D A Liedahl, K Widmann, S C Wilks, W Rozmus, and M Sherlock. Absorption of short laser pulses on solid targets in the ultrarelativistic regime. *Physical Review Letters*, 100(8):6–9, 2008. ISSN 00319007. doi: 10.1103/PhysRevLett.100.085004.

[81] H S Park, D M Chambers, H K Chung, R J Clarke, R Eagleton, E Giraldez, T Goldsack, R Heathcote, N Izumi, M H Key, J A King, J A Koch, O L Landen, A Nikroo, P K Patel, D F Price, B A Remington, H F Robey, R A Snavely, D A Steinman, R B Stephens, C Stoeckl, M Storm, M Tabak, W Theobald, R P J Town, J E Wickersham, and B B Zhang. High-energy Kalpha radiography using high-intensity, short-pulse lasers. *Physics of Plasmas*, 13(5), 2006. ISSN 1070664X. doi: 10.1063/1.2178775.

[82] B Westover, C D Chen, P K Patel, M H Key, H McLean, R Stephens, and F N Beg. Fast electron temperature and conversion efficiency measurements in laser-irradiated foil targets using a bremsstrahlung x-ray detector. *Physics of Plasmas*, 18(6), 2011. ISSN 1070664X. doi: 10.1063/1.3594622.

[83] E Martinolli, D Batani, E Perelli-Cippo, F Scianitti, M Koenig, J J Santos, F Amiranoff, S D Baton, T Hall, M Key, A Mackinnon, R Snavely, R Freeman, C Andersen, J King, R Stephens, M Rabec Le Gloahec, C Rousseaux, and T E Cowan. Fast electron transport and heating in solid-density matter. *Laser and Particle Beams*, 20(2):171–175, 2002. ISSN 02630346. doi: 10.1017/S0263034602202037.

[84] E Martinolli, M Koenig, S D Baton, J J Santos, F Amiranoff, D Batani, E Perelli-Cippo, F Scianitti, L Gremillet, R Mélizzi, A Decoster, C Rousseaux, T A Hall, M H Key, R Snavely, A J MacKinnon, R R Freeman, J A King, R Stephens, D Neely, and R J Clarke. Fast-electron transport and heating of solid targets in high-intensity laser interactions measured by K-alpha fluorescence. *Physical Review E - Statistical, Nonlinear, and Soft Matter Physics*, 73(4):1–5, 2006. ISSN 15393755. doi: 10.1103/PhysRevE.73.046402.

[85] G Gregori, S B Hansen, R Clarke, R Heathcote, M H Key, J King, R I Klein, N Izumi, A J Mackinnon, S J Moon, H S Park, J Pasley, N Patel, P K Patel, B A Remington, D D Ryutov, R Shepherd, R A Snavely, S C Wilks, B B Zhang, and S H Glenzer. Experimental characterization of a strongly coupled solid density plasma generated in a short-pulse laser target interaction. *Contributions to Plasma Physics*, 45(3-4):284–292, 2005. ISSN 08631042. doi: 10.1002/ctpp.200510032.

[86] S B Hansen, A Ya Faenov, T A Pikuz, K B Fournier, R Shepherd, H Chen, K Widmann, S C Wilks, Y Ping, H K Chung, A Niles, J R Hunter, G Dyer, and T Ditmire. Temperature determination using K-alpha spectra from M-shell Ti ions. *Physical Review E - Statistical, Nonlinear, and Soft Matter Physics*, 72(3):1–4, 2005. ISSN 15393755. doi: 10.1103/PhysRevE.72.036408.

[87] J Myatt, W Theobald, J A Delettrez, C Stoeckl, M Storm, T C Sangster, A V Maximov, and R W Short. High-intensity laser interactions with mass-limited solid targets and implications for fast-ignition experiments on OMEGA EP. *Physics of Plasmas*, 14(5), 2007. ISSN 1070664X. doi: 10.1063/1.2472371.

[88] P M Nilson, W Theobald, J Myatt, C Stoeckl, M Storm, O V Gotchev, J D Zuegel, R Betti, D D Meyerhofer, and T C Sangster. High-intensity laser-plasma interactions in the refluxing limit. *Physics of Plasmas*, 15(5): 1–8, 2008. ISSN 1070664X. doi: 10.1063/1.2889449.

[89] K. L. Lancaster, J. S. Green, D. S. Hey, K. U. Akli, J. R. Davies, R. J. Clarke, R. R. Freeman, H. Habara, M. H. Key, R. Kodama, K. Krushelnick, C. D. Murphy, M. Nakatsutsumi, P. Simpson, R. Stephens, C. Stoeckl,

T. Yabuuchi, M. Zepf, and P. A. Norreys. Measurements of energy transport patterns in solid density laser plasma interactions at intensities of 5e20Wcm-2. *Physical Review Letters*, 98(12):1–4, 2007. ISSN 00319007. doi: 10.1103/PhysRevLett.98.125002.

[90] P. M. Nilson, W. Theobald, C. Mileham, C. Stoeckl, J. F. Myatt, J. A. Delettrez, J. MacFarlane, I. A. Begishev, J. D. Zuegel, R. Betti, T. C. Sangster, and D. D. Meyerhofer. Target-heating effects on the Kα1,2-emission spectrum from solid targets heated by laser-generated hot electrons. *Physics of Plasmas*, 18(4):18–22, 2011. ISSN 1070664X. doi: 10.1063/1.3574383.

[91] P. A. Norreys, M. Santala, E. Clark, M. Zepf, I. Watts, F. N. Beg, K. Krushelnick, M. Tatarakis, A. E. Dangor, X. Fang, P. Graham, T. McCanny, R. P. Singhal, K. W.D. Ledingham, A. Creswell, D. C.W. Sanderson, J. Magill, A. Machacek, J. S. Wark, R. Allott, B. Kennedy, and D. Neely. Observation of a highly directional γ-ray beam from ultrashort, ultraintense laser pulse interactions with solids. *Physics of Plasmas*, 6(5 I):2150–2156, 1999. ISSN 1070664X. doi: 10.1063/1.873466.

[92] Hui Chen, S C Wilks, W L Kruer, P K Patel, and R Shepherd. Hot electron energy distributions from ultraintense laser solid interactions. *Physics of Plasmas*, 16(2), 2009. ISSN 1070664X. doi: 10.1063/1.3080197.

[93] Matthew C Levy, Scott C Wilks, Max Tabak, Stephen B Libby, and Matthew G Baring. Petawatt laser absorption bounded. *Nature Communications*, 5(May):4149, 2014. ISSN 20411723. doi: 10.1038/ncomms5149. URL http://www.nature.com/ncomms/2014/140618/ncomms5149/full/ncomms5149.html.

[94] T D Arber, K Bennett, C S Brady, A Lawrence-Douglas, M G Ramsay, N J Sircombe, P Gillies, R G Evans, H Schmitz, A R Bell, and C P Ridgers. Contemporary particle-in-cell approach to laser-plasma modelling. *Plasma Physics and Controlled Fusion*, 57(11): 113001, 2015. ISSN 13616587. doi: 10.1088/0741-3335/57/11/113001. URL http://dx.doi.org/10.1088/0741-3335/57/11/113001http://dx.doi.org/10.1088/0741-3335/57/11/113001{%}5Cnhttp://stacks.iop.org/0741-3335/57/i=11/a=113001?key=crossref.907aa156b73b99b125b1a0ae886c4c22.

[95] R P J Town, C Chen, L A Cottrill, M H Key, W L Kruer, A B Langdon, B F Lasinski, R A Snavely, C H Still, M Tabak, D R Welch, and S C Wilks. Simulations of electron transport for fast ignition using LSP. *Nuclear Instruments and Methods in Physics Research, Section A: Accelerators, Spectrometers, Detectors and Associated Equipment*, 544(1-2):61–66, 2005. ISSN 01689002. doi: 10.1016/j.nima.2005.01.194.

[96] A P L Robinson, M H Key, and M Tabak. Focusing of relativistic electrons in dense plasma using a resistivity-gradient-generated magnetic switchyard. *Physical Review Letters*, 108(12):1–5, 2012. ISSN 00319007. doi: 10.1103/PhysRevLett.108.125004.

[97] A P L Robinson, H Schmitz, J S Green, C P Ridgers, and N Booth. Guiding of laser-generated fast electrons by exploiting the resistivity-gradients around a conical guide element. *Plasma Physics and Controlled Fusion*, 57(6):64004, 2015. ISSN 13616587. doi: 10.1088/0741-3335/57/6/064004. URL http://stacks.iop.org/0741-3335/57/i=6/a=064004?key=crossref.897ad338bb1759121513b182302a3f77.

[98] A P L Robinson, H Schmitz, and J Pasley. Rapid embedded wire heating via resistive guiding of laser-generated fast electrons as a hydrodynamic driver. *Physics of Plasmas*, 20(12), 2013. ISSN 1070664X. doi: 10.1063/1.4838238.

[99] A P L Robinson, M Sherlock, and P A Norreys. Artificial collimation of fast-electron beams with two laser pulses. *Physical Review Letters*, 100(2):1–4, 2008. ISSN 00319007. doi: 10.1103/PhysRevLett.100.025002.

[100] J R Davies, J S Green, and P A Norreys. Electron beam hollowing in laser-solid interactions. *Plasma Physics and Controlled Fusion*, 48(8):1181–1199, 2006. ISSN 07413335. doi: 10.1088/0741-3335/48/8/010.

[101] B Ramakrishna, S Kar, A P L Robinson, D J Adams, K Markey, M N Quinn, X H Yuan, P McKenna, K L Lancaster, J S Green, R H H Scott, P A Norreys, J Schreiber, and M Zepf. Laser-driven fast electron collimation in targets with resistivity boundary. *Physical Review Letters*, 105(13):1–4, 2010. ISSN 00319007. doi: 10.1103/PhysRevLett.105.135001.

[102] R A B Alraddadi, A P L Robinson, N C Woolsey, and J Pasley. The effect of grading the atomic number at resistive guide element interface on magnetic

collimation. *Physics of Plasmas*, 23(7), 2016. ISSN 10897674. doi: 10.1063/1.4959037. URL http://dx.doi.org/10.1063/1.4959037.

[103] R A B Alraddadi, A P L Robinson, J Pasley, and N C Woolsey. Enhancing relativistic electron beam propagation through the use of graded resistivity guides. *Physics of Plasmas*, 25(2):23104, 2018. ISSN 10897674. doi: 10.1063/1.5004265. URL http://aip.scitation.org/doi/10.1063/1.5004265.

[104] J R Davies, A R Bell, M G Haines, and S M Guérin. Short-pulse high-intensity laser-generated fast electron transport into thick solid targets. *Physical Review E - Statistical Physics, Plasmas, Fluids, and Related Interdisciplinary Topics*, 56(6):7193–7203, 1997. ISSN 1063651X. doi: 10.1103/PhysRevE.56.7193. URL http://link.aps.org/doi/10.1103/PhysRevE.56.7193{%}5Cnhttp://journals.aps.org/pre/abstract/10.1103/PhysRevE.56.7193.

[105] S Kar, A P L Robinson, D C Carroll, O Lundh, K Markey, P McKenna, P Norreys, and M Zepf. Guiding of relativistic electron beams in solid targets by resistively controlled magnetic fields. *Physical Review Letters*, 102(5):1–4, 2009. ISSN 00319007. doi: 10.1103/PhysRevLett.102.055001.

[106] P McKenna, D A MacLellan, N M H Butler, R J Dance, R J Gray, A P L Robinson, D Neely, and M P Desjarlais. Influence of low-temperature resistivity on fast electron transport in solids: Scaling to fast ignition electron beam parameters. *Plasma Physics and Controlled Fusion*, 57(6), 2015. ISSN 13616587. doi: 10.1088/0741-3335/57/6/064001.

[107] David Salzmann. *Atomic Physics in Hot Plasmas*. Oxford University Press, 1st edition, 1998. ISBN 0195109309.

[108] Mp Desjarlais. Practical Improvements to the Lee-More Conductivity Near the Metal-Insulator Transition. *Contributions to Plasma Physics*, 41(2-3):267–270, 2001. ISSN 0863-1042. doi: 10.1002/1521-3986(200103)41:2/3⟨267::AID-CTPP267⟩3.0.CO;2-P. URL http://onlinelibrary.wiley.com/doi/10.1002/1521-3986(200103)41:2/3{%}3C267::AID-CTPP267{%}3E3.0.CO;2-P/abstract{%}5Cnhttp://doi.wiley.com/10.1002/1521-3986(200103)41:2/3{%}3C267::AID-CTPP267{%}3E3.0.CO;2-P.

[109] Ruoxian Ying and G Kalman. Thomas-Fermi model for dense plasmas. *Physical Review A*, 40(7):3927–3950, 1989. ISSN 10502947. doi: 10.1103/PhysRevA.40.3927.

[110] R M More, K H Warren, D A Young, and G B Zimmerman. A new quotidian equation of state (QEOS) for hot dense matter. *Physics of Fluids*, 31(10): 3059–3078, 1988. ISSN 10897666. doi: 10.1063/1.866963.

[111] A P L Robinson, H Schmitz, J S Green, C P Ridgers, N Booth, and J Pasley. Control of wire heating with resistively guided fast electrons through an inverse conical taper. *Physics of Plasmas*, 22(4):1–6, 2015. ISSN 10897674. doi: 10.1063/1.4917065.

[112] Elliott H. Lieb. Thomas-fermi and related theories of atoms and molecules. In *The Stability of Matter: From Atoms to Stars: Fourth Edition*. 1981. ISBN 3540420835. doi: 10.1007/3-540-27056-6_20.

[113] E Fermi. Un Metodo Statistico per la Determinazione di alcune Prioprietà dell'Atomo. *Rend. Accad. Naz. Lincei*, 6(6):602–607, 1927. ISSN 0001-4435.

[114] L H Thomas. The calculation of atomic fields. *Mathematical Proceedings of the Cambridge Philosophical Society*, 23(5):542–548, 1927. ISSN 14698064. doi: 10.1017/S0305004100011683.

[115] R P Feynman, N Metropolis, and E Teller. Equations of state of elements based on the generalized fermi-thomas theory. *Physical Review*, 75(10): 1561–1573, 1949. ISSN 0031899X. doi: 10.1103/PhysRev.75.1561.

[116] Elliott H Lieb and Barry Simon. The Thomas-Fermi theory of atoms, molecules and solids. *Advances in Mathematics*, 23(1):22–116, 1977. ISSN 10902082. doi: 10.1016/0001-8708(77)90108-6.

[117] A R Bell. New Equations of State for Medusa. Technical report, Science Research Council, Chilton (UK). Rutherford and Appleton Labs, 1980.

[118] R M More. Pressure Ionization, Resonances, and the Continuity of Bound and Free States. *Advances in Atomic and Molecular Physics*, 21(C):305–356, 1985. ISSN 00652199. doi: 10.1016/S0065-2199(08)60145-1.

[119] J R Davies, A R Bell, and M Tatarakis. Magnetic focusing and trapping of high-intensity laser-generated fast electrons at the rear of solid targets. *Physical Review E - Statistical Physics, Plasmas, Fluids, and Related Interdisciplinary Topics*, 59(5):6032–6036, 1999. ISSN 1063651X. doi: 10.1103/PhysRevE.59.6032.

[120] J Clérouin, P Noiret, P Blottiau, V Recoules, B Siberchicot, P Renaudin, C Blancard, G Faussurier, B Holst, and C E Starrett. A database for equations of state and resistivities measurements in the warm dense matter regime. *Physics of Plasmas*, 19(8), 2012. ISSN 1070664X. doi: 10.1063/1.4742317.

[121] Toru Sasaki, Yuuri Yano, Mitsuo Nakajima, Tohru Kawamura, and Kazuhiko Hortoka. Warm-dense-matter studies using pulse-powered wire discharges in water. *Laser and Particle Beams*, 24(3):371–380, 2006. ISSN 02630346. doi: 10.1017/S0263034606060538.

[122] Hannes R Rüter and Ronald Redmer. Ab initio simulations for the ion-ion structure factor of warm dense aluminum. *Physical Review Letters*, 112(14): 1–5, 2014. ISSN 10797114. doi: 10.1103/PhysRevLett.112.145007.

[123] T G White, S Richardson, B J B Crowley, L K Pattison, J W O Harris, and G Gregori. Orbital-Free Density-Functional Theory Simulations of the Dynamic Structure Factor of Warm Dense Aluminum. *Physical Review Letters*, 111(17):175002, 2013. ISSN 0031-9007. doi: 10.1103/PhysRevLett.111.175002. URL https://link.aps.org/doi/10.1103/PhysRevLett.111.175002.

[124] A P L Robinson, H Schmitz, and P McKenna. Resistivity of non-crystalline carbon in the 1-100 eV range. *New Journal of Physics*, 17(8):83045, 2015. ISSN 13672630. doi: 10.1088/1367-2630/17/8/083045. URL http://dx.doi.org/10.1088/1367-2630/17/8/083045.

[125] Ronald Redmer. Electrical conductivity of dense metal plasmas. *Physical Review E - Statistical Physics, Plasmas, Fluids, and Related Interdisciplinary Topics*, 59(1):1073–1081, 1999. ISSN 1063651X. doi: 10.1103/PhysRevE.59.1073. URL http://link.aps.org/doi/10.1103/PhysRevE.59.1073.

[126] M P Desjarlais, J D Kress, and L A Collins. Electrical conductivity for warm, dense aluminum plasmas and liquids. *Physical Review E - Statistical*

Physics, Plasmas, Fluids, and Related Interdisciplinary Topics, 66(2):2–5, 2002. ISSN 1063651X. doi: 10.1103/PhysRevE.66.025401.

[127] Y T Lee and R M More. An electron conductivity model for dense plasmas. *Physics of Fluids*, 27(5):1273, 1984. ISSN 00319171. doi: 10.1063/1.864744. URL http://scitation.aip.org/content/aip/journal/pof1/27/5/10.1063/1.864744.

[128] David R Blackman, A P L Robinson, and John Pasley. Role of low temperature resistivity on fast electron transport in disordered aluminium and copper. *Physics of Plasmas*, 22(8):83108, 2015. ISSN 1070-664X. doi: 10.1063/1.4928112. URL http://scitation.aip.org/content/aip/journal/pop/22/8/10.1063/1.4928112{%}0Ahttp://aip.scitation.org/doi/10.1063/1.4928112.

[129] Sandra Kuhlbrodt and Ronald Redmer. Transport coefficients for dense metal plasmas. *Physical Review E - Statistical Physics, Plasmas, Fluids, and Related Interdisciplinary Topics*, 62(5):7191–7200, 2000. ISSN 1063651X. doi: 10.1103/PhysRevE.62.7191. URL http://www.ncbi.nlm.nih.gov/pubmed/11102075.

[130] A P L Robinson and H Schmitz. Elliptical magnetic mirror generated via resistivity gradients for fast ignition inertial confinement fusion. *Physics of Plasmas*, 20(6):1–8, 2013. ISSN 1070664X. doi: 10.1063/1.4812193.

[131] Laurent Gremillet, Guy Bonnaud, and François Amiranoff. Filamented transport of laser-generated relativistic electrons penetrating a solid target. *Physics of Plasmas*, 9(3):941, 2002. ISSN 1070664X. doi: 10.1063/1.1432994.

[132] J M Ziman. *Principles of the Theory of Solids [Paperback]*. Cambridge University Press, 2nd edition, 1979. ISBN 0521297338. URL http://www.amazon.com/Principles-Theory-Solids-J-Ziman/dp/0521297338.

[133] R Jung, J Osterholz, K Löwenbrück, S Kiselev, G Pretzler, A Pukhov, O Willi, S Kar, M Borghesi, W Nazarov, S Karsch, R Clarke, and D Neely. Study of electron-beam propagation through preionized dense foam plasmas. *Physical Review Letters*, 94(19):2–5, 2005. ISSN 00319007. doi: 10.1103/PhysRevLett.94.195001.

[134] A. R. Bell, J. R. Davies, S. Guerin, and H. Ruhl. Fast-electron transport in high-intensity short-pulse laser-solid experiments. *Plasma Physics and Controlled Fusion*, 39:653–659, 1997.

[135] A P L Robinson, A R Bell, and R J Kingham. Fast electron transport and ionization in a target irradiated by a high power laser. *Plasma Physics and Controlled Fusion*, 48(8):1063–1076, 2006. ISSN 0741-3335. doi: 10.1088/0741-3335/48/8/002. URL http://stacks.iop.org/0741-3335/48/i=8/a=002?key=crossref.0163e1785384cbff14935cf66c02f3af.

[136] J R Davies. Electric and magnetic field generation and target heating by laser-generated fast electrons. *Physical Review E - Statistical Physics, Plasmas, Fluids, and Related Interdisciplinary Topics*, 68(5):56404, 2003. ISSN 1063651X. doi: 10.1103/PhysRevE.68.056404.

[137] A R Bell and R J Kingham. Resistive Collimation of Electron Beams in Laser-Produced Plasmas. *Physical Review Letters*, 91(3):35003, 2003. ISSN 10797114. doi: 10.1103/PhysRevLett.91.035003.

[138] T. Kluge, M. Bussmann, U. Schramm, and T. E. Cowan. Simple scaling equations for electron spectra, currents, and bulk heating in ultra-intense short-pulse laser-solid interaction. *Physics of Plasmas*, 25(7), 2018. ISSN 10897674. doi: 10.1063/1.5037753.

[139] X. H. Yang, H. B. Zhuo, Y. Y. Ma, H. Xu, T. P. Yu, D. B. Zou, Z. Y. Ge, B. B. Xu, Q. J. Zhu, F. Q. Shao, and M. Borghesi. Effects of resistive magnetic field on fast electron divergence measured in experiments. *Plasma Physics and Controlled Fusion*, 57(2), 2015. ISSN 13616587. doi: 10.1088/0741-3335/57/2/025011.

[140] A. J. Kemp, Y. Sentoku, V. Sotnikov, and S. C. Wilks. Collisional relaxation of superthermal electrons generated by relativistic laser pulses in dense plasma. *Physical Review Letters*, 97(23):8–11, 2006. ISSN 00319007. doi: 10.1103/PhysRevLett.97.235001.

[141] J R Davies. How wrong is collisional Monte Carlo modeling of fast electron transport in high-intensity laser-solid interactions? *Physical Review E - Statistical Physics, Plasmas, Fluids, and Related Interdisciplinary Topics*, 65(2):1–14, 2002. ISSN 1063651X. doi: 10.1103/PhysRevE.65.026407.

[142] X H Yang, M Borghesi, and A P L Robinson. Fast-electron self-collimation in a plasma density gradient. *Physics of Plasmas*, 19(6), 2012. ISSN 1070664X. doi: 10.1063/1.4729322.

[143] D. A. Maclellan, D. C. Carroll, R. J. Gray, A. P.L. Robinson, M. P. Desjarlais, D. Neely, and P. McKenna. Influence of laser-drive parameters on annular fast electron transport in silicon. *Plasma Physics and Controlled Fusion*, 56(8), 2014. ISSN 13616587. doi: 10.1088/0741-3335/56/8/084002.

[144] S. Chawla, M. S. Wei, R. Mishra, K. U. Akli, C. D. Chen, H. S. McLean, A. Morace, P. K. Patel, H. Sawada, Y. Sentoku, R. B. Stephens, and F. N. Beg. Effect of target material on fast-electron transport and resistive collimation. *Physical Review Letters*, 110(2):1–5, 2013. ISSN 00319007. doi: 10.1103/PhysRevLett.110.025001.

[145] A G R Thomas, M Tzoufras, A P L Robinson, R J Kingham, C P Ridgers, M Sherlock, and A R Bell. A review of Vlasov-Fokker-Planck numerical modeling of inertial confinement fusion plasma. *Journal of Computational Physics*, 231(3):1051–1079, 2012. ISSN 00219991. doi: 10.1016/j.jcp.2011.09.028.

[146] C K Birdsall and A B Langdon. *Plasma Physics via Computer Simulation*. CRC Press, 2005. ISBN 9780750310253.

[147] D. A. Chapman, S. J. Hughes, D. J. Hoarty, and D. J.R. Swatton. Hot electron transport modelling in fast ignition relevant targets with non-Spitzer resistivity. *Journal of Physics: Conference Series*, 244(PART 2), 2010. ISSN 17426596. doi: 10.1088/1742-6596/244/2/022031.

[148] A Debayle, J J Honrubia, E D'Humières, and V T Tikhonchuk. Divergence of laser-driven relativistic electron beams. *Physical Review E - Statistical, Nonlinear, and Soft Matter Physics*, 82(3):1–10, 2010. ISSN 15393755. doi: 10.1103/PhysRevE.82.036405.

[149] J. S. Green, V. M. Ovchinnikov, R. G. Evans, K. U. Akli, H. Azechi, F. N. Beg, C. Bellei, R. R. Freeman, H. Habara, R. Heathcote, M. H. Key, J. A. King, K. L. Lancaster, N. C. Lopes, T. Ma, A. J. MacKinnon, K. Markey, A. McPhee, Z. Najmudin, P. Nilson, R. Onofrei, R. Stephens, K. Takeda, K. A. Tanaka, W. Theobald, T. Tanimoto, J. Waugh, L. Van Woerkom, N. C. Woolsey, M. Zepf, J. R. Davies, and P. A. Norreys. Effect of laser intensity

on fast-electron-beam divergence in solid-density plasmas. *Physical Review Letters*, 100(1):1–4, 2008. ISSN 00319007. doi: 10.1103/PhysRevLett.100.015003.

[150] M. Nakatsutsumi, J. R. Davies, R. Kodama, J. S. Green, K. L. Lancaster, K. U. Akli, F. N. Beg, S. N. Chen, D. Clark, R. R. Freeman, C. D. Gregory, H. Habara, R. Heathcote, D. S. Hey, K. Highbarger, P. Jaanimagi, M. H. Key, K. Krushelnick, T. Ma, A. MacPhee, A. J. MacKinnon, H. Nakamura, R. B. Stephens, M. Storm, M. Tampo, W. Theobald, L. Van Woerkom, R. L. Weber, M. S. Wei, N. C. Woolsey, and P. A. Norreys. Space and time resolved measurements of the heating of solids to ten million kelvin by a petawatt laser. *New Journal of Physics*, 10, 2008. ISSN 13672630. doi: 10.1088/1367-2630/10/4/043046.

[151] P. Antici, L. Gremillet, T. Grismayer, P. Mora, P. Audebert, M. Borghesi, C. A. Cecchetti, A. Mančic, and J. Fuchs. Modeling target bulk heating resulting from ultra-intense short pulse laser irradiation of solid density targets. *Physics of Plasmas*, 20(12), 2013. ISSN 1070664X. doi: 10.1063/1.4833618.

[152] M Makita, G Nersisyan, K McKeever, T Dzelzainis, S White, B Kettle, B Dromey, D Doria, M Zepf, C L S Lewis, A P L Robinson, S B Hansen, and D Riley. Fast electron propagation in Ti foils irradiated with sub-picosecond laser pulses at I lambda2 >10 18 Wcm-2 mu m2. *Physics of Plasmas*, 21(2), 2014. ISSN 1070664X. doi: 10.1063/1.4865825.